Maria Aline Gonçalves

Nonlinear Dynamics and Pitch Control of Spacecraft with Sloshing Effects and Reaction Wheel Imbalance

Bauru, SP

2025

Maria Aline Gonçalves

Nonlinear Dynamics and Pitch Control of Spacecraft with Sloshing Effects and Reaction Wheel Imbalance

Thesis presented to the Graduate Program in Electrical Engineering of the Faculty of Engineering at Bauru Campus (FEB-UNESP), in partial fulfillment of the requirements for the degree of Doctor of Philosophy in Electrical Engineering.

São Paulo State University "Júlio de Mesquita Filho"

Faculty of Engineering - Campus Bauru

Electrical Engineering Graduate Program

Supervisor: Prof. Tit. José Manoel Balthazar

Co-supervisor: Prof. Dra. Elżbieta Jarzębowska

Bauru, SP

2025

G635n

Gonçalves, Maria Alice
Nonlinear dynamics and pitch control of spacecraft with sloshing effects and reaction wheel imbalance / Maria Alice Gonçalves. -- Bauru, 2025
142 f. : il., tabs., fotos

Tese (doutorado) - Universidade Estadual Paulista (UNESP), Faculdade de Engenharia, Bauru
Orientador: José Manoel Balthazar
Coorientadora: Elbieta Jarzbowska

1. Satélites artificiais. 2. Dinâmica de fluidos. 3. Modelagem matemática. 4. Controle ótimo. 5. Sistemas de controle. I. Título.

Sistema de geração automática de fichas catalográficas da Unesp. Dados fornecidos pelo autor(a).

ATA DA DEFESA PÚBLICA DA TESE DE DOUTORADO DE MARIA ALINE GONÇALVES, DISCENTE DO PROGRAMA DE PÓS-GRADUAÇÃO EM ENGENHARIA ELÉTRICA, DA FACULDADE DE ENGENHARIA - CÂMPUS DE BAURU.

Aos 13 dias do mês de junho do ano de 2025, às 9h, por meio de Videoconferência, realizou-se a defesa de TESE DE DOUTORADO de MARIA ALINE GONÇALVES, intitulada **NONLINEAR DYNAMICS AND PITCH CONTROL OF SPACECRAFT WITH SLOSHING EFFECTS AND REACTION WHEEL IMBALANCE** . A Comissão Examinadora foi constituída pelos seguintes membros: Prof. Dr. JOSE MANOEL BALTHAZAR (Orientador(a) - Participação Virtual) do(a) Departamento de Engenharia Mecânica docente voluntário / Universidade Estadual Paulista Unesp Faculdade de Engenharia Câmpus Bauru, PROFESSOR ADJUNTO CARLOS ALBERTO BAVASTRI (Participação Virtual) do(a) Departamento Academico de Mecanica / UNIVERSIDADE TECNOLÓGICA FEDERAL DO PARANA, Prof. Dr. ANTONIO FERNANDO BERTACHINI DE ALMEIDA PRADO (Participação Virtual) do(a) INPE, Prof. Dr. ATILA MADUREIRA BUENO (Participação Virtual) do(a) Politécnico / Universidade de São Paulo (USP), Prof. Dr. CLIVALDO DE OLIVEIRA (Participação Virtual) do(a) Departamento de Engenharia Mecânica / Universidade Federal da Grande Dourados - UFGD. Após a exposição pela doutoranda e arguição pelos membros da Comissão Examinadora que participaram do ato, de forma presencial e/ou virtual, a discente recebeu o conceito final APROVADA .Nada mais havendo, foi lavrada a presente ata, que após lida e aprovada, foi assinada pelo(a) Presidente(a) da Comissão Examinadora.

Prof. Dr. JOSE MANOEL BALTHAZAR

gov.br Documento assinado digitalmente
JOSE MANOEL BALTHAZAR
Data: 14/06/2025 08:38:54-0300
Verifique em https://validar.iti.gov.br

Potential Impact of this Research

This work is part of the advancement of nonlinear dynamics and control studies applied to spacecraft systems containing internal fluid, contributing to the strengthening of the research line in Dynamical Systems at the Faculty of Engineering of Bauru – UNESP. At the regional level, the study reinforces the local research group's performance in satellite dynamics, sloshing effects, and nonlinear control, supporting the formation of highly qualified human resources in the field.

At the national level, the research aligns with the strategic objectives of the Brazilian Space Program, especially with projects developed by the National Institute for Space Research (INPE), a recognized leader in orbital missions involving small and medium-sized satellites. The CBERS series (China-Brazil Earth Resources Satellite), a result of a technological cooperation between Brazil and China, stands out as a major international insertion milestone in the national space program. Moreover, INPE leads initiatives focused on technological training through micro and nanosatellite programs such as Amazonia-1 and NANOSATC-BR, which present direct potential applications of the numerical and methodological approaches developed in this thesis.

On an international scale, this research contributes to the scientific literature concerning the dynamic behavior of spacecraft with partially filled fuel tanks, by incorporating a nonlinear modeling framework for sloshing effects and modern control strategies. Although this thesis is limited to controlling the pitch axis variable, the results can be extended to other configurations and applied to space systems operating under strict mass, power, and volume constraints, such as CubeSats and other nanosatellites. This approach provides a robust framework for the development of more efficient control strategies in systems with strong structure–fluid coupling.

Dedico esta conquista às mulheres que,
pelo trabalho invisível e compulsório do cuidado,
tiveram suas trajetórias interrompidas
e o direito à educação negado.
Entre elas, minha mãe.

I dedicate this achievement to the women who,
through invisible and compulsory care work,
had their trajectories interrupted
and their right to education denied.
Among them, my mother.

Acknowledgements

Completing this doctoral degree represents not only the fulfillment of an academic goal, but also the overcoming of numerous personal, professional, and family challenges. This journey was only possible thanks to the generous and unwavering support of many people, to whom I express my deepest and most sincere gratitude.

To Prof. Dr. José Manoel Balthazar, my advisor, for his trust, precise scientific guidance, and commitment to academic excellence. His rigor and intellectual generosity were fundamental to the consolidation of this work.

To Prof. Dr. Elżbieta Jarzębowska, my co-advisor, for her warm welcome in Warsaw, her teachings, attentive guidance, and valuable technical contributions. The period I spent in Poland was particularly rich, both academically and personally, and it will leave a lasting mark on my professional formation.

To the São Paulo State University (UNESP), to the Graduate Program in Electrical Engineering at Bauru, and to CAPES for the institutional and financial support that enabled the development of this research.

To Uninter, my home institution, for providing the conditions necessary for my growth as a profesor and researcher. Through Uninter, I found financial stability, academic freedom, and the opportunity to apply in our research projects and in my work with students everything I learned throughout the doctoral process. I am especially grateful to my colleagues for the respectful and collaborative environment, and in particular Prof. M.Sc. Juliano P. and Prof. M.Sc. Eliane S., my program coordinator and lab colleague, respectively, for their technical exchanges, advice, and generous support during difficult times. Your presence made a significant difference in this journey.

To my mother, for her absolute and unconditional dedication. During much of the doctoral period — especially when I was abroad — she assumed full responsibility for caring for Victor. Without her support, it would have been simply impossible to complete this thesis. This work is also hers.

To my son Heitor, who accompanied me through relocations across cities and countries, always with sensitivity, maturity, and companionship beyond his years. His constant and generous presence gave me strength in the most demanding moments. Thank you for walking this path with me, even through the hardest stretches.

To my colleagues and friends from the research group, for the technical discussions, mutual support, and enriching companionship over the years.

To all those who, directly or indirectly, contributed to this journey, my sincere thanks.

This thesis is the result of many hands, many affections, and many shared silences. To all of you, my eternal gratitude.

Aos sonhos adiados, às vozes silenciadas,
às que carregam o mundo nas costas
sem que a história lhes dê os créditos

Que esta página sirva de registro:
a ciência também é feita de mãos que acolhem,
de noites em claro vigiando febres,
de pratos lavados e lares sustentados
enquanto outros seguem estudando

Que um dia o cuidado seja escolha,
e o conhecimento, direito de todas

To the deferred dreams, to the silenced voices,
to those who carry the world on their backs
without history giving them credit

May this page serve as a record:
science is also made of hands that comfort,
of sleepless nights watching over fevers,
of washed dishes and homes sustained
while others continue studying

May care one day be a choice,
and knowledge, a right for all

Abstract

Esta tese trata da modelagem não linear e do controle da dinâmica de arfagem de satélites influenciada pelo efeito de sloshing de fluido interno. O modelo dinâmico proposto é desenvolvido com base na formulação lagrangiana, representando o movimento do fluido por meio de um pêndulo equivalente. A formulação preserva as não linearidades do sistema, incluindo os efeitos gravitacionais e elásticos, além de considerar distúrbios externos como o desbalanceamento da roda de reação, possibilitando uma descrição realista do acoplamento entre corpo rígido e fluido na direção de arfagem. As simulações numéricas revelam comportamentos dinâmicos não lineares complexos, incluindo oscilações periódicas e quase-periódicas. Esses comportamentos foram caracterizados por meio de expoentes de Lyapunov, seções de Poincaré e análise espectral. Apesar da presença de expoentes de Lyapunov positivos em certos regimes, não foram observadas trajetórias caóticas consolidadas. Com o objetivo de suprimir as oscilações induzidas pelo sloshing e estabilizar o movimento de arfagem, foi implementado um controlador baseado na Equação de Riccati Dependente do Estado (SDRE). Esse controlador aplica torque diretamente ao corpo rígido, influenciando indiretamente o fluido pelo acoplamento dinâmico. Também foi considerada uma versão com atraso de tempo constante no loop de controle. O controlador SDRE apresentou rápida estabilização e alta precisão de rastreamento, embora com elevado esforço de controle durante o regime transitório. Controladores alternativos, baseados em Controle por Modos Deslizantes (SMC) e em sua variante híbrida com ação PID (SMC-PID), também foram avaliados. Os resultados mostraram que o SMC clássico reduz o esforço de controle, mas sofre com chattering e convergência mais lenta. Por outro lado, o controlador SMC-PID demonstrou ser uma solução eficaz, mitigando o chattering e alcançando desempenho superior em termos de tempo de estabilização e suavidade do torque, com níveis moderados de atuação. Este trabalho contribui com estratégias de modelagem e controle para sistemas satelitais subatuados sujeitos à redistribuição de massa interna, fornecendo uma base teórica e numérica para o desenvolvimento de sistemas de controle de atitude robustos e energeticamente eficientes em missões autônomas futuras.

Palavras-chave: Dinâmica de satélites. Sloshing de fluido. Modelagem não linear. Equação de Riccati Dependente do Estado (SDRE). Controle não linear. Desbalanceamento da roda de reação.

Abstract

This thesis addresses the nonlinear modeling and control of spacecraft pitch dynamics affected by internal liquid sloshing. The proposed dynamic model is developed via Lagrangian mechanics, representing the fluid motion through an equivalent pendulum. The formulation preserves full nonlinearities, including gravitational and elastic potential energies, and accounts for external disturbances such as reaction wheel imbalance, enabling a realistic depiction of the coupled rigid–fluid dynamics along the pitch axis. Numerical simulations reveal rich nonlinear behavior, including periodic and quasi-periodic oscillations, which are characterized using Lyapunov exponents, Poincaré sections, and spectral analysis. Although indicators such as positive Lyapunov exponents are observed, the system remains within bounded non-chaotic regimes under all tested conditions. To suppress sloshing-induced oscillations and stabilize the pitch motion, a nonlinear State-Dependent Riccati Equation (SDRE) controller is implemented. It applies torque directly to the rigid body, influencing the fluid motion through dynamic coupling. A variant with time-delay compensation is also evaluated. The SDRE controller achieves fast stabilization and high tracking precision, albeit at the cost of elevated control effort, particularly during transients. Alternative controllers based on Sliding Mode Control (SMC) and its hybrid variant with PID enhancement (SMC-PID) are also investigated. Results show that while classical SMC reduces control effort, it suffers from chattering and slower convergence. In contrast, the SMC-PID controller offers an effective compromise, significantly mitigating chattering and achieving superior performance in terms of stabilization time and control smoothness, with moderate actuation levels. Overall, this work contributes to the advancement of modeling and control strategies for underactuated spacecraft subjected to internal fluid dynamics. The findings provide theoretical foundations and simulation-based insights to support the design of robust and energy-aware attitude control systems for future autonomous missions.

Keywords: Spacecraft dynamics. Liquid sloshing. Nonlinear modeling. State-Dependent Riccati Equation (SDRE). Nonlinear control. Reaction wheel imbalance.

List of Figures

Figure 1 – Experimental Setup Demonstrating Liquid Sloshing in a Cylindrical Tank 24
Figure 2 – Disturbances and control relevance in different orbital regimes. In Low Earth Orbit (LEO), drag, magnetic torque, and gravity gradient are dominant. 25
Figure 3 – Mechanical analogs for liquid sloshing: (a) Linear model with mass-spring dashpot or simple pendulum; (b) Weakly nonlinear regime; (c) Sloshing with impact. 30
Figure 4 – Amazonia-1: Brazil's first fully indigenous Earth observation satellite, launched in 2021 to monitor deforestation and agricultural activity in the Amazon region. 33
Figure 5 – CBERS-4: A collaborative mission between Brazil and China providing multi-spectral imaging for environmental monitoring and disaster response. 33
Figure 6 – Block diagram of a typical Attitude Control System (ACS), illustrating sensor inputs, controller logic, and actuation via reaction wheels. . . . 36
Figure 7 – Reaction wheels installed on a spacecraft platform. Small deviations in mass symmetry can produce disturbance torques that affect pointing stability. 37
Figure 8 – Schematic diagram of the satellite-fluid system with sloshing, represented by an internal pendulum. 43
Figure 9 – Schematic model of a reaction wheel with static imbalance. A small mass m_s is mounted on the rim of the flywheel, producing a centrifugal force F_s as the wheel rotates with angular velocity ω_s. 49
Figure 10 – Time series and frequency analysis of the satellite's pitch and roll angle and angular velocity. 59
Figure 11 – Phase space diagram: ψ vs $d\psi$. 60
Figure 12 – 3D phase space: ψ, $d\psi$, and θ. 61
Figure 13 – Time series and frequency analysis of the sloshing mass angle and angular velocity. 63
Figure 14 – Phase space diagram: θ vs $d\theta$. 64

Figure 15 – 3D phase space: θ, $d\theta$, and ψ. 64
Figure 16 – Time evolution of the Lyapunov exponents for the variables ψ, $\dot{\psi}$, θ, and $\dot{\theta}$. 65
Figure 17 – Zoomed-in Poincaré map: section in θ for the variable ψ. Blue points correspond to $\dot{\psi} > 0$ and grey points to $\dot{\psi} < 0$. 68
Figure 18 – Full Poincaré map: section in θ for the variable ψ. Blue points correspond to $\dot{\psi} > 0$ and grey points to $\dot{\psi} < 0$. 68
Figure 19 – Zoomed-in Poincaré map: section in ψ for the variable θ. 70
Figure 20 – Full Poincaré map: section in ψ for the variable θ. 70
Figure 21 – Kinetic energy maps obtained from the parametric variation of parameters a and b. 72
Figure 22 – Potential energy maps obtained from the parametric variation of parameters a and b. 73
Figure 23 – Reaction wheel energy maps obtained from the parametric variation of parameters a and b. 74
Figure 24 – Satellite and fluid combined energy maps obtained from the parametric variation of parameters a and b. 75
Figure 25 – Total energy maps obtained from the parametric variation of parameters a and b. 75
Figure 26 – Time evolution of the Lyapunov exponents for the scenario with $a = 0.35\,\mathrm{m}$ and $b = -0.30\,\mathrm{m}$. 76
Figure 27 – Poincaré map in the θ vs $d\theta$ plane for the scenario with $a = 0.35\,\mathrm{m}$ and $b = -0.30\,\mathrm{m}$. Magenta points represent $\dot{\psi} > 0$, and dark gray points represent $\dot{\psi} < 0$. 77
Figure 28 – Full Poincaré map in the θ vs $d\theta$ plane for the scenario with $a = 0.35\,\mathrm{m}$ and $b = -0.30\,\mathrm{m}$. Blue points indicate $\dot{\psi} > 0$, and dark gray points indicate $\dot{\psi} < 0$. The behavior of θ remains regular, with organized patterns similar to those seen in the previous simulation. 78
Figure 29 – Poincaré map in the ψ vs $d\psi$ plane for the scenario with $a = 0.35\,\mathrm{m}$ and $b = -0.30\,\mathrm{m}$. Blue points represent $\dot{\psi} > 0$ and grey points represent $\dot{\psi} < 0$. 79
Figure 30 – Full Poincaré map in the ψ vs $d\psi$ plane for the scenario with $a = 0.35\,\mathrm{m}$ and $b = -0.30\,\mathrm{m}$. Blue points indicate $\dot{\psi} > 0$ and gray points indicate $\dot{\psi} < 0$. 79

Figure 31 – Time evolution of the pitch angle $\psi(t)$ with and without control.Greylines indicate the uncontrolled case and blue-colored segments correspond to the SDRE-controlled case. 87
Figure 32 – Time evolution of the sloshing mass angle $\theta(t)$ with and without control. 87
Figure 33 – Phase portrait of satellite pitch $(\psi,\ \dot{\psi})$ trajectories with and without control. Greylines indicate the uncontrolled case and blue-colored segments correspond to the SDRE-controlled case. 89
Figure 34 – Phase portrait of sloshing mass $(\theta,\ \dot{\theta})$ with and without control. Light ping indicate the uncontrolled case and dark pink-colored segments correspond to the SDRE-controlled case. 89
Figure 35 – Zoomed-in phase portrait of of satellite pitch $(\psi,\ \dot{\psi})$ with control after transient removal (20% of initial data excluded). 90
Figure 36 – Zoomed-in phase portrait of of sloshing mass $(\theta,\ \dot{\theta})$ with control after transient removal (20% of initial data excluded). 90
Figure 37 – Time evolution of the control torque $u(t)$ generated by the SDRE controller. 91
Figure 38 – Time evolution of the pitch angle $\psi(t)$: free system (gray), SDRE control (light blue), and under SDRE control with delay ($\tau = 0.1$ s), after 10% transient removal (dark blue). 93
Figure 39 – Time evolution of the sloshing angle $\theta(t)$: free system (light pink), SDRE control (red), and under SDRE control with delay ($\tau = 0.1$ s), after 10% transient removal (magenta). 93
Figure 40 – Phase portraits of satellite pitch $(\psi,\ \dot{\psi})$: free system (gray), SDRE control (light blue), and under SDRE control with delay ($\tau = 0.1$ s), after 10% transient removal (dark blue). 94
Figure 41 – Phase portraits of sloshing mass $(\theta,\ \dot{\theta})$: free system (light pink), SDRE control (dark pink), and under SDRE control with delay ($\tau = 0.1$ s), after 10% transient removal (magenta). 95
Figure 42 – Comparison of control torque $u(t)$: SDRE controller with and without time delay ($\tau = 0.05$ s). 96
Figure 43 – Comparison of control torque $u(t)$: SDRE controller with and without time delay ($\tau = 0.05$ s). 97
Figure 44 – Time evolution of the pitch angle $\psi(t)$ for all control scenarios. Gray: Free dynamics; Cyan: SDRE; Blue: SDRE with delay; Red: Sliding Mode. . . 100

Figure 45 – Time evolution of the sloshing angle $\theta(t)$ for all control scenarios. Pink: Free dynamics; Hotpink: SDRE; Magenta: SDRE with delay; Black: Sliding Mode. 101
Figure 46 – Control effort $u(t)$ for each strategy. Orange: SDRE; Blue: SDRE with delay; Purple: Sliding Mode. 101
Figure 47 – SMC-PID control effort over 600 seconds of simulation. 103
Figure 48 – SMC-PID control effort during the transient period (0–100 s). . . . 103
Figure 49 – Comparison of control torque during transients for all controllers. 104
Figure 50 – Time evolution of state variables under SMC-PID control. 104
Figure 51 – Stages of the bibliometric selection process. 117
Figure 52 – Distribution of result papers by keyword 118
Figure 53 – Distribution of result papers by publication year 119

List of Tables

Table 1 – Description of variables used in the satellite–fluid dynamic model . 43
Table 2 – Main parameters of the satellite-fluid system. 56
Table 3 – Initial conditions adopted in the simulations. 57
Table 4 – Comparison of performance indicators with and without SDRE control. . 88
Table 5 – Quantitative performance comparison of all evaluated controllers. . 105
Table 6 – Keyword groups and codes used in the bibliometric analysis 118
Table 7 – Most productive and impactful journals in the selected dataset . . 120
Table 8 – Top 10 selected papers relevant to spacecraft dynamics and fuel sloshing control 121

List of abbreviations and acronyms

ACS	Attitude Control System
ADCS	Attitude Determination and Control System
CFD	Computational Fluid Dynamics
FLEVO	Facility for Liquid Experimentation and Verification On-orbit
FFT	Fast Fourier Transform
HIL	Hardware-in-the-Loop
LQR	Linear Quadratic Regulator
LEO	Low Earth Orbit
MIMO	Multiple-Input Multiple-Output
NASA	National Aeronautics and Space Administration
ODE	Ordinary Differential Equation
PDE	Partial Differential Equation
PID	Proportional–Integral–Derivative
SDRE	State-Dependent Riccati Equation
SISO	Single-Input Single-Output
SMC	Sliding Mode Control
SPH	Smoothed Particle Hydrodynamics
TVC	Thrust Vector Control

List of symbols

$\psi(t)$	Satellite pitch angle (rotation around the principal axis)
$\theta(t)$	Relative angle of the pendulum representing the sloshing
$\dot{\psi}(t)$	Satellite angular velocity
$\dot{\theta}(t)$	Pendulum angular velocity
m_f	Fluid fixed mass
m_p	Pendulum mass (sloshing equivalent mass)
I_{sat}	Satellite moment of inertia about the pitch axis
I_f	Pendulum moment of inertia about the pivot
a	Length of the pendulum rod
b	Distance from the pivot to the satellite center of mass
c	Distance from the satellite center of mass to the torque application point
g	Gravitational acceleration at 450 km altitude
M_ψ	Control torque applied to the satellite
$T_s(t)$	External disturbance torque (reaction wheel imbalance)
ε	Fluid damping coefficient
$K_r(\psi, \theta)$	Restorative stiffness matrix of the coupled system
$Q(x)$	State weighting matrix (SDRE control)
$R(x)$	Control weighting matrix (SDRE control)
$K(x)$	State-dependent feedback gain matrix (SDRE)

$s(t)$	Sliding surface (SMC)
k	Switching gain of the SMC
λ	Convergence rate parameter of the sliding surface
$u(t)$	Control signal (applied torque)

Contents

	Impacto da Pesquisa	**4**
1	**INTRODUCTION**	**23**
1.1	**Problem Statement**	**24**
1.2	**Research Motivation**	**25**
1.3	**Objectives**	**26**
1.4	**Thesis Structure**	**27**
2	**LITERATURE REVIEW**	**28**
2.1	**Classical Studies on Sloshing and Satellite Dynamics**	**29**
2.1.1	Sloshing Dynamics	29
2.1.2	Spacecraft Applications	31
2.2	**State-of-the-Art and Recent Advances**	**34**
2.2.1	Modeling of Satellite Dynamics with Sloshing	34
2.2.2	Disturbance Torques and Reaction Wheel Imbalance	35
2.2.3	Control Strategies in Sloshing-Affected Systems	38
2.3	**Summary and Research Gaps**	**40**
3	**MATHEMATICAL MODELING**	**42**
3.1	**Hypotheses and Model Restrictions**	**42**
3.2	**Lagrangian Formulation**	**44**
3.2.1	Relative Positions and Velocities	45
3.2.1.1	Fixed Mass Position	45
3.2.1.2	Absolute Velocities	46
3.2.2	Total Kinetic Energy of the System	46
3.2.2.1	Kinetic Energy of the Pendulum Mass	46
3.2.2.2	Kinetic Energy of the Fixed Mass	47
3.2.2.3	Rotational Kinetic Energy of the Satellite	47
3.2.2.4	Total Kinetic Energy	47
3.2.3	Potential Energy	47

3.2.3.0.1 Note on Gravitational Acceleration. 48
3.2.4 Equation of Motion for ψ 49
3.2.5 Equation of Motion for $\theta(t)$ 51
3.2.6 Disturbance Torque from Unbalanced Reaction Wheels 52
3.2.7 Matrix Form 52

4 NUMERICAL SIMULATION AND RESULTS ANALYSIS 54
4.1 Methods, Techniques, and Parameters Employed 54
4.2 Simulation Methods and Parameters 55
4.3 Time and Spectral Analysis via FFT 57
4.3.1 Analysis of the Pitch Angle ψ 58
4.3.2 Analysis of the Angular Velocity $\dot{\psi}$ 60
4.3.3 Analysis of the Fluid Oscillation Angle θ 62
4.3.4 Analysis of the Fluid Angular Velocity $\dot{\theta}$ 62
4.4 Lyapunov Exponent Analysis 65
4.5 Poincaré Map Analysis 66
4.5.1 Poincaré Maps for the Variable ψ 67
4.5.2 Poincaré Maps for the Variable θ 69
4.6 Parametric Analysis of the System Energy as a Function of Parameters a and b 71
4.6.1 Kinetic Energy 71
4.6.2 Potential Energy 71
4.6.3 Energy Associated with the Reaction Wheel Imbalance Torque . . 72
4.6.4 Combined Energy of the Satellite and the Fluid 73
4.6.5 Total Energy of the System 74
4.7 Extreme Scenario Analysis: $a = 0.35\,\mathrm{m}$, $b = -0.30\,\mathrm{m}$ 76

5 NONLINEAR CONTROL 80
5.0.1 Notation Clarification 80
5.1 Control Design Using SDRE Methodology 81
5.1.1 State-Dependent Representation 82
5.1.2 SDRE-Based Optimal Control Design 83
5.1.3 Numerical Evaluation in the Extreme Scenario 84

5.1.3.0.1 Remark: Augmenting the System with Integral Action. 92
5.1.4 SDRE Control with Time Delay Compensation 92
5.1.5 Comparison of Control Effort with and without Time Delay 95
5.1.6 Comparison of Control Effort and Energy Consumption with and without Time Delay 96
5.1.7 Sliding Mode Control Design 98
5.1.8 Comparison of Control Strategies 99
5.1.9 Sliding Mode Control with PID Enhancement (SMC-PID) 102

6 CONCLUSION 106
6.1 Future Work 107

BIBLIOGRAPHY 110

APPENDIX 116

APPENDIX A – BIBLIOMETRIC ANALYSIS OF THE LITERATURE 117
A.0.1 Search Strategy and Keywords 118
A.0.2 Data Cleaning and Preprocessing 119
A.0.3 Selection Criteria 120

APPENDIX B – MATHEMATICAL MODELING CODE 122

APPENDIX C – SIMULATION CODE FOR THE SATELLITE-FLUID MODEL 129

APPENDIX D – ANALYTICAL EXPRESSIONS FOR THE MATRICES A(X), B(X), AND THE VECTOR G(X,T) 138

1 Introduction

This chapter presents a comprehensive review of the literature concerning the modeling, analysis, and control of spacecraft attitude dynamics, a term that encompasses the vehicle's orientation in space, typically described by three rotational degrees of freedom: pitch, yaw, and roll. While most of the referenced works address the general framework of attitude control, the present study concentrates specifically on pitch dynamics, which refers to the rotation about the lateral axis and is particularly sensitive to the influence of internal fluid motion and actuator-induced disturbances (**??**). The increasing use of satellites in Low Earth Orbit (LEO)—especially those incorporating liquid propellant systems and subject to stringent pointing accuracy requirements—has heightened the demand for accurate nonlinear dynamic models (**????**). These models must capture internal mass redistribution effects—primarily attributable to liquid sloshing—as well as unbalanced torques generated by actuators such as reaction wheels. To contextualize the present research, a bibliometric analysis was conducted, followed by a qualitative synthesis of seminal and contemporary works addressing the coupled dynamics of fluid motion and spacecraft orientation. A summary of this analysis is presented in Appendix **??**.

This research represents the first study conducted by the group coordinated by Prof. José Manoel Balthazar at UNESP–Bauru specifically focused on spacecraft dynamics with internal fluid interaction. Although Prof. Balthazar has led other projects on this topic at different institutions, this marks the inaugural effort within the Bauru-based team. It thus establishes a foundational contribution for future investigations within the group and supports the development of advanced pitch-axis control strategies applicable to small satellites and agile platforms.

This chapter introduces the sloshing phenomenon, its engineering relevance, the problem context motivating this research, and the objectives pursued. It concludes by outlining the thesis structure and the contribution of each chapter.

1.1 Problem Statement

The transport of liquids within mobile systems, such as spacecraft or tank trucks, introduces nonlinear dynamic interactions. Even minor accelerations can induce fluid oscillations that compromise the stability of the entire structure (**??**), as visually exemplified in Figure **??**. In aerospace systems, the situation becomes critical, as the sloshing of propellant within partially filled tanks alters the mass distribution and induces torques that may degrade the performance of the attitude control system (ACS)—particularly along axes subject to stringent pointing accuracy requirements (**????**).

Sloshing refers to the nonlinear, often chaotic, motion of a liquid's free surface when the containing structure experiences acceleration. These oscillations involve energy exchange between the fluid and the container, frequently manifesting as instabilities or long-term drift in vehicle's orientation. Traditional linear models predict sloshing behavior under small perturbations, estimating natural frequencies and hydrodynamic pressures. However, they fail to capture relevant nonlinear phenomena such as rotary motion of the free surface, coupled fluid-structure dynamics, and transitions to chaotic regimes, which are critical in missions involving significant attitude maneuvers or structural flexibility (**??**). Figure **??** shows an experimental setup capturing such dynamics.

Figure 1 – Experimental Setup Demonstrating Liquid Sloshing in a Cylindrical Tank

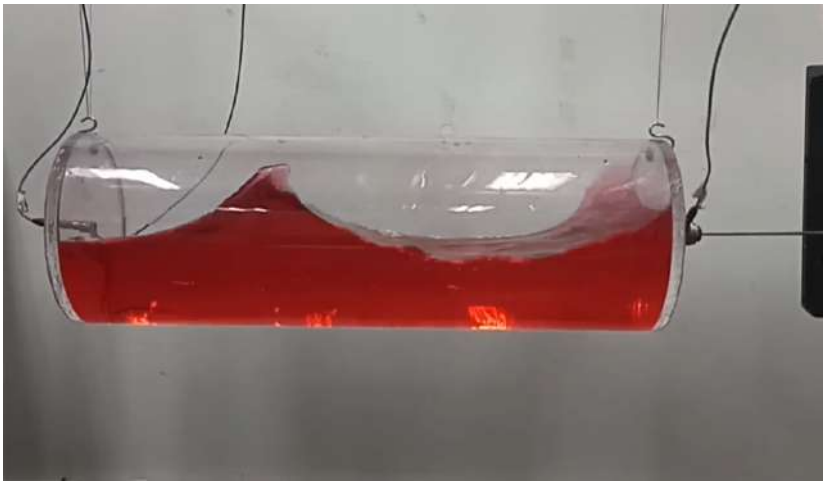

Source: Laboratory of Vibrations and Acoustics, UFPR. Image used with permission.

1.2 Research Motivation

The motivation for this work stems from the increasing demand for high-performance attitude control in Low Earth Orbit (LEO) missions, where maintaining accurate orientation is essential for mission success. A major challenge in this domain lies in the presence of internal disturbances, such as reaction wheel imbalance and liquid propellant sloshing, which introduce nonlinearities that are difficult to model and control effectively. As illustrated in Figure **??**, LEO missions are characterized by a complex disturbance environment, including drag, magnetic torque, and gravity gradient effects. These external perturbations compound the internal dynamics, demanding robust and precise control strategies.

Figure 2 – Disturbances and control relevance in different orbital regimes. In Low Earth Orbit (LEO), drag, magnetic torque, and gravity gradient are dominant.

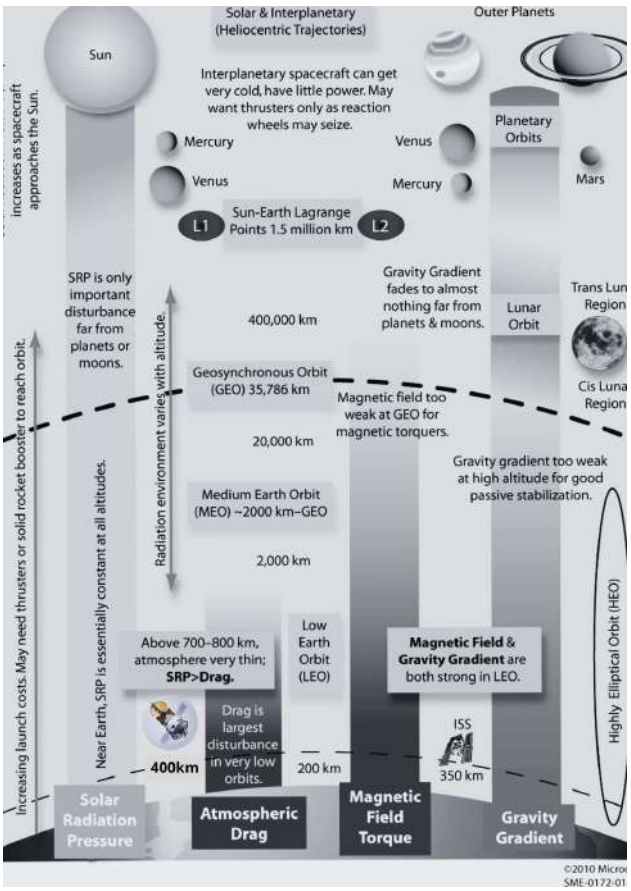

Source: Adapted from (**??**).

Although attitude control encompasses all rotational degrees of freedom, this research focuses specifically on the pitch axis, which is often the most sensitive to slosh-induced torques due to its alignment with major structural and propellant tank axes. By addressing pitch dynamics under fluid-structure coupling, the study contributes a targeted solution to a broader control problem—enhancing the overall robustness and reliability of spacecraft orientation systems under internal disturbances (**????**).

However, despite the importance of capturing fluid-structure coupling effects, many existing studies simplify the system by decoupling the fluid motion from the rigid dynamics, or by relying on computationally intensive CFD simulations that limit practical applicability. To overcome these limitations, this thesis proposes a reduced-order model, formulated via Lagrangian mechanics, that retains the key nonlinear interactions between satellite and fluid dynamics in the pitch axis, enabling tractable simulation and control design.

1.3 Objectives

This thesis aims to model and control the pitch-axis dynamics of a satellite affected by internal propellant sloshing and reaction wheel imbalance. The specific objectives are:

- Develop a nonlinear reduced-order model, based on Lagrangian formulation, to represent the coupling between satellite pitch dynamics and fluid sloshing through an equivalent pendulum representation;
- Analyze the nonlinear behavior of the coupled system using dynamical systems theory tools–such as Poincaré maps and Lyapunov exponents–to identify periodic, quasi-periodic, and chaotic regimes;
- Design and evaluate nonlinear control strategies, particularly State-Dependent Riccati Equation (SDRE) and Sliding Mode Control (SMC), emphasizing robustness against time delays and actuator imperfections;

- Validate the proposed model and control strategies through numerical simulations under both nominal and perturbed dynamic conditions, including parameter variations;
- Provide design-oriented recommendations for parameter tuning and mass placement in propellant tanks to mitigate the adverse effects of fluid sloshing on satellite pitch-axis control.

1.4 Thesis Structure

The thesis is structured as follows:

Chapter 2: A comprehensive literature review on sloshing dynamics, spacecraft modeling, actuator imbalances, and nonlinear control strategies, including a bibliometric analysis guiding this work.

Chapter 3: Development of the mathematical model derived using Lagrangian mechanics, capturing the nonlinear coupling between the satellite and the sloshing fluid in the pitch axis.

Chapter 4: Analysis of the uncontrolled pitch dynamics using simulations and nonlinear diagnostic tools (time series, FFT, Lyapunov exponents, Poincaré maps), including parametric studies and identification of extreme scenarios.

Chapter 5: Development and evaluation of SDRE and SMC control strategies under nominal and extreme conditions, including time delay considerations and comparisons of control effort.

Chapter 6: Conclusions and future work, summarizing the key findings, practical implications, and directions for experimental validation and methodological improvements.

2 Literature Review

This chapter provides a comprehensive review of the literature pertinent to the modeling, analysis, and control of satellite dynamics under the influence of internal fluid motion and disturbances induced by actuators. The increasing deployment of satellites in Low Earth Orbit (LEO), particularly those incorporating liquid propellant systems and stringent pointing accuracy requirements, has heightened the demand for accurate nonlinear dynamic models (**????**). These models must capture internal mass redistribution effects—primarily attributable to liquid sloshing—as well as unbalanced torques generated by reaction wheels (**????**). To substantiate and contextualize the present study, a bibliometric analysis was carried out, followed by a qualitative synthesis of seminal and contemporary works in the field.

Missions in Low Earth Orbit (LEO) encompass satellites and space platforms operating at altitudes generally below 2,000 kilometers. Due to their proximity to Earth and reduced signal transmission latency, LEO missions are extensively employed in applications such as Earth observation, telecommunications, navigation, and microgravity experimentation (**????**). As these missions impose increasingly stringent pointing accuracy requirements and commonly integrate onboard liquid systems, the formulation of models that accurately represent internally coupled disturbances—particularly liquid sloshing and reaction wheel imbalance—has become essential for achieving robust attitude control performance, especially along critical axes such as pitch (**????**).

The dynamics and control of liquid sloshing in partially filled tanks hold critical implications across multiple engineering domains, notably aerospace, automotive, and chemical engineering. Within the aerospace domain, sloshing phenomena can significantly degrade attitude stability, control accuracy, and overall mission reliability (**????**). This chapter offers a systematic and contemporary review of the literature on liquid sloshing, synthesizing classical theoretical frameworks with recent methodological and computational advancements. The reference selection process was informed by a bibliometric study performed through the CAPES Periodicals Portal, thereby

ensuring a thorough and up-to-date characterization of the state-of-the-art.

2.1 Classical Studies on Sloshing and Satellite Dynamics

The study of liquid sloshing in partially filled containers has long been recognized as a critical factor influencing the dynamic behavior of aerospace systems, particularly spacecraft equipped with onboard liquid propellants. Accurate modeling of such phenomena is essential for predicting and mitigating disturbances that can significantly compromise attitude stability and control performance. Over the decades, several foundational studies have advanced the understanding of sloshing dynamics through both theoretical analysis and experimental validation.

This section reviews classical contributions that laid the groundwork for modeling sloshing effects and their implications for spacecraft dynamics. These methodologies have played a pivotal role in enabling analytical tractability while capturing the dominant dynamic characteristics of internal fluid motion and its coupling with rigid and flexible structural components.

2.1.1 Sloshing Dynamics

The hydrodynamic pressure exerted by liquid within rigid containers can be decomposed into two primary components: an inertial contribution associated with the bulk fluid motion—directly proportional to the container's acceleration—and a convective component arising from fluid movement at the free surface. These dynamic effects are commonly modeled using equivalent mechanical analogs comprising lumped masses, springs, and dampers, which replicate the forces and torques induced by internal fluid motion (**??**).

Linear modeling approaches often rely on mass-spring-damper configurations or simplified pendulum structures to describe planar sloshing behavior under the assumption of small angular displacements. These approximations yield accurate results when the fluid oscillates near equilibrium, with low-amplitude motion about the vertical axis. Under such conditions, the restoring torque is approximately linearly proportional to the angular deviation, allowing for the application of linear system

theory (Fig. **??**a).

However, as the sloshing amplitude increases, nonlinear phenomena emerge. The relationship between the restoring torque and angular displacement deviates from linearity, giving rise to weakly nonlinear behavior (Fig.**??**b). At higher amplitudes, the system may enter strongly nonlinear regimes characterized by wave breaking, fluid-structure impacts against tank walls, and potentially chaotic fluid motion (Fig. **??**c).

Figure 3 – Mechanical analogs for liquid sloshing: (a) Linear model with mass-spring dashpot or simple pendulum; (b) Weakly nonlinear regime; (c) Sloshing with impact.

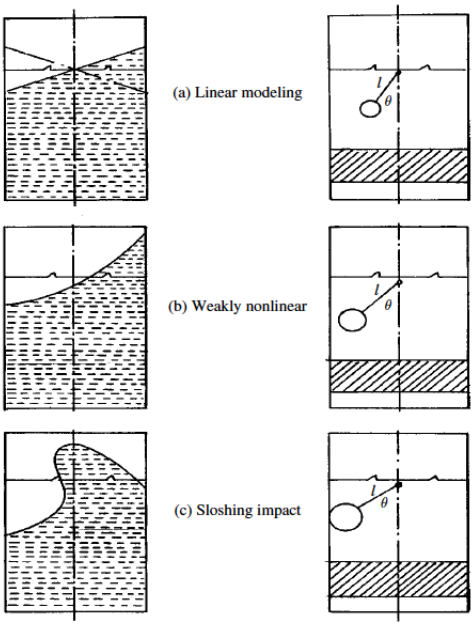

Source: Adapted from **??**).

For the purposes of this research, a single pendulum model with large angular displacement is employed to capture the dominant sloshing mode. This approach preserves analytical tractability while incorporating essential nonlinear characteristics necessary for accurate dynamic representation.

The angular deviation between the pendulum and its vertical equilibrium position serves as a critical indicator for the applicability of linear assumptions. Empirical evidence and theoretical analysis confirm that linear approximations remain

valid for deviations below approximately 5°. Beyond this threshold, nonlinear contributions dominate the system response, significantly affecting dynamic behavior. This transition from linear to nonlinear dynamics has been extensively documented in foundational works, notably by Abramson (**??**), who formulated reduced-order pendulum-based models for sloshing analysis. His studies emphasized the limitations of such representations under conditions involving large angular amplitudes and rotational sloshing, highlighting the necessity for more sophisticated modeling frameworks in such cases.

2.1.2 Spacecraft Applications

As previously discussed, the phenomenon of liquid sloshing has long presented substantial challenges in spacecraft design and attitude control—particularly in axes such as pitch. Early investigations trace back to the 1950s, when **??**), inspired by analogous problems in aircraft dynamics, postulated that the movement of free liquid surfaces within onboard tanks could exert non-negligible influence on spacecraft behavior, especially under resonant excitation conditions. Building upon this foundation, **??**) extended the analytical framework by applying linearized fluid models and equivalent mechanical analogs to characterize sloshing across various tank configurations. These theoretical formulations were substantiated through experimental validation, marking a key milestone in the development of predictive tools for spacecraft applications.

Several landmark space missions, including ATS-V (1969) and Intelsat IV, underscored the critical sensitivity of satellite stability to sloshing-induced disturbances, even in scenarios involving minimal residual propellant masses (**????**). During orbital maneuvers or re-entry phases, internal fluid oscillations can result in wall impacts, generating unexpected perturbation torques that compromise attitude control performance (**??**). In the early 2000s, **??**) applied computational fluid dynamics (CFD) within the Sloshsat mission to simulate these nonlinear interactions. However, the high computational demand and limited real-time applicability of full-scale CFD models prompted further research into alternative methodologies.

To address these limitations, **??**) proposed a coupled formulation integrating Navier–Stokes equations with rigid-body spacecraft dynamics, thereby enabling

a more physically consistent representation of fluid–structure interaction. This approach represented a significant step toward balancing model fidelity and numerical tractability.

From a control systems perspective, **??**) introduced a control-oriented modeling strategy based on a single-degree-of-freedom pendulum representation, specifically tailored for thrust vector control (TVC) synthesis. They also examined spherical-pendulum analogies to account for multi-directional sloshing modes. Complementing this effort, **??**) developed Lyapunov-based control laws grounded on simplified reduced-order models, circumventing the need for computationally intensive CFD simulations while preserving essential dynamic characteristics.

Contemporary research continues to investigate hybrid modeling and control strategies that reconcile simulation accuracy with computational efficiency. These include reduced-order modeling, finite element methods, and data-driven estimation techniques, as reported in recent studies by **??**), **??**), **??**), and **??**).

Within the Brazilian academic community, Souza (**??**) conducted research on robust control methodologies for spacecraft incorporating both rigid and flexible structural components alongside internal liquid motion. His doctoral work introduced H_∞ and H_∞-LMI control architectures designed to accommodate parametric uncertainties in the mass, damping, and stiffness matrices. The analysis revealed that variations in the mass matrix—often induced by sloshing—exhibit a particularly pronounced effect on the actuator effort required for attitude regulation. The proposed robust control solutions effectively stabilized the system under significant parameter uncertainty and nonlinear sloshing effects, offering valuable contributions to the advancement of high-precision spacecraft control design.

These research efforts align with Brazil's broader investments in space technology, exemplified by missions such as Amazonia-1 and CBERS-4, which require precise attitude control to fulfill Earth observation objectives. Figures **??** and **??** illustrate two flagship Brazilian satellites developed with the support of the National Institute for Space Research (INPE).

Figure 4 – Amazonia-1: Brazil's first fully indigenous Earth observation satellite, launched in 2021 to monitor deforestation and agricultural activity in the Amazon region.

Source: Amazonia-1/INPE – Divulgação.

Figure 5 – CBERS-4: A collaborative mission between Brazil and China providing multispectral imaging for environmental monitoring and disaster response.

Source: CBERS/INPE – Divulgação.

The literature review highlights the historical development, modeling strategies, and modern control techniques for sloshing in spacecraft. Despite significant advancements, challenges remain in balancing model fidelity with computational feasibility. This thesis aims to address these gaps by proposing a nonlinear model that incorporates sloshing and external disturbances, enabling analysis through nonlinear dynamics tools and supporting the future development of robust control laws.

2.2 State-of-the-Art and Recent Advances

The literature review presented so far has highlighted the foundational theories and classical methodologies used to model and control spacecraft dynamics under the influence of internal fluid motion. However, to ensure that the proposed modeling and control strategies align with current scientific advancements, it is essential to examine recent contributions grounded in up-to-date research trends and high-impact publications.

To contextualize the present study, a qualitative synthesis of seminal and contemporary works in the field is provided. This synthesis offers a data-driven basis for identifying key references that reflect the current state of the art in spacecraft dynamics, fuel sloshing modeling, and robust control design. The selected studies were filtered based on publication year, citation count, journal impact factor, and thematic relevance to nonlinear dynamics and control.

The following subsections present a synthesis of these recent advances, beginning with updated modeling approaches that capture the interaction between satellite rigid/flexible structures and internal sloshing dynamics. These models represent the evolution from simplified mechanical analogs to more comprehensive formulations that incorporate nonlinear couplings, structural flexibility, and fluid–structure interactions.

This section thus serves as a bridge between historical developments and contemporary research, providing a solid foundation for the modeling and control strategies proposed in this thesis.

2.2.1 Modeling of Satellite Dynamics with Sloshing

Modeling the interaction between internal fluid motion and satellite dynamics is one of the central challenges in analyzing space systems with partially filled tanks. Such models aim to represent the mass redistribution effects caused by sloshing, which directly affect the center of mass and moments of inertia, thereby impacting attitude control performance.

??) developed a dynamic model of a flexible satellite with sloshing based on

the Lagrangian formulation, considering both structural deformations and fluid–structure interactions. Their parametric stability analysis demonstrates how structural stiffness and fluid location influence the overall system behavior. This integration of flexibility and fluid motion is significant, as it addresses couplings often neglected in reduced-order models (**??**).

In a related effort, **??**) proposed a nonlinear model capturing the coupling between large-amplitude sloshing and satellite attitude dynamics. Also derived from Lagrange's equations, their work emphasizes the importance of accurately representing nonlinear fluid effects, particularly when linear approximations fail. The model proved effective for simulating highly dynamic orbital maneuvers and environments.

??) advanced the field further by modeling the satellite and fuel as a single, strongly coupled system. Using an equivalent pendulum to represent the fluid, they introduced fuzzy sliding mode control techniques directly into the model, facilitating its use in robust control applications. This integrated approach reinforces the fluid's role as an active component in the overall dynamics (**??**).

Together, these contributions reflect a growing trend in the literature: while equivalent pendulum models remain common due to their simplicity and analytical clarity, there is an increasing effort to build more comprehensive models that capture structural deformations, fluid–structure interaction, and nonlinear couplings. These advances enhance the realism of simulations and support the development of robust and reliable control strategies for real-world missions.

2.2.2 Disturbance Torques and Reaction Wheel Imbalance

Figure **??** illustrates the architecture of a typical Attitude Control System (ACS), which integrates sensor feedback, control algorithms, and actuators such as reaction wheels. In addition to the internal disturbances caused by fuel motion, spacecraft attitude control systems are subjected to a variety of internal and external torques. Among the most critical internal sources are imbalances in reaction wheels, which are essential actuators for fine attitude control—particularly in small satellites and nanosatellites.

Figure 6 – Block diagram of a typical Attitude Control System (ACS), illustrating sensor inputs, controller logic, and actuation via reaction wheels.

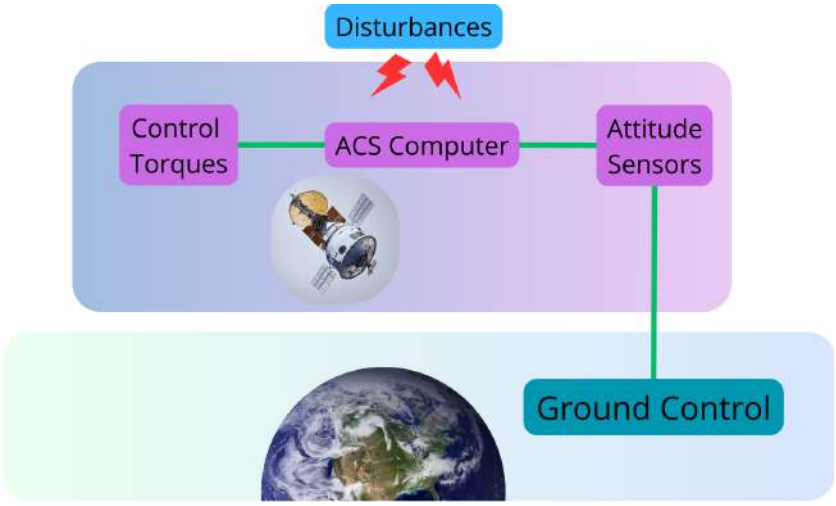

Source: The Author, 2025.

??) present a methodology for experimental identification of space manipulator systems that include the influence of fuel sloshing. Their approach, based on frequency response and modal analysis, enables the separation of dynamic contributions from different subsystems, such as parasitic torques generated by internal liquid motion and those arising from actuator imbalances. This decoupling is fundamental for the design of adaptive controllers and robust state observers in spacecraft systems.

As shown in Figure **??**, reaction wheels are electromechanical devices mounted on orthogonal axes within the spacecraft. Although they enable fine control of orientation, any slight imbalance in their mass distribution generates periodic torques that propagate to the spacecraft structure.

Figure 7 – Reaction wheels installed on a spacecraft platform. Small deviations in mass symmetry can produce disturbance torques that affect pointing stability.

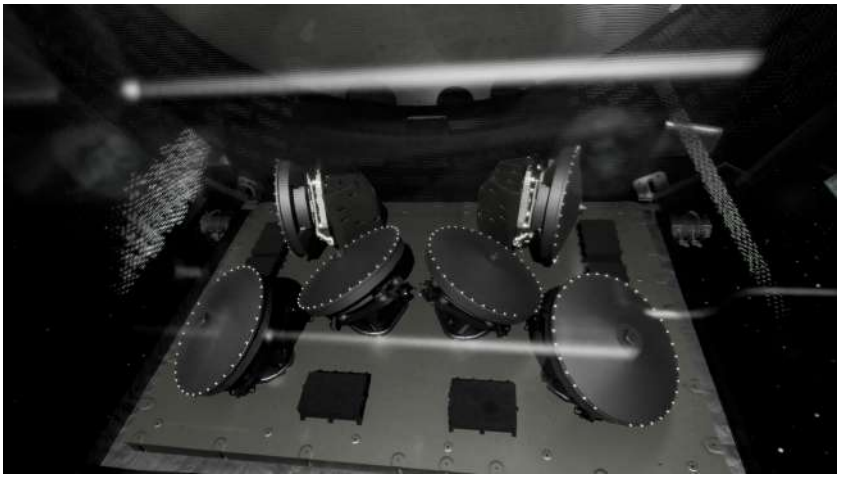

Source: NASA's Goddard Space Flight Center. Image credit: NASA.

??) examine the specific effects of reaction wheel imbalance on satellite attitude control performance. Their study demonstrates that even minor asymmetries in mass distribution—often inevitable due to manufacturing tolerances—can produce persistent oscillatory disturbances. These disturbances reduce control precision and can lead to instabilities, especially when compounded by sloshing-induced torques. The authors propose a simplified analytical model to represent imbalance-generated torques, allowing for their direct inclusion in the equations of motion.

Further investigations by Bayard **??**), **??**), and **??**), contribute to the development of modeling techniques and compensation strategies for these disturbances. Their works explore adaptive identification schemes and robust control laws designed to mitigate the impact of actuator degradation and evolving imbalance profiles over long-duration missions.

Collectively, these studies underscore the importance of explicitly accounting for disturbance torques—particularly those induced by reaction wheel imbalance—during the modeling and control design phases. The coupling between these torques and fluid sloshing effects necessitates the use of integrated dynamic models and robust control strategies capable of managing multiple, nonlinear, and time-varying uncertainties.

2.2.3 Control Strategies in Sloshing-Affected Systems

The design of control strategies for satellites affected by fuel sloshing requires methods capable of dealing with nonlinearity, uncertainties, and potential couplings between subsystems. Several recent studies have proposed advanced control techniques, often combining robustness and adaptivity, to ensure stability and performance under such conditions.

??) present a fuzzy sliding mode control strategy applied to a nonlinear coupled spacecraft-fuel system. The method combines the robustness of sliding mode control with the adaptability of fuzzy logic, allowing it to handle modeling uncertainties and parameter variations effectively. Their results demonstrate that this hybrid approach significantly reduces attitude deviation caused by sloshing and external disturbances.

??) develop a fuzzy control technique based on Linear Matrix Inequalities (LMI), which enables the synthesis of controllers that guarantee stability and performance criteria even in the presence of sloshing-induced perturbations. The approach proves to be computationally efficient and suitable for embedded systems onboard small satellites.

??) propose an adaptive prediction backstepping controller to manage attitude regulation in the presence of fuel sloshing and other dynamic uncertainties. The control scheme adapts in real time to variations in system parameters, offering robust tracking performance even under aggressive maneuvers.

Other works, such as **??**), investigate $\mathcal{H}_\infty$ and μ-synthesis techniques for rendezvous and docking scenarios involving nanosatellites. These robust control methods are particularly effective in minimizing the worst-case effects of sloshing torques and actuator limitations.

In summary, the state of the art in control strategies for sloshing-affected systems shows a consistent interest in hybrid, adaptive, and robust methods. These techniques aim to ensure stability and precision in dynamic operational environments, particularly under conditions of large-amplitude sloshing, parameter uncertainty, and actuator imperfections.

Among robust control strategies, Sliding Mode Control (SMC) has been widely investigated for its ability to handle matched uncertainties and nonlinearities, including in spacecraft applications affected by fuel sloshing. Navabi et al. present two significant contributions in this area. In (**??**), they model the nonlinear interaction between spacecraft dynamics and internal fuel slosh using a two-pendulum approach, and propose active nonlinear controllers, including SMC, to regulate the attitude while suppressing fluid oscillations. Later, in (**??**), they extend the methodology by introducing an Optimal Fuzzy Sliding Mode (OFSM) controller. This hybrid technique integrates fuzzy logic and SMC, with gain optimization performed via Particle Swarm Optimization (PSO), achieving improved suppression of sloshing effects during orbital maneuvers.

Additional studies have addressed the application of SMC to underactuated and slosh-sensitive systems. **??**) and **??**) developed SMC-based strategies with tailored nonlinear sliding surfaces to achieve slosh-free motion in constrained mechanical systems. These approaches are relevant for space missions where minimizing fluid motion is critical to maintaining precise attitude control.

Collectively, these works demonstrate that SMC remains a robust and viable solution in the context of sloshing, offering effective control even in the presence of significant model uncertainties and coupled dynamics.

The State-Dependent Riccati Equation (SDRE) method has been explored as an effective approach for controlling nonlinear systems, including satellite attitude control. Unlike traditional linear techniques, SDRE preserves the nonlinear structure of the system, offering flexibility in controller design through state-dependent weighting matrices.

??) developed a satellite attitude control system based on reaction wheels using the SDRE method implemented in Java. The constructed 3D simulator allowed for the evaluation of the controller's performance in typical missions of the National Institute for Space Research (INPE), demonstrating the SDRE's effectiveness in stabilizing the satellite in three axes during maneuvers.

Additionally, **??**) investigated the effects of sloshing dynamics on the performance of satellite attitude control systems. Although the study employed LQR and

LQG methods, the authors emphasized the importance of considering nonlinear approaches, such as SDRE, to address the perturbations introduced by the interaction between fluid motion and satellite dynamics.

These studies reinforce the viability of the SDRE method as a robust alternative for satellite attitude control, especially in scenarios involving significant nonlinearities and dynamic uncertainties.

In this thesis, both SMC and SDRE (with time-delay compensation) are implemented and evaluated on a nonlinear coupled model of satellite attitude dynamics affected by fuel sloshing and reaction wheel imbalance. These control strategies were selected based on their mathematical compatibility with the nonlinear characteristics of the model and their documented performance in related contexts. The comparative assessment—presented in Chapter **??**—provides quantitative insights into their effectiveness in terms of stability, disturbance rejection, and control effort under realistic operating conditions.

2.3 Summary and Research Gaps

This section provided a comprehensive review of the literature concerning the modeling and control of spacecraft attitude dynamics under the influence of internal sloshing and reaction wheel disturbances. It examined historical and recent contributions, highlighting various approaches to model analogies, nonlinear couplings, and control strategies.

The reviewed works demonstrate that while simplified pendulum models remain useful for preliminary analysis and controller design, there is a growing emphasis on more realistic nonlinear and coupled formulations. These include flexible-body dynamics, detailed fluid-structure interactions, and advanced disturbance modeling. From a control perspective, recent advances integrate robust, adaptive, and intelligent methods to manage the nonlinear behaviors introduced by sloshing and actuator imperfections. Despite this progress, many challenges remain, especially in integrating all these effects into a unified, computationally efficient framework.

A key gap identified is the limited number of studies that jointly address large-

amplitude sloshing, structural flexibility, and internal torque disturbances from unbalanced actuators in a nonlinear and experimentally validated context. Furthermore, most control designs rely on high-fidelity CFD models, which are computationally intensive and difficult to generalize for onboard implementation.

This thesis addresses these limitations by proposing a nonlinear reduced-order model focused on pitch dynamics—arguably the most sensitive axis to slosh-induced torques. The model captures essential features of internal fluid motion and actuator asymmetries in a compact, analytically tractable form. It supports the use of nonlinear analysis tools such as Poincaré maps and Lyapunov exponents and enables the design and evaluation of advanced control strategies under realistic mission scenarios.

3 Mathematical Modeling

This chapter introduces a comprehensive nonlinear mathematical model that describes the attitude dynamics of a satellite subjected to internal fluid sloshing and reaction wheel imbalance. The modeling framework is grounded in the formulations presented by **??**), **??**), and **??**), which utilize Lagrangian mechanics to capture the dynamic behavior of coupled rigid-body and fluid systems. Kinetic coupling terms and potential energy interactions are systematically included for the rigid body, the equivalent fluid model, and the actuator subsystems. Contributions from (**??**) and (**??**) are further incorporated to account for unbalanced torques generated by reaction wheels and damping effects inherent to the sloshing motion.

The primary modeling objective is to characterize the interaction between the rigid satellite platform and the internal fluid sloshing, which is represented using an equivalent mechanical pendulum. This pendulum consists of a point mass connected to the satellite through a pivot, effectively capturing the dominant dynamic effects of fluid sloshing—specifically, its inertial, restoring, and dissipative contributions acting on the spacecraft's structural frame.

3.1 Hypotheses and Model Restrictions

The dynamic model is constructed using two generalized coordinates: $\psi(t)$, representing the satellite's pitch angle about a principal axis, and $\theta(t)$, denoting the relative angular displacement of a pendulum that models the sloshing of internal fluid. The rotational motion of the satellite is described within a planar framework, whereas the internal fluid dynamics are represented by the oscillatory response of the pendulum, influenced by both gravitational and inertial coupling effects. This coordinate selection ensures a physically meaningful and analytically manageable formulation of the coupled rigid-body–fluid interaction.

Figure 8 – Schematic diagram of the satellite-fluid system with sloshing, represented by an internal pendulum.

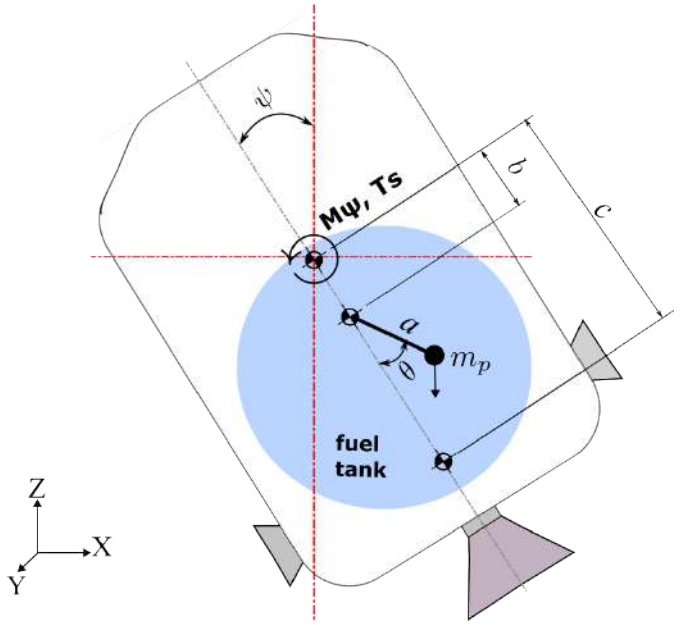

Source: The Author, 2025.

Table 1 – Description of variables used in the satellite–fluid dynamic model

Symbol	Description	Unit
$\psi(t)$	Satellite pitch angle	[rad]
$\theta(t)$	Pendulum (sloshing) angle	[rad]
m_p	Pendulum/sloshing mass	[kg]
m_f	Fixed mass (structure + residual fluid)	[kg]
a	Pendulum length	[m]
b	Distance from pivot to CoM	[m]
c	Distance from fixed mass to CoM	[m]
g	Gravitational acceleration	[m/s^2]
M	Control torque	[N·m]
$T_s(t)$	Disturbance torque (imbalance)	[N·m]

Source: The Author, 2025.

The model is derived in its full nonlinear form, avoiding any small-angle

approximations, thereby preserving all trigonometric nonlinearities. As a result, the formulation accounts for large angular excursions in pitch, making it suitable for scenarios involving significant attitude variations.

Figure **??** and Table **??** present the physical configuration and define the key variables used in the model. The satellite is treated as a rigid body referenced to two coordinate frames: one inertial (fixed to Earth) and one body-fixed. The pendulum mass m_p, located at a distance a from the pivot, models sloshing, while the fixed mass m_f incorporates structural and static fluid contributions. The distances b and c define the geometric relationships to the system's center of mass. Torques M and $T_s(t)$ represent the active control input and reaction wheel imbalance, respectively.

The model incorporates external torques and actuator-induced disturbances, particularly those associated with unbalanced reaction wheels, which contribute to the system's nonlinear behaviour. The formulation proceeds with the definition of generalised coordinates, computation of kinetic and potential energies, and construction of the Lagrangian function. By applying the Euler–Lagrange equations, the resulting system of coupled nonlinear differential equations governs the time evolution of the dynamic variables.

In addition to inertial terms, the model incorporates dissipative forces representing energy losses associated with fluid motion, such as viscous effects and friction between the fluid and the tank walls. Considering these effects is essential to accurately represent the natural damping of oscillations and to provide a basis for controller design.

In the following sections, the detailed derivation of the equations of motion will be presented, along with the description of the terms that compose the dynamic system, laying the foundation for the stability and control analyses that will be developed in the subsequent chapters.

3.2 Lagrangian Formulation

To describe the motion of the satellite-fluid system with internal oscillatory dynamics, the Lagrangian approach was adopted in which two internal components

are modeled: a sloshing mass represented by a pendulum, and a fixed mass located at a constant distance from the center of rotation.

The total kinetic energy of the system is composed of two parts: the kinetic energy of the rigid body of the satellite and the kinetic energy of the fluid mass represented by the pendulum. Similarly, the total potential energy consists of the gravitational potential energy associated with the pendulum mass. These energies are derived in the next subsection to construct the Lagrangian $\mathcal{L} = T - V$.

3.2.1 Relative Positions and Velocities

Let $\theta(t)$ be the pitch angle of the satellite and $\psi(t)$ the angular displacement of the sloshing mass relative to the satellite. The following notation is adopted:

a: length of the pendulum (distance from the pivot to the pendulum mass)

b: offset from the satellite's center of mass to the pivot point along the structure

c: distance of the fixed mass from the pivot (representing an asymmetry)

x_p, z_p: inertial position of the sloshing (pendulum) mass

x_f, z_f: inertial position of the fixed internal mass

The position of the pendulum mass is given in inertial coordinates as:

$$x_p = (a\cos\theta + b)\sin\psi + a\sin\theta\cos\psi \tag{3.1}$$

$$z_p = (a\cos\theta + b)\cos\psi - a\sin\theta\sin\psi \tag{3.2}$$

These expressions result from composing the rotation $\theta(t)$ of the satellite with the rotation $\psi(t)$ of the pendulum with respect to the satellite.

3.2.1.1 Fixed Mass Position

The position of the fixed internal mass is defined in a similar way, but since its location is fixed with respect to the body axis and it only undergoes the ψ rotation:

$$x_f = c\sin\psi \tag{3.3}$$

$$z_f = c\cos\psi \tag{3.4}$$

3.2.1.2 Absolute Velocities

To obtain the kinetic energy, the absolute velocities of the pendulum and fixed masses are computed. This includes both relative motion and the transport term due to the rotation of the satellite.

Let $\dot{\psi} = \frac{d\psi}{dt}$ and $\dot{\theta} = \frac{d\theta}{dt}$ denote the angular velocities. Then, the absolute velocity components are:

$$v_{x_p} = \frac{d}{dt}(x_p) + \dot{\psi} z_p \tag{3.5}$$

$$v_{z_p} = \frac{d}{dt}(z_p) - \dot{\psi} x_p \tag{3.6}$$

$$v_{x_f} = \frac{d}{dt}(x_f) + \dot{\psi} z_f \tag{3.7}$$

$$v_{z_f} = \frac{d}{dt}(z_f) - \dot{\psi} x_f \tag{3.8}$$

These terms account for both the local time derivatives of x_p, z_p, x_f, and z_f, and the additional convective (Coriolis-like) components associated with the rotation $\dot{\psi}$ around the satellite's body axis.

3.2.2 Total Kinetic Energy of the System

The total kinetic energy T is composed of four terms: translational kinetic energy of the sloshing (pendulum) mass (T_p), Translational and rotational kinetic energy of the fixed mass (T_f and T_{fix}), and rotational kinetic energy of the satellite.

3.2.2.1 Kinetic Energy of the Pendulum Mass

Let m_p be the mass of the pendulum. Using the expanded velocity components v_{x_p} and v_{z_p}, the translational kinetic energy is:

$$T_p = \frac{1}{2} m_p \left(v_{x_p}^2 + v_{z_p}^2 \right) \tag{3.9}$$

3.2.2.2 Kinetic Energy of the Fixed Mass

Let m_f be the fixed mass, located at a distance c from the axis of rotation. Its translational and rotational kinetic energies are:

$$T_f = \frac{1}{2} m_f \left(v_{x_f}^2 + v_{z_f}^2 \right) \tag{3.10}$$

$$T_{\text{fix}} = \frac{1}{2} I_f (\dot{\theta} + \dot{\psi})^2 = \frac{1}{2} m_f c^2 (\dot{\theta} + \dot{\psi})^2 \tag{3.11}$$

3.2.2.3 Rotational Kinetic Energy of the Satellite

Assuming the satellite has moment of inertia I_{sat} and rotates with angular velocity $\dot{\psi}$, its kinetic energy is:

$$T_{\text{sat}} = \frac{1}{2} I_{\text{sat}} \dot{\psi}^2 \tag{3.12}$$

3.2.2.4 Total Kinetic Energy

Summing all contributions:

$$T = T_p + T_f + T_{\text{sat}} + T_{\text{fix}} \tag{3.13}$$

Or explicitly:

$$T = \frac{1}{2} m_p (v_{x_p}^2 + v_{z_p}^2) + \frac{1}{2} m_f (v_{x_f}^2 + v_{z_f}^2) + \frac{1}{2} I_{\text{sat}} \dot{\psi}^2 + \frac{1}{2} m_f c^2 (\dot{\theta} + \dot{\psi})^2 \tag{3.14}$$

This expression accounts for all the motion in the system, and will be used next to construct the Lagrangian function and derive the equations of motion.

3.2.3 Potential Energy

The total potential energy V of the coupled satellite–pendulum system comprises gravitational and elastic components:

$$V = V_{\text{grav}} + V_{\text{elas}} = m_p\, g\, z_p + m_f\, g\, z_f + \frac{1}{2}\, k_\psi\, \psi^2 + \frac{1}{2}\, k\, \theta^2 \tag{3.15}$$

where:

- m_p and m_f are the pendulum and fluid equivalent masses, respectively;
- g is the gravitational acceleration;
- z_p and z_f denote the vertical positions of the pendulum mass and fluid center of mass;
- k_ψ is the structural stiffness associated with the satellite attitude coordinate ψ;
- k is the equivalent stiffness of the slosh mode θ.

This potential energy expression is then used to define the Lagrangian:

$$\mathcal{L}(\psi, \dot{\psi}, \theta, \dot{\theta}) = T(\psi, \dot{\psi}, \theta, \dot{\theta}) - V(\psi, \theta) \tag{3.16}$$

which forms the basis for deriving the nonlinear equations of motion via the Euler–Lagrange formalism.

3.2.3.0.1 Note on Gravitational Acceleration.

To allow for future extensions of the model to different orbital altitudes, the gravitational acceleration g can be generalized by the Newtonian formula:

$$g(h) = \frac{GM_E}{(R_E + h)^2}, \tag{3.17}$$

where G is the universal gravitational constant, M_E is the Earth's mass, R_E is the Earth's radius, and h is the altitude of the satellite above the surface.

In this study, a constant value of $g = 8.7\ \mathrm{m/s^2}$ was used to approximate conditions at a reference altitude. However, Equation **??** can be directly incorporated into the potential energy formulation to accommodate simulations at different orbital heights.

3.2.4 Equation of Motion for ψ

The equation of motion corresponding to the generalized coordinate ψ, which describes the angular displacement of the satellite with respect to an inertial reference frame, is derived from the Euler-Lagrange formulation. In this model, the coordinate ψ is influenced by a control torque M_ψ and a disturbance torque T_s, the latter resulting from the unbalanced dynamics of the reaction wheels. The general Euler-Lagrange equation for ψ with external torques is:

$$\frac{d}{dt}\left(\frac{\partial \mathcal{L}}{\partial \dot{\psi}}\right) - \frac{\partial \mathcal{L}}{\partial \psi} = M_\psi + T_s \tag{3.18}$$

where:
- $\mathcal{L} = T - V$ is the Lagrangian;
- M_ψ is the control torque applied to the satellite;
- T_s represents the torque induced by the unbalanced dynamics of the reaction wheels;

Figure **??** illustrates a schematic of a reaction wheel with static imbalance, where a small mass m_s mounted on the rim of the flywheel generates a centrifugal force F_s as it rotates at angular speed ω_s.

Figure 9 – Schematic model of a reaction wheel with static imbalance. A small mass m_s is mounted on the rim of the flywheel, producing a centrifugal force F_s as the wheel rotates with angular velocity ω_s.

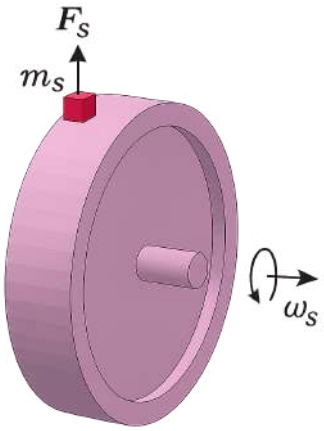

Source: Adapted from Bayard (2010) (**??**). Illustration by the author.

To model this disturbance torque, we consider an eccentric mass m_s located at a radial distance ρ from the axis of rotation of the reaction wheel. The centrifugal force acting on this mass is given by:

$$F_s(t) = m_s \rho \omega_s^2 \sin(\omega_s t + \phi_s) \tag{3.19}$$

where:

- m_s [kg]: mass of the eccentric element mounted on the rim of the wheel;
- ρ [m]: radial distance from the axis of rotation to the mass m_s;
- ω_s [rad/s]: angular velocity of the reaction wheel;
- ϕ_s [rad]: phase offset at $t = 0$;
- $F_s(t)$ [N]: instantaneous centrifugal force acting on the eccentric mass.

This force induces a torque about the satellite's center of mass due to the offset ℓ between the wheel axis and the satellite's reference point:

$$T_s(t) = m_s \rho \ell \, \omega_s^2 \sin(\omega_s t + \phi_s) \tag{3.20}$$

where:

- ℓ [m]: distance from the reaction wheel to the satellite's center of mass;
- $T_s(t)$ [N·m]: torque applied to the satellite due to static imbalance.

By defining the **static imbalance coefficient** as $C_s = m_s \rho \ell$ [kg·m^2], the disturbance torque can be written compactly as:

$$T_s(t) = C_s \, \omega_s^2 \sin(\omega_s t + \phi_s) \tag{3.21}$$

Equation (**??**) captures the periodic nature of the disturbance, which directly impacts the pitch axis dynamics and must be considered in robust control design, especially in missions requiring fine pointing accuracy (**??**).

The equation of motion for the satellite angle $\psi(t)$ is:

$$\begin{aligned}
&(I_{\text{sat}} + 4a^2 m_p + 4b^2 m_p + 5c^2 m_f + 8abm_p \cos\theta)\ddot{\psi} \\
&+ (2a^2 m_p + c^2 m_f + 2abm_p \cos\theta)\ddot{\theta} \\
&- 8abm_p \sin\theta \dot{\psi}\dot{\theta} - 2abm_p \sin\theta \dot{\theta}^2 \\
&- agm_p \sin(\psi + \theta) - bgm_p \sin\psi - cgm_f \sin\psi + k_\psi \psi = M_\psi + T_s
\end{aligned} \tag{3.22}$$

3.2.5 Equation of Motion for $\theta(t)$

The coordinate $\theta(t)$ describes the angular displacement of the internal pendulum-like mass (sloshing fluid) relative to the satellite body. This coordinate is not directly actuated by control inputs, but is affected by the satellite's motion and by internal restoring and damping forces.

The equation of motion is obtained by applying the extended Euler-Lagrange formulation, including the Rayleigh dissipation function $\mathcal{D} = \frac{1}{2}\epsilon_\theta \dot{\theta}^2$, associated with internal fluid damping:

$$\frac{d}{dt}\left(\frac{\partial \mathcal{L}}{\partial \dot{\theta}}\right) - \frac{\partial \mathcal{L}}{\partial \theta} + \epsilon_\theta \dot{\theta} + k\,\theta = 0 \tag{3.23}$$

Therefore, the equation of motion for the pendulum angle $\theta(t)$ is

$$\begin{aligned}
&(2a^2 m_p + c^2 m_f + 2abm_p \cos\theta)\,\ddot{\psi} + (a^2 m_p + c^2 m_f)\,\ddot{\theta} + \epsilon\,\dot{\theta} \\
&\quad + 4abm_p \sin\theta\,\dot{\psi}^2 - agm_p \sin(\psi + \theta) + k\,\theta = 0
\end{aligned} \tag{3.24}$$

This equation describes the nonlinear dynamics of the sloshing fluid and its interaction with the satellite structure.

Equations **??** and **??** describe the coupling between the satellite's rotational motion and the sloshing behavior of the internal fluid, and they incorporate both control and disturbance torques. The terms $k\theta$ and $\epsilon\dot{\theta}$ model the restoring and damping effects of the fluid, respectively. The system is nonlinear due to the trigonometric and multiplicative coupling terms, and it serves as the foundation for the subsequent dynamic analysis and control strategies.

3.2.6 Disturbance Torque from Unbalanced Reaction Wheels

Reaction wheels are commonly used in satellites for attitude control. However, small manufacturing or mounting imperfections may cause their center of mass to be slightly offset from the axis of rotation. This leads to a periodic disturbance torque acting on the satellite's structure — known as imbalance torque — which can adversely affect attitude stability and pointing accuracy (**????????**).

The disturbance torque caused by this imbalance can be modeled as:

$$T_s(t) = C_s \omega_s^2 \sin(\omega_s t + \phi_s) \tag{3.25}$$

where:

C_s is the imbalance coefficient, related to the mass distribution offset;

ω_s is the angular velocity of the reaction wheel (in rad/s);

ϕ_s is the initial phase, accounting for the starting orientation of the rotor.

Equation (**??**) provides a practical approximation of the torque generated by a reaction wheel with small mass imbalance. This modeling is widely used in high-fidelity simulations of spacecraft dynamics and is essential when investigating the interaction between internal actuation and fluid sloshing.

3.2.7 Matrix Form

The nonlinear equations of motion derived in the previous section can be expressed in matrix form as:

$$\mathbf{M}(\theta)\,\ddot{\mathbf{q}} + \mathbf{C}(\theta, \dot{\theta})\,\dot{\mathbf{q}} + \mathbf{K}_\mathbf{r}(\psi, \theta)\mathbf{q} = \boldsymbol{\tau}(\psi, \theta, \dot{\psi}, t) \tag{3.26}$$

with the generalized coordinates:

$$\mathbf{q}(t) = \begin{bmatrix} \psi(t) \\ \theta(t) \end{bmatrix}, \quad \dot{\mathbf{q}}(t) = \begin{bmatrix} \dot{\psi}(t) \\ \dot{\theta}(t) \end{bmatrix}, \quad \ddot{\mathbf{q}}(t) = \begin{bmatrix} \ddot{\psi}(t) \\ \ddot{\theta}(t) \end{bmatrix}$$

The matrices and force vector are defined as follows:

Inertia matrix:

$$\mathbf{M}(\theta) = \begin{bmatrix} I_{\text{sat}} + 4a^2 m_p + 4b^2 m_p + 5c^2 m_f + 8abm_p \cos(\theta) & 2a^2 m_p + c^2 m_f + 2abm_p \cos(\theta) \\ 2a^2 m_p + c^2 m_f + 2abm_p \cos(\theta) & a^2 m_p + c^2 m_f \end{bmatrix} \tag{3.27}$$

Dissipative matrix:

$$\mathbf{C}(\theta, \dot{\theta}) = \begin{bmatrix} -8abm_p \sin(\theta)\dot{\theta} & -2abm_p \sin(\theta)\dot{\theta} \\ 0 & -\epsilon \end{bmatrix} \tag{3.28}$$

Restorative forces:

$$\mathbf{K_r}(\psi, \theta) = \begin{bmatrix} k_\psi & 0 \\ 0 & k \end{bmatrix} \tag{3.29}$$

Generalized force vector:

$$\boldsymbol{\tau}(t) = \begin{bmatrix} M_\psi + T_s(t) + agm_p \sin(\psi + \theta) + bgm_p \sin(\psi) - cgm_f \sin(\psi) \\ agm_p \sin(\psi + \theta) - 4abm_p \sin(\theta)\dot{\psi}^2 \end{bmatrix} \tag{3.30}$$

This formulation highlights the nonlinear coupling between the rigid body and fluid dynamics. The structure of $\mathbf{M}(\theta)$ and $\mathbf{C}(\theta, \dot{\theta})$ captures the parametric dependence on θ, which plays a central role in the system's stability and resonance behavior.

4 Numerical Simulation and Results Analysis

This chapter presents the numerical simulation framework and analyzes the dynamic response of the coupled satellite–fluid system formulated in Chapter **??**. The model comprises a rigid satellite carrying a partially filled propellant tank, whose internal sloshing is represented by an equivalent pendulum. Our objectives are to quantify the influence of fluid slosh on satellite attitude dynamics and to evaluate the effects of reaction-wheel–induced disturbance torques. The governing equations—derived via Lagrangian mechanics and encompassing both kinetic coupling and potential energy terms—are integrated using a fixed-step, fourth-order Runge–Kutta scheme. Subsequent sections detail the simulation parameters and numerical methods, followed by time-domain, spectral, Lyapunov, Poincaré, and parametric energy analyses of the system's behavior.

4.1 Methods, Techniques, and Parameters Employed

The system's ordinary differential equations were solved using the fourth-order Runge-Kutta (RK4) method with a fixed integration step, ensuring stability and accuracy of the simulations.

All code was implemented in `Julia` and `Python`, using libraries specific to data manipulation, numerical integration, and graphical representation. The satellite-fluid system parameters (Table **??**) were chosen to realistically represent the dynamics of a low Earth orbit satellite with a partially filled fluid tank. These parameters balance physical fidelity and computational feasibility, while enabling the occurrence of nonlinear dynamic behaviors such as oscillations, mode coupling, and transitions to chaotic regimes.

The gravitational acceleration was set to $g = 8.7\ \mathrm{m/s^2}$ to simulate residual gravity effects at 400 km altitude. The fluid stiffness coefficient, $k = 500.0\ \mathrm{N/m}$, and

the stiffness associated with the degree of freedom ψ, $k_\psi = 90.0\ \mathrm{N \cdot m/rad}$, were selected based on literature that employs equivalent pendulum models to represent moderate restoring effects in both fluid motion and satellite attitude (**????????**). The satellite's moment of inertia was set to $I_{sat} = 720.0\ \mathrm{kg, m^2}$, a representative value for small research satellites or lightweight orbital platforms (**????**). The control torque applied to ψ was set to $M_\psi = 0.0\ \mathrm{N \cdot m}$ to isolate the system's natural dynamics. The reaction wheel imbalance coefficient $C_s = 1 \times 10^{-7}\ \mathrm{kg \cdot m^2/s}$ and angular velocity $\omega_s = 628.0\ \mathrm{rad/s}$ (approximately $6000\ \mathrm{rpm}$) reflect a realistic operational condition (**????**). The initial phase angle $\phi_s = 0.0^\circ$ assumes alignment with no initial imbalance. Geometric parameters include equivalent pendulum length $a = 0.28\ \mathrm{m}$, and mounting positions $b = -0.19\ \mathrm{m}$ and $c = -0.38\ \mathrm{m}$, based on (**??**). The Rayleigh dissipation coefficient $\epsilon = 0.003\ \mathrm{kg \cdot m^2/s}$ accounts for viscous losses (**??**). Masses are set to $m_p = 190.0\ \mathrm{kg}$ (satellite) and $m_f = 460.0\ \mathrm{kg}$ (fluid), making the fluid a significant contributor to attitude dynamics (**??**).

Together, these parameters define a realistic simulation configuration that enables the observation of nonlinear dynamic behaviors such as bifurcations, quasi-periodicity, and chaotic transitions typical in coupled satellite-fluid systems.

4.2 Simulation Methods and Parameters

The coupled ordinary differential equations derived in Chapter **??** were integrated using a fixed-step, fourth-order Runge–Kutta (RK4) algorithm, chosen for its robust balance between numerical accuracy and computational efficiency. All dynamic simulations were implemented in `Julia`, and post-processing (FFT, Lyapunov, Poincaré maps, plotting) was performed in `Python`, leveraging standard libraries for ODE integration, data management, and graphics.

Table **??** summarizes the physical parameters selected to emulate a low Earth orbit satellite with a partially filled propellant tank. The gravitational acceleration was set to $g = 8.7\ \mathrm{m/s^2}$ to simulate residual gravity effects at 400 km altitude. The fluid pendulum stiffness and attitude spring stiffness are $k = 500\ \mathrm{N/m}$ and $k_\psi = 90\ \mathrm{N\,m/rad}$, respectively, following equivalent-pendulum models in (**????????**). The satellite's moment of inertia is $I_{\mathrm{sat}} = 720\ \mathrm{kg\,m^2}$ (**????**). Reaction-wheel imbalance is

modeled with $C_s = 1 \times 10^{-7}\ \mathrm{kg\,m^2/s}$, $\omega_s = 628\ \mathrm{rad/s}$, and $\phi_s = 0$ (**????**). A small Rayleigh damping coefficient $\epsilon = 0.003\ \mathrm{kg\,m^2/s}$ accounts for viscous losses (**??**). Geometric parameters are $a = 0.28\ \mathrm{m}$, $b = -0.19\ \mathrm{m}$, and $c = -0.38\ \mathrm{m}$ (**??**), with masses $m_p = 190\ \mathrm{kg}$ (pendulum) and $m_f = 460\ \mathrm{kg}$ (fixed mass).

These settings ensure that the simulations capture key nonlinear phenomena—mode coupling, bifurcations, quasi-periodicity, and potential transitions to chaos—while maintaining tractable computational demands.

Table 2 – Main parameters of the satellite-fluid system.

Parameter	**Value**	**Description**
g	$8.7\ \mathrm{m/s^2}$	Gravitational acceleration
k	$500.0\ \mathrm{N/m}$	Fluid stiffness coefficient
k_ψ	$90.0\ \mathrm{N \cdot m/rad}$	Stiffness associated with ψ
I_{sat}	$720.0\ \mathrm{kg\,m^2}$	Satellite moment of inertia
M_ψ	$0.0\ \mathrm{N \cdot m}$	Control torque applied to ψ
C_s	$1 \times 10^{-7}\ \mathrm{kg \cdot m^2/s}$	Reaction wheel damping coefficient
ω_s	$628.0\ \mathrm{rad/s}$	Reaction wheel angular velocity
ϕ_s	$0.0°$	Initial phase angle of the reaction wheel
a	$0.28\ \mathrm{m}$	Equivalent pendulum length
b	$-0.19\ \mathrm{m}$	Pendulum attachment position
c	$-0.38\ \mathrm{m}$	Position relative to the satellite's center of mass
ϵ	$0.003\ \mathrm{kg \cdot m^2/s}$	Rayleigh dissipation coefficient
m_p	$190.0\ \mathrm{kg}$	Pendulum mass (mobile fluid)
m_f	$460.0\ \mathrm{kg}$	Fixed mass of the satellite (rigid body)

Source: The Author, 2025.

The initial conditions considered for the simulation are listed in Table **??**.

Table 3 – Initial conditions adopted in the simulations.

Variable	**Value**	**Description**
$\psi(0)$	$30°$ (0.5236 rad)	Initial satellite angle
$\theta(0)$	$5°$ (0.0873 rad)	Initial fluid angle
$\dot{\psi}(0)$	$0.5\ \mathrm{rad/s}$	Initial angular velocity of the satellite
$\dot{\theta}(0)$	$0.5\ \mathrm{rad/s}$	Initial angular velocity of the fluid

Source: The Author, 2025.

4.3 Time and Spectral Analysis via FFT

This section presents a comprehensive analysis of the temporal and spectral behavior of the primary state variables describing the coupled satellite–fluid dynamic system: the pitch angle ψ, its angular velocity $\dot{\psi}$, the relative angular displacement θ of the equivalent pendulum representing the sloshing fluid, and its corresponding angular velocity $\dot{\theta}$.

Time-domain visualization enables a direct assessment of the temporal evolution of these variables, facilitating the qualitative identification of distinct dynamical patterns — including periodic oscillations, quasi-periodic motions, and chaotic responses, which are typically marked by irregular temporal structures and high sensitivity to initial conditions.

However, pure time-domain inspection may be insufficient for accurately resolving the underlying frequency content, particularly in systems exhibiting multiple coexisting frequencies or complex nonlinear dynamics. To address this limitation, frequency-domain analysis is performed using the Fast Fourier Transform (FFT), allowing decomposition of the temporal signals into their harmonic constituents and providing insight into the energy distribution across different frequency bands.

In periodic systems, the resulting power spectra exhibit discrete, sharply defined peaks at the dominant oscillation frequencies. Quasi-periodic regimes manifest through multiple distinct spectral lines corresponding to incommensurate frequencies, whereas chaotic dynamics are generally characterized by continuous broadband spectra lacking dominant frequency components.

Therefore, a synergistic combination of time- and frequency-domain analyses constitutes a robust methodology for identifying and classifying the prevailing dynamical regime of the system. While time-domain plots offer intuitive insights into the regularity or stochastic nature of the motion, spectral analysis enables quantitative characterization of the dominant frequencies and classification of the oscillatory behavior as periodic, quasi-periodic, or chaotic.

To complement this characterization, the following results incorporate:

- Temporal waveforms of the key variables (ψ, $\dot{\psi}$, θ, $\dot{\theta}$);

- Corresponding frequency spectra derived via FFT;

- Two- and three-dimensional phase portraits.

The temporal and spectral data allow for a preliminary classification of the system's response, while phase-space reconstructions provide a more holistic view of the attractors governing the system dynamics. Regular closed orbits are indicative of periodic motion; toroidal structures point to quasi-periodic behavior; and erratic, non-repeating trajectories filling extended regions of the phase space are typical signatures of chaos. By integrating signal information across time, frequency, and phase space domains, the observed dynamical regimes can be effectively identified and interpreted for each simulation scenario.

4.3.1 Analysis of the Pitch Angle ψ

Figure **??** shows the time evolution of the pitch angle ψ. The signal exhibits regular oscillations over time, with moderate amplitudes and an approximately periodic behavior. No abrupt variations or exponential amplitude growth are observed, indicating stability within the oscillatory regime. Complementarily, Figure **??** presents the corresponding frequency spectrum obtained via FFT. The spectrum displays a dominant peak at a specific frequency, confirming the predominantly periodic nature of the motion. The presence of lower-intensity harmonics suggests mild nonlinearities within the system, without compromising the periodic pattern.

The phase space structure $\psi \times \dot{\psi}$, illustrated in Figure **??**, supports this interpretation. The trajectories form closed and regular orbits around the origin, characteristic of stable periodic motion. No diffused trajectories or chaotic filling of the phase space are observed, confirming the predominance of regular dynamics. Finally, the three-dimensional representation in the ψ, $\dot{\psi}$, and θ space (Figure **??**) highlights the interaction between the satellite motion and the fluid oscillation. Despite this coupling, the three-dimensional structure remains confined around a well-defined orbit, with no evident signs of chaotic behavior.

Figure 10 – Time series and frequency analysis of the satellite's pitch and roll angle and angular velocity.

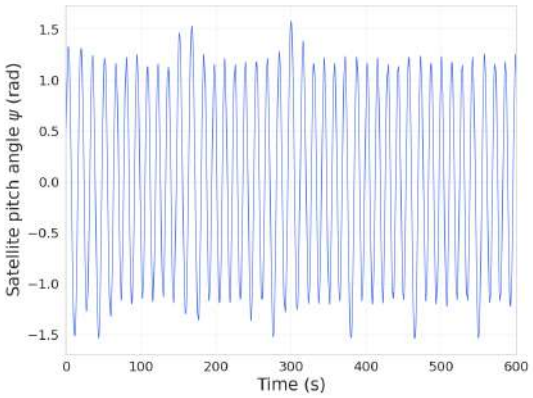

(a) Time evolution of ψ

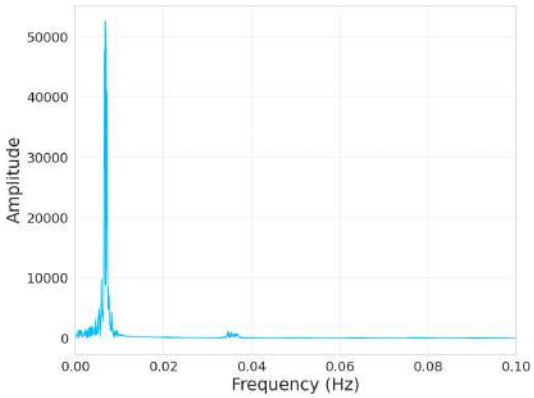

(b) FFT of ψ

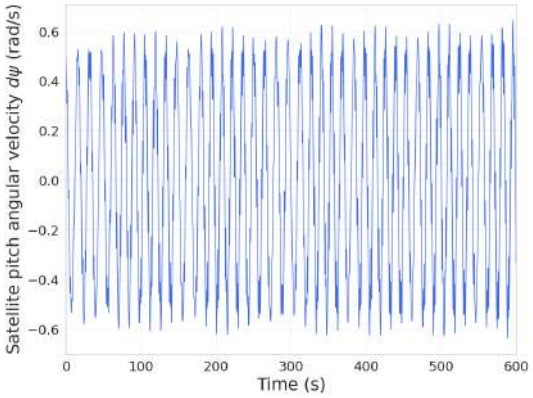

(c) Time evolution of $d\psi$

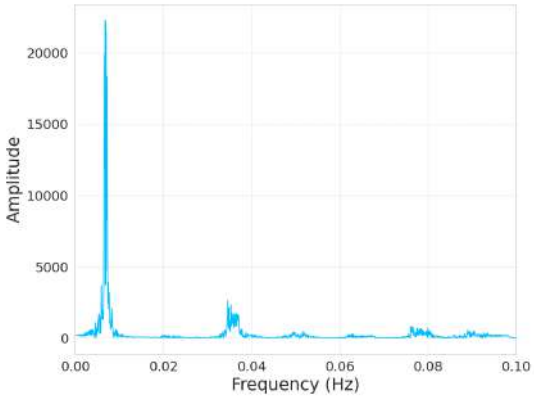

(d) FFT of $d\psi$

Source: The Author, 2025.

Figure 11 – Phase space diagram: ψ vs $d\psi$.

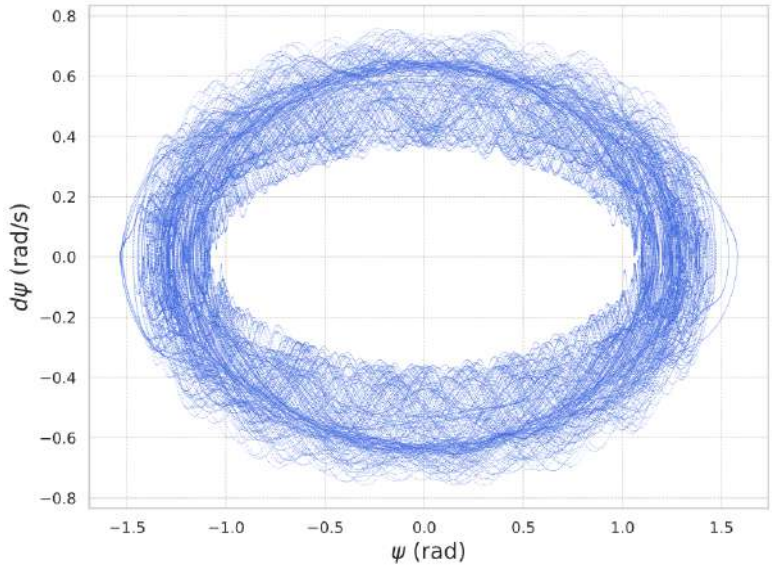

Source: The Author, 2025.

4.3.2 Analysis of the Angular Velocity $\dot{\psi}$

Figure **??** displays the time evolution of the angular velocity $\dot{\psi}$. The behavior is similar to that observed for the variable ψ, exhibiting regular oscillations with stable amplitudes over time. The corresponding frequency spectrum, shown in Figure **??**, confirms the presence of a dominant frequency, consistent with the approximately periodic motion identified in the time evolution. As with the variable ψ, low-intensity harmonics are observed, associated with system nonlinearities. In the $\psi \times \dot{\psi}$ phase space (Figure **??**), the combined trajectory of these variables maintains a structure of closed and regular orbits, with no evidence of chaotic diffusion or irregular filling of the phase space.

These results indicate that the dynamic regime for the variable $\dot{\psi}$ is also predominantly periodic, with limited nonlinear effects and no evident transitions to quasi-periodicity or chaos.

Spectral analysis of the variables ψ and $\dot{\psi}$ reveals, in addition to the dominant fundamental frequency, the presence of second- and third-order harmonics. This behavior indicates that the signals are not purely sinusoidal, but exhibit distortions

Figure 12 – 3D phase space: ψ, $d\psi$, and θ.

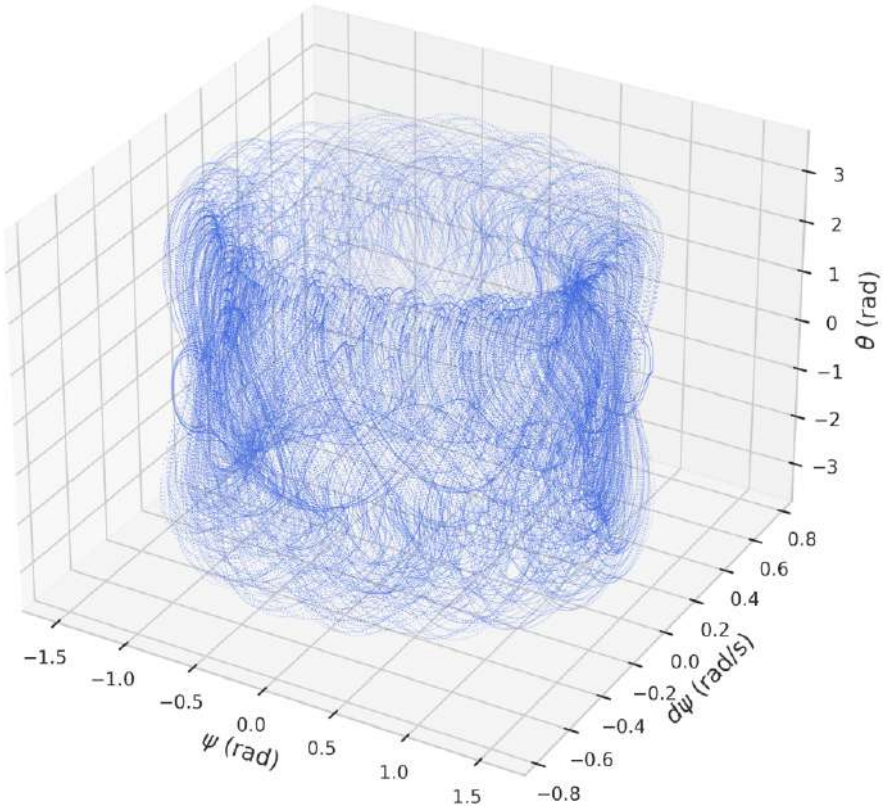

Source: The Author, 2025.

due to the presence of nonlinearities in the dynamic system. Such nonlinearities are attributed to quadratic terms present in the satellite-fluid system's equations of motion, which introduce additional components in the frequency spectrum.

The presence of multiple harmonics suggests that, although the dynamic regime is predominantly periodic, the motion exhibits characteristics typical of nonlinear systems. The time series reveals regular oscillations that are slightly distorted when compared to a purely harmonic motion, which is consistent with the observed spectral distribution.

This analysis supports the interpretation obtained from the $\psi \times \dot{\psi}$ phase space, in which regular trajectories with minor shape variations indicate a periodic motion modified by the influence of internal nonlinear dynamic interactions.

4.3.3 Analysis of the Fluid Oscillation Angle θ

Figure **??** shows the time evolution of the angle θ. The signal exhibits large-amplitude oscillations with visible waveform modulations, suggesting the presence of multiple frequency components. The corresponding frequency spectrum (Figure **??**) confirms this observation, displaying the fundamental frequency accompanied by multiple harmonics and evidence of nonlinear coupling. In the $\theta \times \dot{\theta}$ phase space (Figure **??**), the trajectories do not form simple closed orbits but rather thicker toroidal patterns, characteristic of quasi-periodic or strongly nonlinear motion. These results indicate that the motion of the fluid mass exhibits quasi-periodic oscillation characteristics, associated with dynamic coupling effects and nonlinearities present in the equations of motion of the satellite-fluid system.

4.3.4 Analysis of the Fluid Angular Velocity $\dot{\theta}$

Figure **??** shows the time evolution of the angular velocity $\dot{\theta}$. The signal reflects the characteristics observed for θ, exhibiting large-amplitude oscillations and more variability than observed in $\dot{\psi}$. The corresponding frequency spectrum, shown in Figure **??**, confirms the presence of multiple high-intensity harmonic components. Compared to $\dot{\psi}$, the spectrum of $\dot{\theta}$ displays a broader energy spread around the fundamental frequency, indicating that the fluid mass motion is more significantly affected by nonlinear effects.

The analysis of the $\theta \times \dot{\theta}$ phase space (Figure **??**) reinforces the interpretation of nonlinear and asymmetric dynamics: the trajectories do not concentrate on simple closed orbits but are rather diffusely and irregularly distributed, filling regions of the phase space in a nonuniform manner. This pattern is characteristic of quasi-periodic or transient motion with sensitivity to initial conditions, suggesting a possible transition to chaotic regimes under certain conditions.

These results demonstrate that the behavior of the fluid mass inside the satellite is dominated by complex oscillations, with significant interaction among the dynamic variables, reflecting the importance of sloshing in the overall dynamics of the system.

Figure 13 – Time series and frequency analysis of the sloshing mass angle and angular velocity.

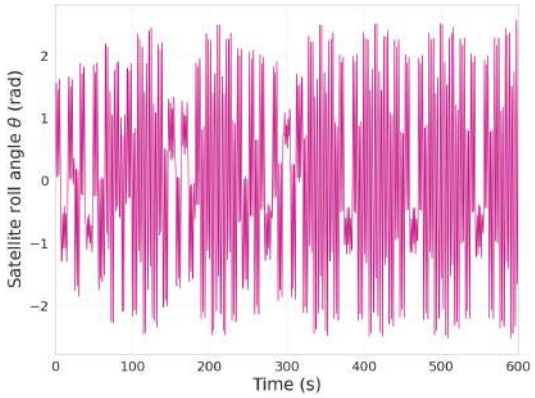

(a) Time evolution of θ

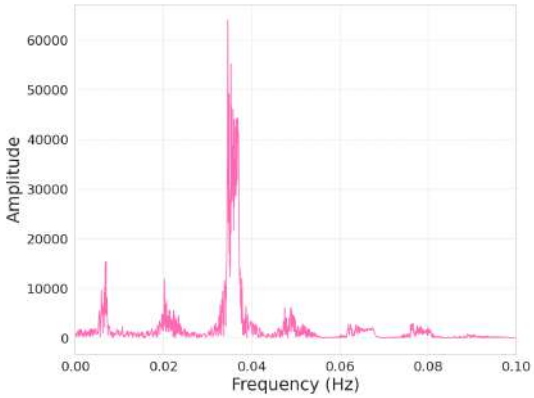

(b) FFT of θ

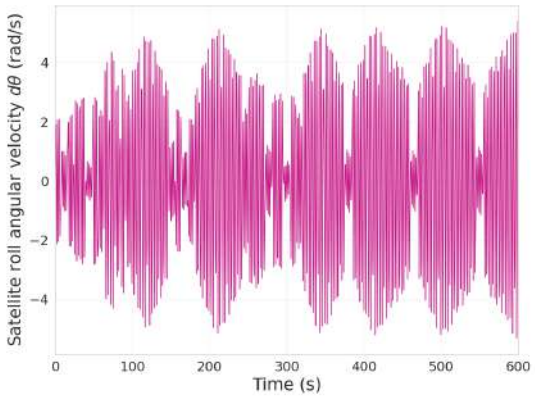

(c) Time evolution of $d\theta$

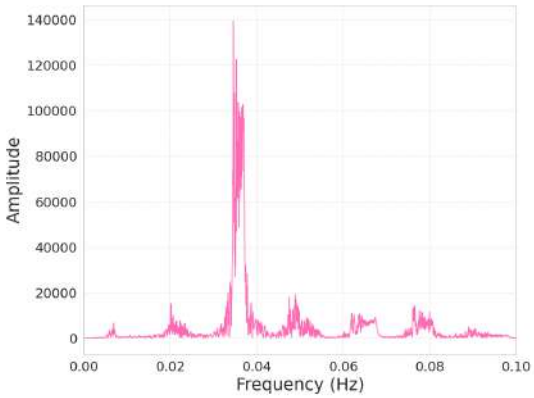

(d) FFT of $d\theta$

Source: The Author, 2025.

Figure 14 – Phase space diagram: θ vs $d\theta$.

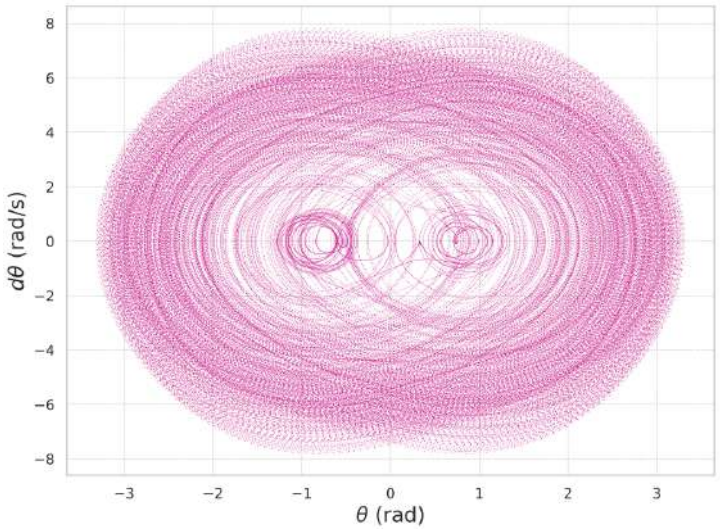

Source: The Author, 2025.

Figure 15 – 3D phase space: θ, $d\theta$, and ψ.

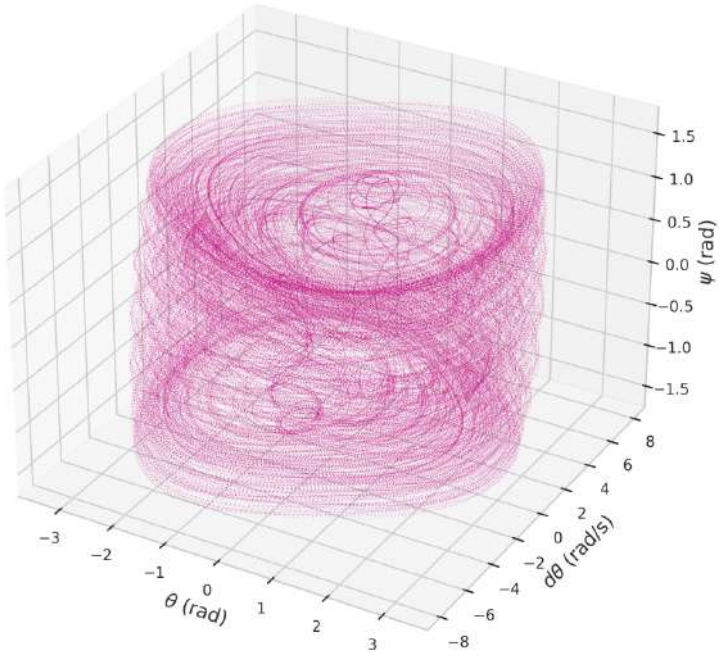

Source: The Author, 2025.

4.4 Lyapunov Exponent Analysis

The time-domain analysis reveals the interaction between the sloshing dynamics and the satellite motion, elucidating phenomena such as quasi-periodic or transient behaviors with sensitivity to initial conditions. These dynamics suggest a possible transition to chaotic regimes under specific conditions. The computation of Lyapunov exponents further quantifies the divergence or convergence of trajectories in phase space, allowing classification of the system's behavior. Specifically, $\lambda > 0$ indicates the presence of chaos with exponential divergence of trajectories, $\lambda = 0$ corresponds to quasi-periodic motion on invariant tori, and $\lambda < 0$ characterizes stable behavior with convergence of trajectories to fixed points or periodic cycles. Lyapunov exponent analysis enables the mapping of chaotic regions and their transitions to stable dynamic regimes.

Figure 16 – Time evolution of the Lyapunov exponents for the variables ψ, $\dot{\psi}$, θ, and $\dot{\theta}$.

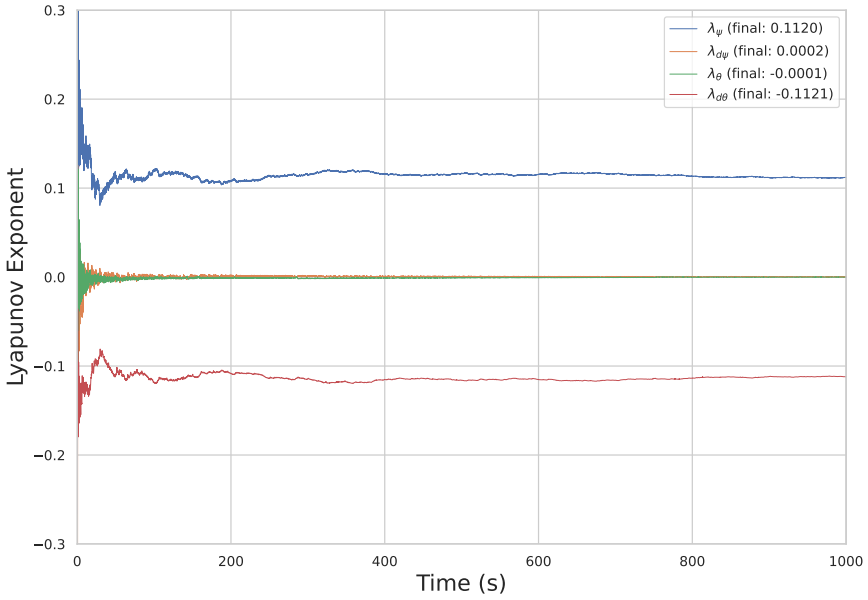

Source: The Author, 2025.

Figure **??** shows the time evolution of the Lyapunov exponents for the state variables ψ, $\dot{\psi}$, θ, and $\dot{\theta}$. The exponent associated with the pitch angle ψ, λ_ψ, converges to a positive value of approximately $+0.1120$, whereas the exponents for $\dot{\psi}$,

θ, and $\dot{\theta}$ remain near zero or negative. A positive λ_ψ indicates local instability in the satellite's pitch dynamics, with nearby trajectories diverging exponentially over finite time intervals.

However, the time series of ψ displays a predominantly quasi-periodic pattern, which warrants caution in definitively classifying the regime as fully chaotic. According to the specialized literature, periodic systems with nonlinear behavior may exhibit positive Lyapunov exponents due to local instabilities, without necessarily presenting global chaos. Furthermore, the presence of Strange Nonchaotic Attractors (SNA) can lead to regions of expansion and contraction in trajectories, resulting in limited-time positive exponents (**??**).

Therefore, the results suggest that the system operates in a mixed dynamic regime: the fluid exhibits predominantly stable or quasi-periodic behavior, whereas the satellite's pitch dynamics motion shows signs of dynamic instability and sensitivity to initial conditions. To further characterize the system's dynamic structure, the analysis continues with the investigation of Poincaré maps. This approach will allow visualization of the trajectory organization in phase space and identification of recurrence patterns, bifurcations, or clearer indicators of transitions to chaotic regimes.

4.5 Poincaré Map Analysis

Continuing the characterization of the dynamics of the satellite-fluid system, we now perform the analysis of Poincaré maps. This tool is essential for visualizing the phase space structure in dynamical systems, enabling the identification of periodic, quasi-periodic, transient, and chaotic behavior regions.

The Poincaré map reduces the original dimensionality of a continuous-time dynamical system by capturing the intersections of trajectories in discrete time with a chosen section surface, effectively removing one of the system's variables (**??**). This technique facilitates a better understanding of the system's global dynamics, revealing fixed points for periodic motion, closed curves for quasi-periodic dynamics, and scattered points for chaotic behavior. Observing structural changes in Poincaré maps also helps elucidate bifurcations and transitions between distinct dynamic

regimes.

Poincaré's contribution to the analysis of dynamical systems was groundbreaking, as he demonstrated that, although the internal interactions of the system cannot be separated, it is possible to eliminate one variable from the equations of motion to simplify the analysis (**??**). In this way, the Poincaré map contributes to highlighting the global dynamic structure of the system, facilitating a broader understanding of its behavior.

There is no universal method for constructing Poincaré maps, but common approaches include defining a specific frequency to sample trajectory points, or slicing the three-dimensional phase space using a plane or section surface (**??**). In this study, the latter approach is adopted, using cross-sections in the phase space with respect to θ and ψ to analyze, respectively, the behavior of the rigid mass of the vehicle and the dynamics of the fluid mass.

Based on previous results, the presence of local instabilities in the satellite's pitch dynamics motion—suggested by the Lyapunov exponent analysis—motivates further investigation through Poincaré maps. The figures presented in the following sections allow direct observation of the trajectory organization in phase space and the identification of patterns indicative of stability, quasi-periodicity, or transitions to chaotic regimes.

4.5.1 Poincaré Maps for the Variable ψ

Figure **??** presents the Poincaré map obtained from the section in θ, showing the dynamics of the variable ψ and its angular velocity $\dot{\psi}$ within a limited range. One can observe the formation of well-defined toroidal structures, which are characteristic of quasi-periodic regimes. There is slight diffusion of the trajectories, indicating the presence of local instabilities, consistent with the previously identified positive Lyapunov exponent. However, the prevailing behavior consists of regular and confined oscillations.

Figure 17 – Zoomed-in Poincaré map: section in θ for the variable ψ. Blue points correspond to $\dot{\psi} > 0$ and grey points to $\dot{\psi} < 0$.

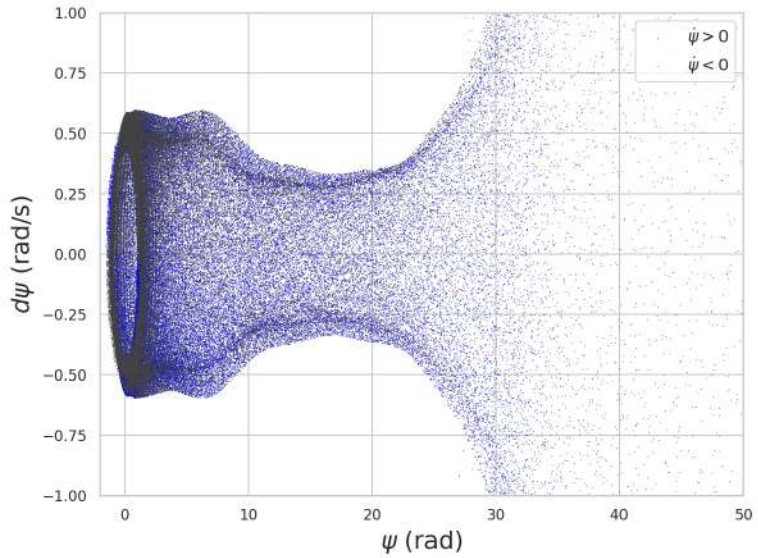

Source: The Author, 2025.

Figure 18 – Full Poincaré map: section in θ for the variable ψ. Blue points correspond to $\dot{\psi} > 0$ and grey points to $\dot{\psi} < 0$.

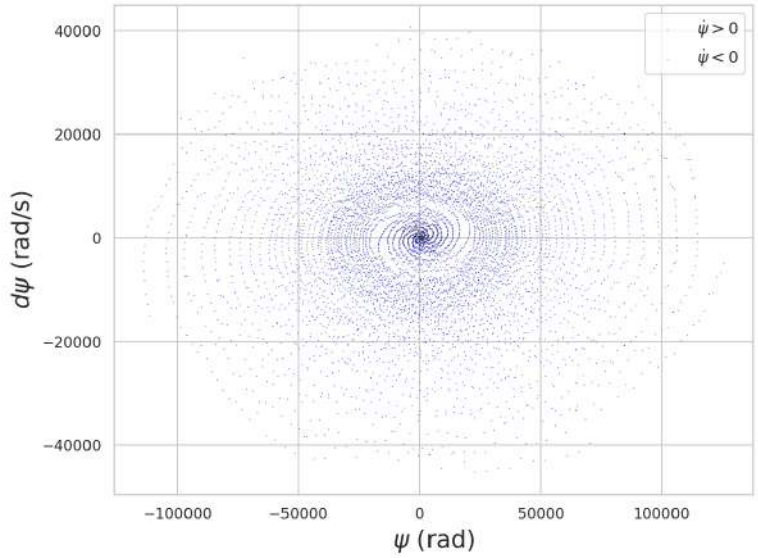

Source: The Author, 2025.

On the other hand, Figure **??** shows the Poincaré map at an expanded scale, highlighting the accumulated drift in the variable ψ. The spiral distribution of trajectories suggests a drift[1] in the pitch dynamics angle, associated with the lack of global confinement in the motion. This behavior is consistent with the possibility of resonance or the presence of unbounded motion components in the system.

The joint analysis of the two Poincaré maps leads to the conclusion that, although the local dynamics of the satellite exhibit quasi-periodic features, the global evolution of ψ is not strictly confined, revealing progressive instabilities resulting from the interaction between the pitch dynamics motion and the fluid displacement.

4.5.2 Poincaré Maps for the Variable θ

Figure **??** shows the zoomed-in Poincaré map for the variable θ and its angular velocity $\dot{\theta}$, within a restricted value range. The trajectories appear dispersed but still exhibit some degree of organization, indicating a quasi-periodic behavior, though with greater amplitude variability compared to the dynamics observed for ψ. This higher dispersion is consistent with the dynamic role of the fluid mass, which, due to its oscillatory nature and interaction with the satellite motion, exhibits wide, non-strictly confined oscillations.

Figure **??** displays the full-scale Poincaré map, revealing the occurrence of continuous drift in θ. The scattering of points across a broad value range confirms that the internal fluid motion does not remain confined around a fixed point but evolves continuously in phase space, reflecting energy transfer and persistent nonlinear interactions.

These results indicate that although the local behavior of the fluid exhibits quasi-periodic characteristics, its global dynamics allow for drift, reinforcing the nonlinear and coupled nature of the satellite-fluid system.

[1] Drift behavior refers to the continuous evolution of a system variable over time, without returning to an initial state or confined interval. Although the local dynamics may be regular, the absolute value of the variable progressively increases or decreases, characterizing a cumulative displacement in phase space.

Figure 19 – Zoomed-in Poincaré map: section in ψ for the variable θ.

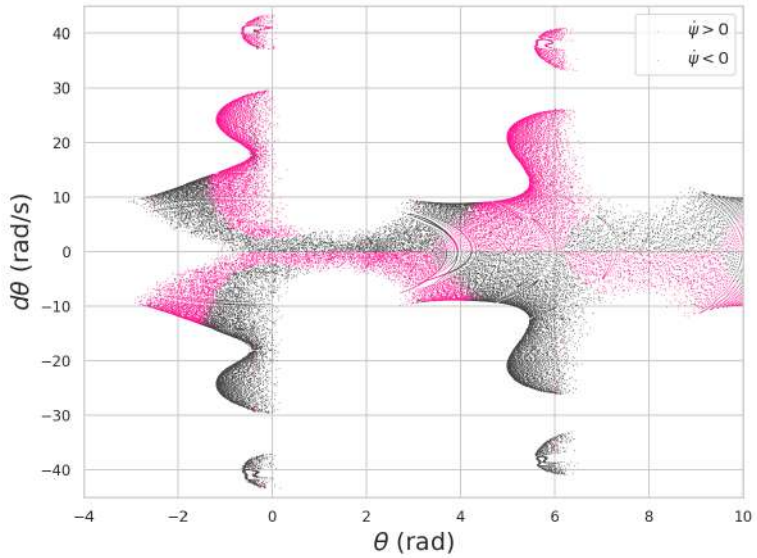

Source: The Author, 2025.

Figure 20 – Full Poincaré map: section in ψ for the variable θ.

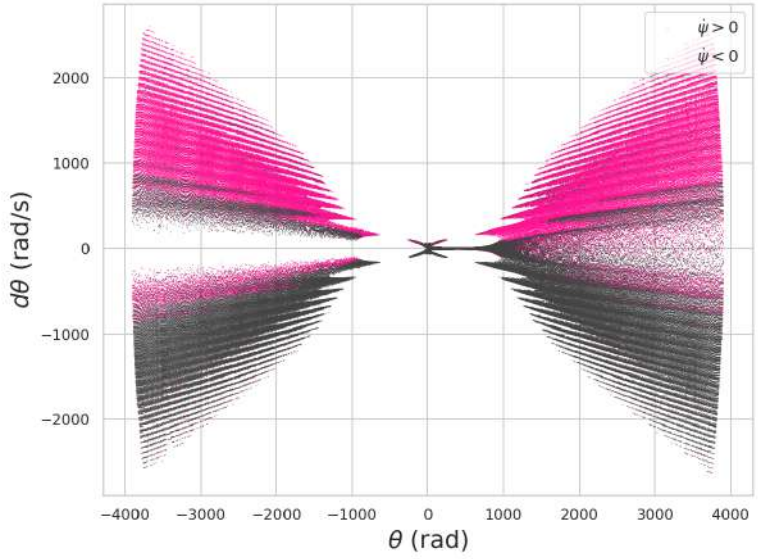

Source: The Author, 2025.

4.6 Parametric Analysis of the System Energy as a Function of Parameters a and b

To assess the influence of parameters a and b (representing, respectively, the pendulum length and the pivot position) on the characteristic energy components of the system, 3D surface plots and 2D heatmaps were generated for each energy type considered: kinetic energy, potential energy, energy associated with the reaction wheels (RW), combined energy of the satellite and fluid, and total system energy. These parameters were chosen because, in the equivalent pendulum model, they represent hypothetical points fixed relative to the satellite's center of gravity, and are therefore estimated during the modeling process. The goal is to demonstrate that careful selection of these parameters is essential, as they can exert significant influence on the system's dynamic behavior.

4.6.1 Kinetic Energy

The 3D surface of kinetic energy (Fig. **??**) reveals that the system exhibits the highest energy peaks for larger values of the pendulum length a, particularly when the pivot is located farther from the center of gravity. The behavior with respect to parameter b is smoother, indicating lower sensitivity to the pivot position. The 2D heatmap (Fig. **??**) supports these observations, showing that the highest concentrations of energy occur in the lower-right region of the (a, b) plane. This result suggests that small variations in the pendulum length can lead to significant changes in the system's kinetic energy, directly impacting its dynamics.

4.6.2 Potential Energy

The 3D surface of potential energy (Fig. **??**) shows a smoother variation compared to kinetic energy, indicating that the system's dependence on parameters a and b is more balanced. It is observed that the potential energy increases gradually for larger values of a, but this behavior is modulated by the influence of the pivot position b.

The 2D heatmap (Fig. **??**) reinforces this interpretation, showing that the

Figure 21 – Kinetic energy maps obtained from the parametric variation of parameters a and b.

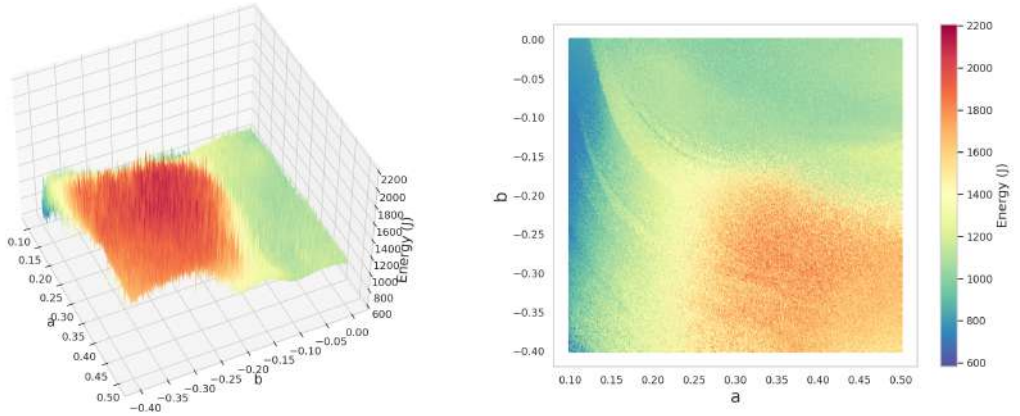

(a) 3D Surface of Kinetic Energy (b) 2D Heatmap of Kinetic Energy

Source: The Author, 2025.

highest magnitudes of potential energy are concentrated in regions with high a and negative b. This behavior is consistent with the system's physics, since increasing the pendulum length, combined with a displacement of the pivot to negative positions relative to the center of gravity, increases the lever arm and enhances the action of gravitational torque. Thus, the geometric configuration directly influences the storage of potential energy in the system.

These results demonstrate that the proper selection of parameters a and b is essential for achieving a desirable dynamic behavior, requiring special attention to the interaction between pendulum length and pivot position during the modeling and control process.

4.6.3 Energy Associated with the Reaction Wheel Imbalance Torque

The 3D surface of the energy associated with the reaction wheel imbalance torque (Fig. **??**) reveals extremely low energy values, on the order of millijoules. The 2D heatmap (Fig. **??**) confirms this observation, displaying a nearly flat surface with only slight variations as a function of parameters a and b.

This energy does not correspond to the rotational energy of the reaction

Figure 22 – Potential energy maps obtained from the parametric variation of parameters a and b.

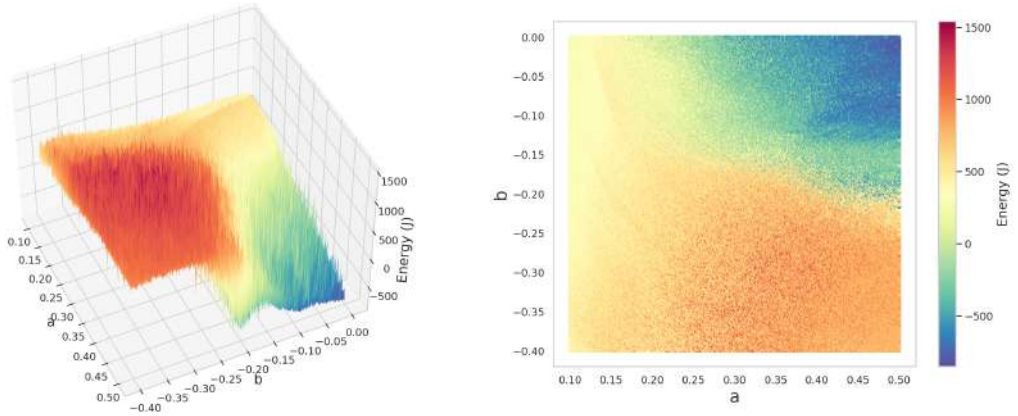

(a) 3D Surface of Potential Energy (b) 2D Heatmap of Potential Energy

Source: The Author, 2025.

wheels themselves, but rather to the perturbation effect generated by their imbalance within the satellite-fluid system. The low magnitude of the energy associated with the imbalance torque indicates that these perturbations are minimal, favoring satellite stability and the precision of pitch dynamics controllers.

Furthermore, since reaction wheels operate electrically, they enable orientation adjustments with high energy efficiency and no consumption of chemical propellant. This characteristic preserves onboard resources such as electrical energy and fuel mass, thereby increasing the system's autonomy and operational lifespan.

4.6.4 Combined Energy of the Satellite and the Fluid

The 3D surface of the combined energy of the satellite and the fluid (Fig. **??**) exhibits a smooth topology, with a gradual increase in energy for higher values of pendulum length a. The 2D heatmap (Fig. **??**) reinforces this trend, showing higher energy concentrations in regions with large a and negative b.

This energy represents the dynamic coupling between the satellite's rigid body and the relative motion of the internal fluid, here modeled as a pendulum. The increase in energy with respect to a is consistent with the amplification of the

Figure 23 – Reaction wheel energy maps obtained from the parametric variation of parameters a and b.

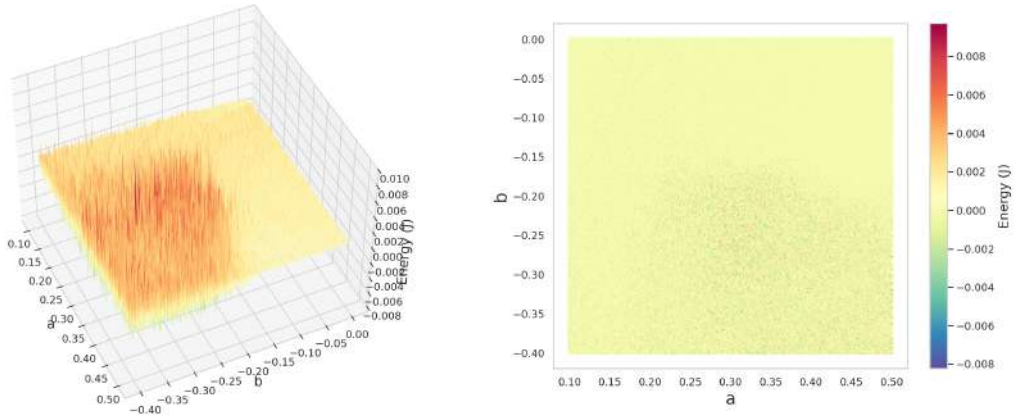

(a) 3D Surface of Reaction Wheel Energy (b) 2D Heatmap of Reaction Wheel Energy

Source: The Author, 2025.

relative motion of the fluid, which becomes more significant for longer pendulums. The parameter b, representing the pivot position relative to the center of gravity, has a more moderate influence but contributes to the redistribution of energy depending on the system's geometry.

These results highlight the importance of careful modeling of parameters a and b, since the combined satellite-fluid energy directly affects the system's stability and dynamic behavior during attitude maneuvers.

4.6.5 Total Energy of the System

The 3D surface of the system's total energy (Fig. **??**) shows a marked increase with the growth of the pendulum length a, reflecting the combined contribution of kinetic, potential, fluid, satellite body, and reaction wheel imbalance energies. The 2D heatmap (Fig. **??**) reinforces this trend, highlighting regions of higher total energy concentrated in zones with large a and negative or intermediate b.

This behavior indicates that the geometric configuration of the system has a direct impact on the amount of energy stored during its operation. The increase in total energy in certain regions of the parametric space may imply higher demands

Figure 24 – Satellite and fluid combined energy maps obtained from the parametric variation of parameters a and b.

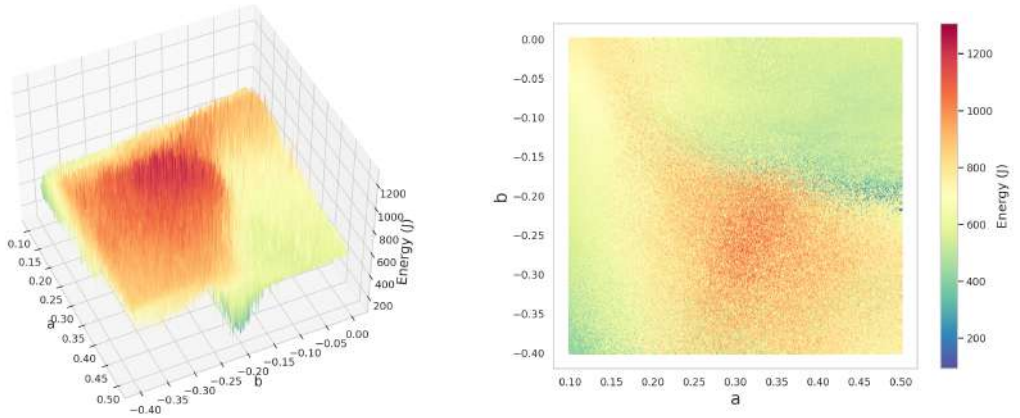

(a) 3D Surface of Satellite + Fluid Energy (b) 2D Heatmap of Satellite + Fluid Energy

Source: The Author, 2025.

on the control actuators and a greater risk of instabilities during attitude maneuvers. Therefore, total energy analysis is essential for identifying safer and more efficient operational zones, supporting proper sizing of control strategies and contributing to the system's longevity.

Figure 25 – Total energy maps obtained from the parametric variation of parameters a and b.

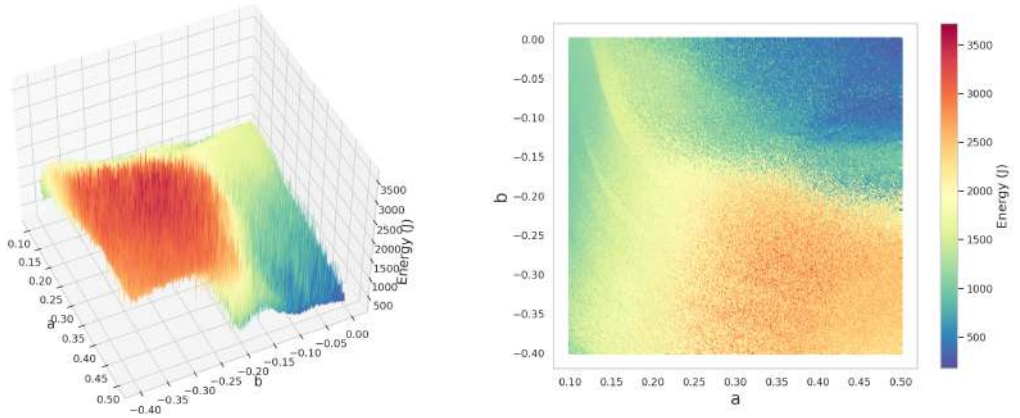

(a) 3D Surface of Total Energy (b) 2D Heatmap of Total Energy

Source: The Author, 2024.

4.7 Extreme Scenario Analysis: $a = 0.35\,\mathrm{m}$, $b = -0.30\,\mathrm{m}$

Based on the energy surfaces and parametric maps constructed in the previous sections, an extreme scenario was selected, defined by $a = 0.35\,\mathrm{m}$ and $b = -0.30\,\mathrm{m}$, located in one of the regions with the highest total energy and potentially most critical in terms of stability. The objective was to evaluate the system behavior under a more challenging configuration, prior to the implementation of control strategies.

Figure 26 – Time evolution of the Lyapunov exponents for the scenario with $a = 0.35\,\mathrm{m}$ and $b = -0.30\,\mathrm{m}$.

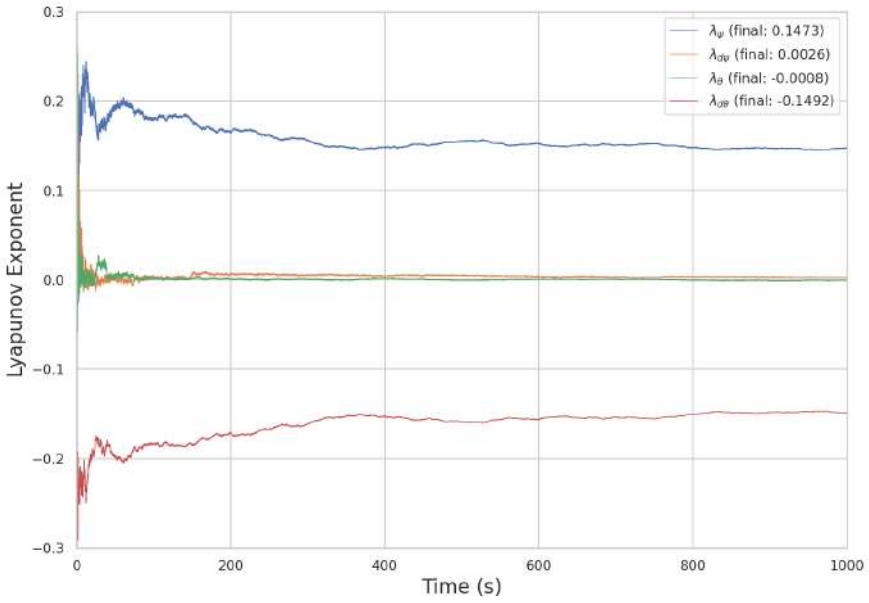

Source: The Author, 2025.

Figure **??** and Figure **??** compare the Lyapunov exponent evolution for a moderate parameter set and the extreme scenario $(a, b) = (0.35, -0.30)\,\mathrm{m}$. In both cases, each exponent converges rapidly to a steady value, with no sustained upward trend. The exponent λ_ψ increases slightly from ≈ 0.1120 to ≈ 0.1473 , indicating only a marginal rise in sensitivity of the pitch dynamics. Exponent $\lambda_{\dot{\psi}}$ remains near zero ($0.0002 \to 0.0026$), and λ_θ stays slightly negative ($-0.0001 \to -0.0008$). Finally, $\lambda_{\dot{\theta}}$ becomes more negative ($-0.1121 \to -0.1492$), reflecting increased damping in the pendulum mode.

These small shifts confirm that the system's qualitative regime—periodic or quasi-periodic with local instabilities—persists in the extreme case, without clear evidence of a transition to fully developed chaos.

Figure 27 – Poincaré map in the θ vs $d\theta$ plane for the scenario with $a = 0.35\,\mathrm{m}$ and $b = -0.30\,\mathrm{m}$. Magenta points represent $\dot{\psi} > 0$, and dark gray points represent $\dot{\psi} < 0$.

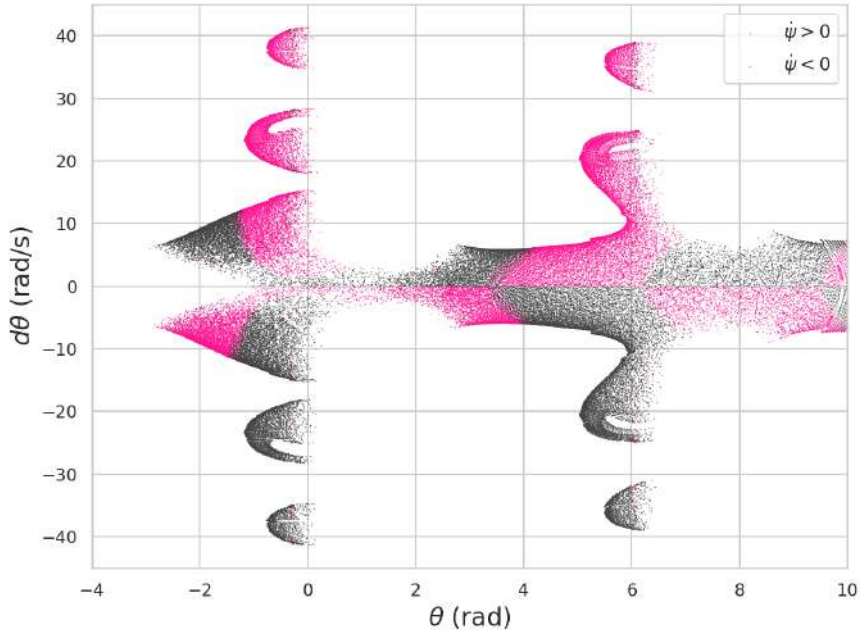

Source: The Author, 2025.

This difference becomes even more evident when analyzing the Poincaré maps. Figure **??** shows that the phase portrait for θ remains qualitatively similar to the one observed previously. On the other hand, Figure **??** reveals a significant change in the dynamic pattern of ψ, with greater dispersion and disorganization in the Poincaré sections, indicating loss of regularity and a possible transition to chaotic behavior.

To complement the analysis and allow for a broader visual assessment of the dynamics, full Poincaré maps are also included (Figures **??** and **??**). In these extended visualizations, the difference in behavior between the variables becomes even more evident. Particularly for ψ, one can observe a complete breakdown of previous patterns, characterizing highly sensitive and potentially chaotic behavior.

Figure 28 – Full Poincaré map in the θ vs $d\theta$ plane for the scenario with $a = 0.35\,\mathrm{m}$ and $b = -0.30\,\mathrm{m}$. Blue points indicate $\dot{\psi} > 0$, and dark gray points indicate $\dot{\psi} < 0$. The behavior of θ remains regular, with organized patterns similar to those seen in the previous simulation.

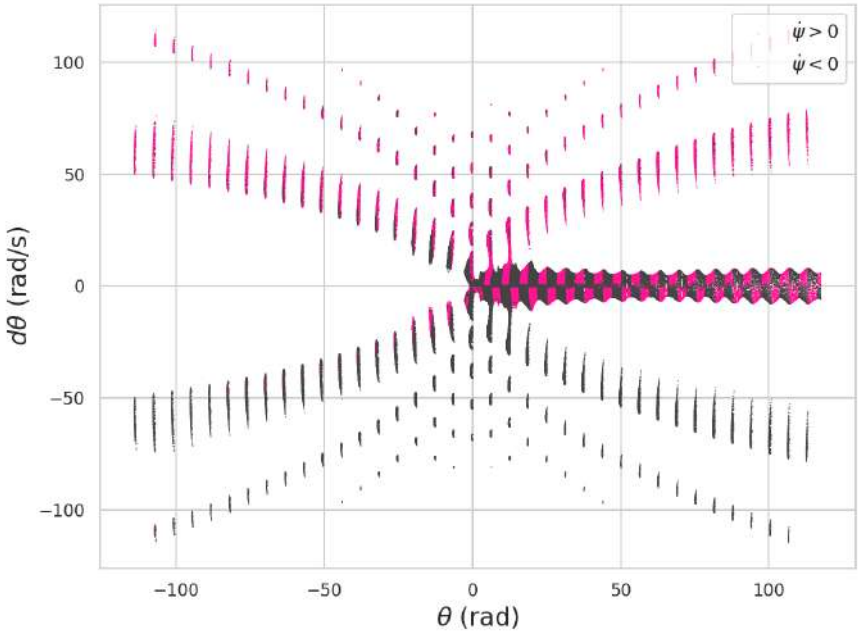

Source: The Author, 2024.

These results show that, under certain geometric parameter combinations, the system may exhibit severe dynamic degradation even without significant variations in all state variables. Therefore, the careful selection of a and b during system modeling is essential to ensure stability and performance. This scenario will later be used to assess the effectiveness of the designed controller.

Figure 29 – Poincaré map in the ψ vs $d\psi$ plane for the scenario with $a = 0.35\,\mathrm{m}$ and $b = -0.30\,\mathrm{m}$. Blue points represent $\dot{\psi} > 0$ and grey points represent $\dot{\psi} < 0$.

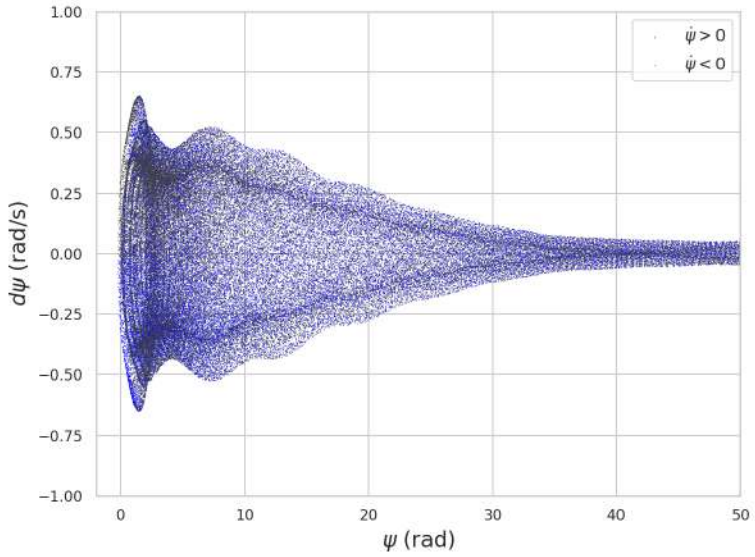

Source: The Author, 2025.

Figure 30 – Full Poincaré map in the ψ vs $d\psi$ plane for the scenario with $a = 0.35\,\mathrm{m}$ and $b = -0.30\,\mathrm{m}$. Blue points indicate $\dot{\psi} > 0$ and gray points indicate $\dot{\psi} < 0$.

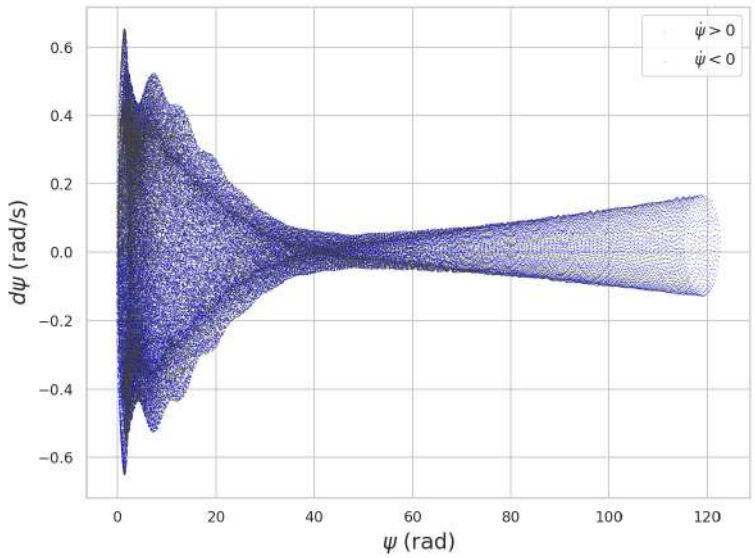

Source: The Author, 2024.

5 Nonlinear Control

The attitude control of spacecraft carrying internal liquid propellant presents significant challenges due to the dynamic couplings between the rigid body and the sloshing of the fuel. These couplings introduce nonlinearities, dynamic perturbations, and time-varying effects that can compromise pointing accuracy, excite unwanted oscillations, and jeopardize system stability if not properly addressed. Traditional linear control techniques, although widely employed, are often insufficient to handle such nonlinear behavior, particularly in scenarios with strong interactions between the spacecraft and the sloshing mass.

In this chapter, a nonlinear state-feedback control strategy based on the State-Dependent Riccati Equation (SDRE) methodology is proposed to mitigate the influence of sloshing on the satellite attitude dynamics. The SDRE approach allows the formulation of locally optimal controllers by solving a Riccati equation with state-dependent system matrices, enabling the preservation of the system nonlinearities while ensuring stabilizing control actions. The methodology is implemented and numerically evaluated considering extreme operating scenarios, demonstrating its effectiveness in stabilizing the coupled satellite-fluid system and attenuating the undesired sloshing-induced perturbations.

5.0.1 Notation Clarification

In this chapter, to avoid ambiguity between the different matrices used in the modeling and control formulation, the following notation is adopted throughout the text:

- $\mathbf{K_r}(\psi, \theta)$ denotes the *restorative stiffness matrix* of the mechanical model, representing the nonlinear restoring forces acting on the system as a function of the generalized coordinates.

- $\mathbf{K}(x)$ denotes the *state-feedback gain matrix* obtained from the SDRE approach, which is computed from the solution of the state-dependent Riccati equation.

This distinction ensures clarity between the physical parameters of the system dynamics and the control gains applied to the state vector.

5.1 Control Design Using SDRE Methodology

To stabilize the angular motion of the satellite affected by internal sloshing dynamics, we employ a nonlinear control strategy based on the State-Dependent Riccati Equation (SDRE) method. This approach allows the design of a state-feedback controller where the system matrix is explicitly dependent on the current state, enabling local linearizations at each integration step. This approach allows the transformation of the nonlinear control problem into a sequence of local Linear Quadratic Regulator (LQR) problems evaluated along the trajectory, preserving the system's nonlinear characteristics while ensuring computational feasibility for real-time applications. The method has been demonstrated as a robust and efficient alternative for such systems (**??????**).

The general form of the system must be rewritten as:

$$\dot{x} = A(x)x + B(x)u + G(x), \tag{5.1}$$

where $x \in \mathbb{R}^4$ is the state vector, $u \in \mathbb{R}$ is the control input (the torque M_ψ), $A(x) \in \mathbb{R}^{4\times4}$ and $B(x) \in \mathbb{R}^{4\times1}$ are state-dependent matrices, and $G(x)$ gathers all nonlinear terms that cannot be expressed as $A(x)x$ or $B(x)u$.

The state vector is defined as:

$$x = \begin{bmatrix} \psi & \theta & \dot{\psi} & \dot{\theta} \end{bmatrix}^T. \tag{5.2}$$

Only the torque M_ψ is considered a control input, while the sinusoidal torque $T_s(t)$ is treated as an external disturbance. The objective is to design a feedback law $u(x)$ that stabilizes the attitude of the satellite by minimizing a local quadratic cost function at each instant.

5.1.1 State-Dependent Representation

The nonlinear dynamics of the satellite-fluid system can be described by a second-order differential equation of the form:

$$M(\theta)\ddot{q} + C(\theta, \dot{\theta})\dot{q} + K_r(\psi, \theta)q = F(\psi, \theta, \dot{\psi}, t) + B_c u, \tag{5.3}$$

where $q = \begin{bmatrix} \psi & \theta \end{bmatrix}^T$ are the angular positions of the sloshing mass and the satellite body, respectively. The matrices M, C, and K_r represent the inertia, dissipative, and restorative components of the system, respectively, all of which are state-dependent. The vector F includes the gravitational and external forcing effects. The control input $u = M_\psi$ acts only on the first equation, i.e., the torque around ψ.

To apply the SDRE method, we define the state vector:

$$x = \begin{bmatrix} \psi & \theta & \dot{\psi} & \dot{\theta} \end{bmatrix}^T, \tag{5.4}$$

and rewrite the system in the first-order form:

$$\dot{x} = \begin{bmatrix} \dot{\psi} \\ \dot{\theta} \\ \ddot{\psi} \\ \ddot{\theta} \end{bmatrix} = A(x)x + B(x)u + G(x), \tag{5.5}$$

where:

- $A(x) \in \mathbb{R}^{4\times4}$ is the Jacobian matrix of the nonlinear vector field with respect to the state vector x.
- $B(x) \in \mathbb{R}^{4\times1}$ is the input matrix, derived as the effect of the control torque M_ψ applied to the satellite.
- $G(x, t) \in \mathbb{R}^4$ represents nonlinear and time-dependent forcing terms, including gravitational torques and external disturbances such as the sinusoidal excitation $T_s(t)$.

The expressions for $A(x)$, $B(x)$, and $G(x, t)$ are obtained from the equations of motion in matrix form:

$$\ddot{q} = M(\theta)^{-1}\left[-C(\theta, \dot{\theta})\dot{q} - K(\psi, \theta)q + F(\psi, \theta, \dot{\psi}, t)\right], \tag{5.6}$$

with $q = [\psi, \theta]^\top$ and $\dot{q} = [\dot{\psi}, \dot{\theta}]^\top$.

Thus, the complete state-space representation is:

$$\dot{x} = \begin{bmatrix} \dot{\psi} \\ \dot{\theta} \\ \ddot{\psi} \\ \ddot{\theta} \end{bmatrix} = A(x)x + B(x)u + G(x,t),$$

where:

- $A(x) = \frac{\partial f(x)}{\partial x}$ is computed symbolically,
- $B(x)$ is the first column of $M^{-1}(\theta)$ appended to zeros in $\dot{\psi}$ and $\dot{\theta}$ rows,
- $G(x,t) = f(x) - A(x)x$, representing all remaining nonlinearities not captured by the affine component.

5.1.2 SDRE-Based Optimal Control Design

Given the nonlinear state-dependent representation of the system, the SDRE control strategy is employed to compute an optimal feedback gain $K(x)$ based on the solution of a Riccati equation at each state point.

The control objective is to stabilize the satellite's attitude while mitigating the disturbances caused by fluid sloshing. To achieve this, we formulate a local quadratic cost function of the form:

$$J = \int_0^\infty \left[x(t)^\top Q x(t) + u(t)^\top R u(t) \right] dt, \tag{5.7}$$

where $Q \in \mathbb{R}^{4\times4}$ is a symmetric positive semi-definite matrix penalizing deviations in state variables, and $R \in \mathbb{R}^{1\times1}$ is a symmetric positive definite scalar penalizing control effort.

At each point x, the following algebraic Riccati equation is solved:

$$A(x)^\top P(x) + P(x)A(x) - P(x)B(x)R^{-1}B(x)^\top P(x) + Q = 0, \tag{5.8}$$

where $P(x) \in \mathbb{R}^{4\times4}$ is the unique positive-definite solution of the Riccati equation.

The optimal feedback law is given by:

$$u(x) = -K(x)x = -R^{-1}B(x)^{\top}P(x)x. \tag{5.9}$$

This approach effectively transforms the nonlinear control problem into a series of local Linear Quadratic Regulator (LQR) problems, enabling real-time computation of the control input through matrix updates that reflect the current system state. The method is particularly suitable for highly nonlinear systems, such as the one considered in this work, as it preserves the nonlinear structure while offering computational tractability.

It is important to emphasize that the feedback gain $K(x)$ obtained via the SDRE method is *locally optimal*. Specifically, for each operating point x, the Riccati equation

$$A(x)^{\top}P(x) + P(x)A(x) - P(x)B(x)R^{-1}B(x)^{\top}P(x) + Q = 0 \tag{5.10}$$

is solved assuming that the system behaves locally as a linear time-invariant (LTI) system with matrices $A(x)$ and $B(x)$. The resulting gain

$$K(x) = R^{-1}B(x)^{\top}P(x) \tag{5.11}$$

minimizes the instantaneous quadratic cost

$$J = \int_0^{\infty} \left[x^{\top}Qx + u^{\top}Ru\right] dt, \tag{5.12}$$

under the local approximation.

However, since the SDRE strategy does not globally solve the nonlinear optimal control problem, the controller does not guarantee global optimality in the sense of minimizing the cost functional over the full nonlinear trajectory. Nonetheless, SDRE preserves the nonlinear structure of the system and provides an effective feedback law that adapts to the system state, often yielding excellent practical performance even in strongly nonlinear regimes.

5.1.3 Numerical Evaluation in the Extreme Scenario

To illustrate the application of the SDRE controller under challenging conditions, we consider the set of parameters defined in Table **??**, which characterizes the

nonlinear satellite-fluid system under study. For this specific simulation, the values of parameters a and b were adjusted to $a = 0.35$ and $b = -0.30$, respectively, as established in the subsection discussing the extreme scenario, chosen after a parametric analysis of energy conservation.

The initial state used in the evaluation corresponds to the chaotic regime identified in the free response analysis:

$$x = \begin{bmatrix} \psi & \theta & \dot{\psi} & \dot{\theta} \end{bmatrix}^\top = \begin{bmatrix} 0.5236 & 0.0873 & 0.5 & 0.5 \end{bmatrix}^\top.$$

The matrices $A(x)$, $B(x)$, and the vector $G(x,t)$ were numerically evaluated at this state using the symbolic expressions derived in the previous section and the torque disturbance $T_s(t)$ at $t = 0$. The complete analytical expressions for the matrices $A(x)$, $B(x)$, and the vector $G(x,t)$ involves a large number of coupled dynamic terms and trigonometric interactions. Due to its length, it has been included in Appendix **??** for clarity and readability. This expression plays a key role in the formulation of the state-space model incorporating the effects of fluid sloshing and external torques in the pitch dynamics of the satellite system.The results obtained are:

$$A(x) = \begin{bmatrix} 0 & 0 & 1.0000 & 0 \\ 0 & 0 & 0 & 1.0000 \\ 0.8892 & 0.4156 & -0.0127 & -0.0105 \\ 4.5575 & -0.4303 & 0.0879 & 0.0086 \end{bmatrix}, \quad B(x) = \begin{bmatrix} 0 \\ 0 \\ 0.0010 \\ -0.0008 \end{bmatrix},$$

$$G(x,t) = \begin{bmatrix} 0 \\ 0 \\ 0.0687 \\ 0.3792 \end{bmatrix}.$$

The controllability of the pair $(A(x), B(x))$ was verified by checking the rank of the controllability matrix:

$$\operatorname{rank}\left(\mathcal{C} = \begin{bmatrix} B & AB & A^2B & A^3B \end{bmatrix}\right) = 4.$$

An initial evaluation of the SDRE control strategy was performed using the weighting matrices

$$Q = \mathrm{diag}(100,\ 10,\ 1,\ 1), \quad R = 1.$$

With this configuration, the continuous algebraic Riccati equation was solved at the initial condition, yielding the gain

$$K(x) = \begin{bmatrix} 4114.4 & 786.5 & 3115.3 & 580.5 \end{bmatrix},$$

which results in a control input of approximately

$$u(x) = -K(x)x \approx -4070.8\ \mathrm{N \cdot m}.$$

This very high control effort highlights the aggressive nature of the chosen weights and confirms that the SDRE controller can strongly counteract the sloshing-induced disturbances and nonlinear coupling in the extreme operating conditions.

To mitigate the excessive control effort while maintaining stabilization performance, the weighting matrices were redefined as

$$Q = \mathrm{diag}(200,\ 20,\ 5,\ 2), \quad R = 0.1.$$

This choice gives more relative weight to angular velocities—particularly $\dot{\theta}$—while penalizing the control input more lightly. With these weights, the SDRE law was evaluated along the full nonlinear state trajectory, yielding a time-varying gain matrix.

At the initial condition, the gain computed was:

$$K(x) = \begin{bmatrix} 106.7261 & -14.1242 & 37.0799 & -548.8528 \end{bmatrix},$$

which generated a control torque of

$$u(x) = K(x)x \approx 201.24\ \mathrm{N \cdot m}.$$

The application of the SDRE controller with the revised Q and R matrices led to a significant improvement in the dynamic behavior of the system under the extreme scenario. The temporal evolution of the satellite's pitch and internal sloshing dynamics is illustrated in Figures **??** and **??**, respectively.

Figure 31 – Time evolution of the pitch angle $\psi(t)$ with and without control.Greylines indicate the uncontrolled case and blue-colored segments correspond to the SDRE-controlled case.

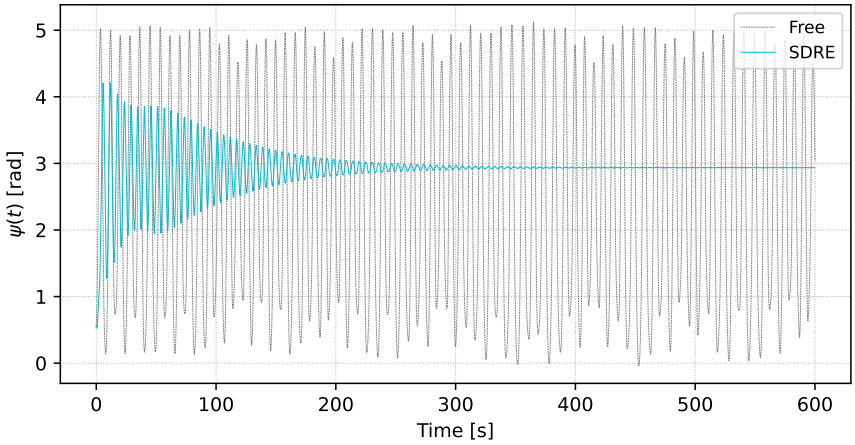

Source: The Author, 2025.

Figure 32 – Time evolution of the sloshing mass angle $\theta(t)$ with and without control.

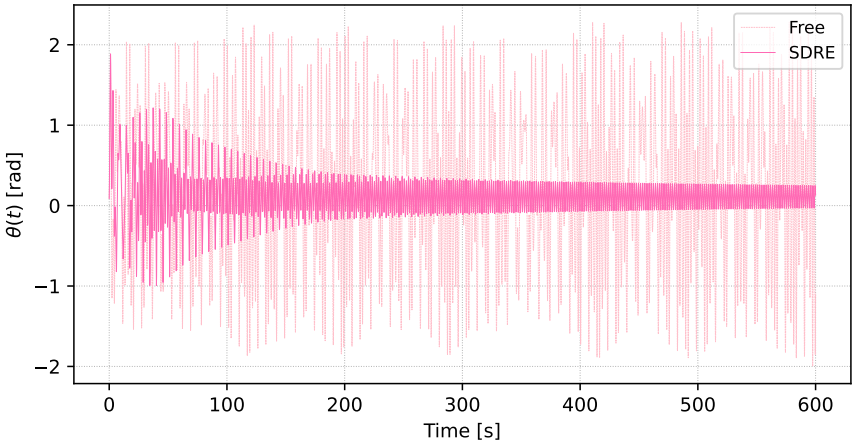

Source: The Author, 2025.

The comparison reveals that the SDRE controller successfully stabilizes both the satellite's pitch and the internal sloshing dynamics, represented by $\theta(t)$, within the first 100 seconds. The uncontrolled system exhibits persistent oscillations, while the controlled case converges rapidly to a neighborhood near the equilibrium.

A quantitative comparison between the two scenarios is summarized in Table **??**, which presents the estimated settling times and maximum overshoot values for both state variables. The uncontrolled dynamics of $\psi(t)$ and $\theta(t)$ fail to settle within the 600-second time window, indicating either sustained oscillatory behavior or the presence of low-frequency quasi-periodic modes. Conversely, under the SDRE controller, both variables exhibit fast attenuation of transients.

Specifically, the pitch angle $\psi(t)$ reaches steady-state conditions around 90 seconds after the control is engaged, with a substantial reduction in overshoot—from approximately 0.58 rad down to 0.18 rad. Similarly, the internal sloshing mode, represented by $\theta(t)$, is significantly damped, achieving stabilization in approximately 70 seconds and showing a peak deviation of only 0.09 rad.

These results highlight the effectiveness of the SDRE approach not only in improving the convergence rate but also in suppressing undesired oscillations and enhancing overall attitude stability of the system.

Table 4 – Comparison of performance indicators with and without SDRE control.

Variable	**Scenario**	**Settling Time (s)**	**Max Overshoot (rad)**
$\psi(t)$	Uncontrolled	> 600	0.58
	SDRE	$\sim$ 90	0.18
$\theta(t)$	Uncontrolled	> 600	0.33
	SDRE	$\sim$ 70	0.09

Source: The Author, 2025.

The phase portraits presented in Figures **??** and **??** further reinforce this behavior. Each plot shows the system response with and without SDRE control in the $(\psi,\ \dot{\psi})$ and $(\theta,\ \dot{\theta})$ planes. The trajectories corresponding to the uncontrolled system exhibit wide and persistent oscillations, indicative of nonlinear coupled dynamics and possibly quasi-periodic motion.

The blue and pink lines represent, respectively, the $(\psi,\ \dot{\psi})$ and $(\theta,\ \dot{\theta})$ trajectories. In both cases, the darker lines in each color represent the response of the controlled system. These appear as small, concentrated points near the center of the phase space, suggesting effective stabilization by the SDRE law.

Figure 33 – Phase portrait of satellite pitch $(\psi,\ \dot{\psi})$ trajectories with and without control. Greylines indicate the uncontrolled case and blue-colored segments correspond to the SDRE-controlled case.

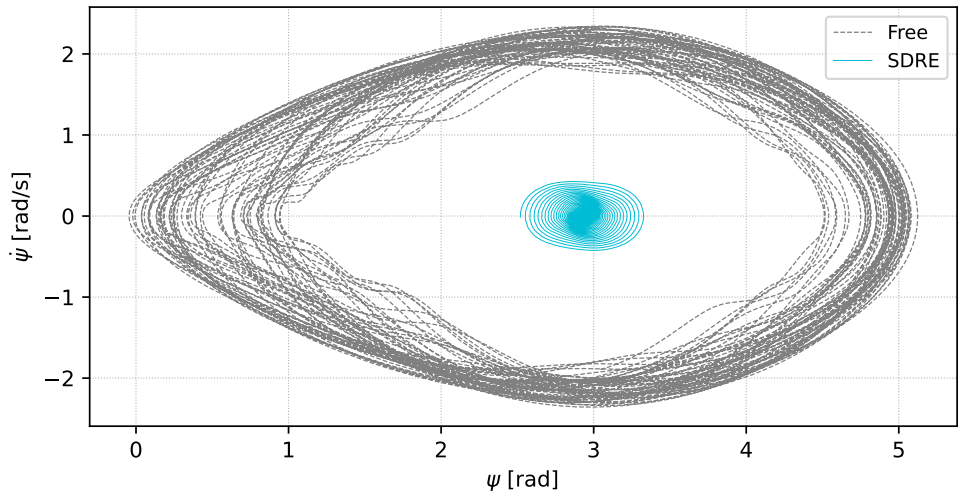

Source: The Author, 2025.

Figure 34 – Phase portrait of sloshing mass $(\theta,\ \dot{\theta})$ with and without control. Light ping indicate the uncontrolled case and dark pink-colored segments correspond to the SDRE-controlled case.

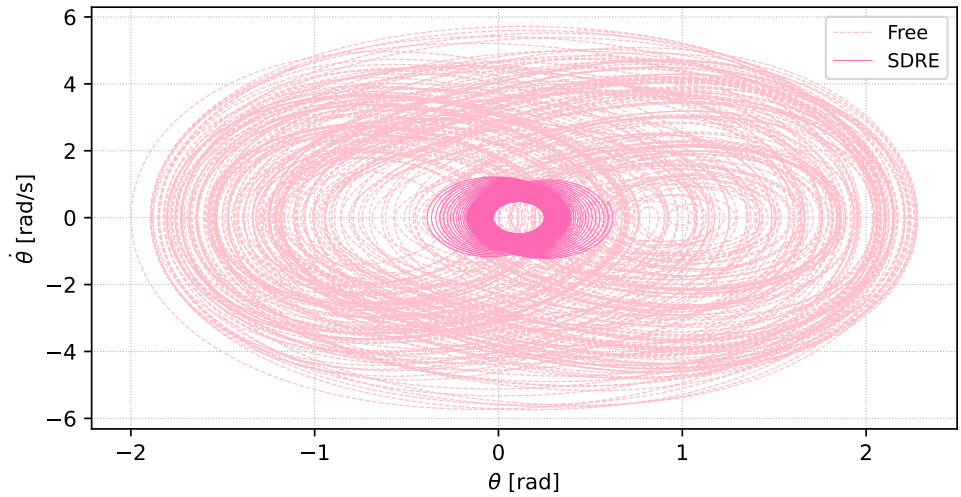

Source: The Author, 2025.

To better visualize the asymptotic behavior of the controlled system, Figure **??** and **??** shows a zoomed-in view of the state trajectories after removing the initial 40% transient. In this refined view, the convergence of the controlled dynamics toward the origin becomes more evident. The blue trace corresponds to the $(\psi,\ \dot{\psi})$ plane and the pink trace to $(\theta,\ \dot{\theta})$, clearly revealing the attenuation of the oscillatory behavior and the suppression of residual motion under SDRE control.

Figure 35 – Zoomed-in phase portrait of of satellite pitch $(\psi,\ \dot{\psi})$ with control after transient removal (20% of initial data excluded).

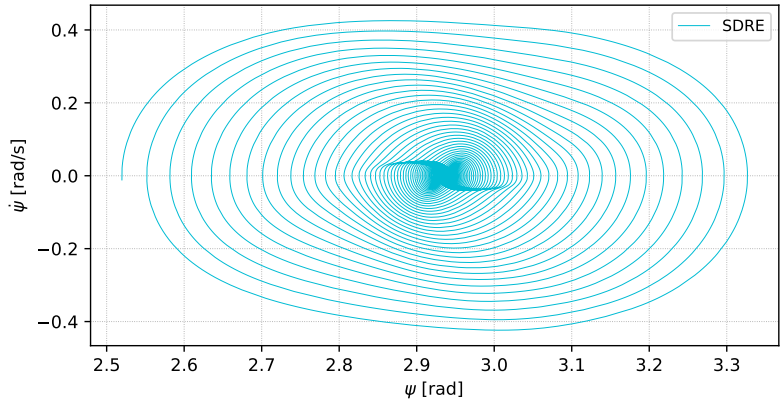

Source: The Author, 2025.

Figure 36 – Zoomed-in phase portrait of of sloshing mass $(\theta,\ \dot{\theta})$ with control after transient removal (20% of initial data excluded).

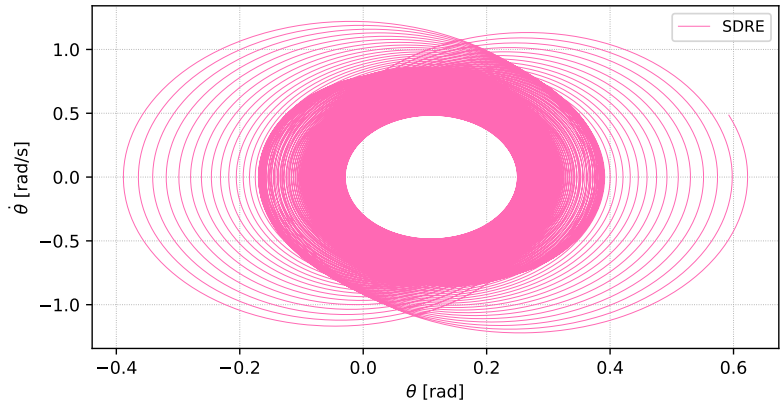

Source: The Author, 2025.

Finally, Figure **??** shows the control torque $u(t)$ applied by the SDRE law. As expected from the aggressive tuning and initial state deviation, the control effort reaches a peak of approximately -4000 N $\cdot$ m at the beginning of the simulation. This high initial action is required to rapidly suppress the strong nonlinear oscillations and steer the system toward equilibrium. After the transient, the torque decays swiftly and remains close to zero, confirming the effectiveness of the SDRE controller in minimizing steady-state energy expenditure while maintaining stability.

Figure 37 – Time evolution of the control torque $u(t)$ generated by the SDRE controller.

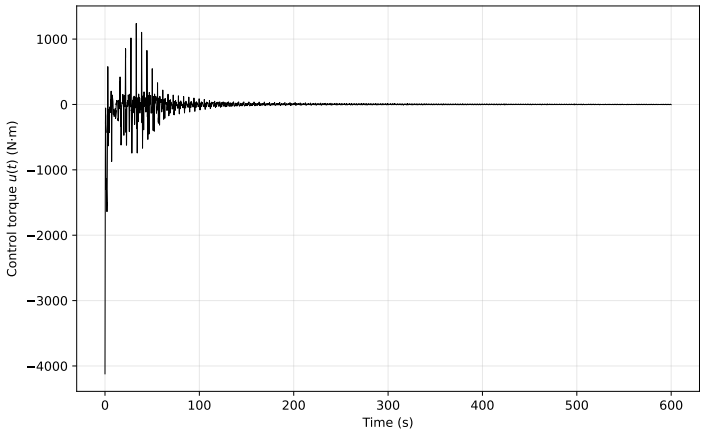

Source: The Author, 2025.

These results validate the SDRE approach as an effective method for nonlinear attitude control in spacecraft subjected to fluid sloshing effects, particularly under challenging dynamic conditions.

Although the SDRE controller achieves a good stabilization performance, it requires a relatively high torque in the initial moments of the simulation. As shown in Figure **??**, the control input $u(t)$ reaches values close to $+4000$ N $\cdot$ m before gradually declining. This behavior is a direct consequence of the aggressive weighting adopted in the matrix Q and the low penalization on the control input in $R = 0.1$.

Such high control efforts might be infeasible in practice due to actuator saturation limits or energy constraints aboard small spacecraft. Therefore, alternative strategies to mitigate this excessive control action include increasing the weight R to

reduce the control magnitude, at the expense of slower convergence.

The current SDRE formulation serves as a reference baseline for performance under ideal conditions. Future work may explore multi-objective optimization to balance control effort and transient suppression more effectively.

5.1.3.0.1 Remark: Augmenting the System with Integral Action.

While the SDRE controller provides effective stabilization, the current formulation relies solely on state feedback. To further improve steady-state accuracy and ensure disturbance rejection, the inclusion of an integrator is recommended. This can be achieved by augmenting the state vector with an additional integral state that accumulates the deviation between the actual state and the desired reference. The augmented system can then be controlled using an extended SDRE formulation, enhancing performance in the presence of persistent disturbances such as those induced by fluid sloshing or actuator imperfections.

5.1.4 SDRE Control with Time Delay Compensation

To further assess the robustness of the SDRE controller, we analyze its performance in the presence of a constant time delay in the control loop. Time delays are common in spacecraft applications due to onboard computation time, communication latency, or sensor-actuator dynamics. In this study, we introduce a delay $\tau = 0.1$ s in the feedback control path, meaning that the control input $u(t)$ is computed based on the state vector $x(t-\tau)$. The same SDRE formulation described earlier is employed, but the control law becomes:

$$u(t) = -K(x(t-\tau))x(t-\tau), \tag{5.13}$$

where $K(x)$ is evaluated as in the delay-free case. The simulation incorporates this delay using the `dde23` solver in MATLAB, which handles delay differential equations with a specified history function.

Figures **??** and **??** compare the time evolution of $\psi(t)$ and $\theta(t)$ under three scenarios: free (uncontrolled) dynamics, SDRE without delay, and SDRE with time

delay. Each plot illustrates the stabilizing effect of the SDRE controller and the degradation introduced by the delay.

Figure 38 – Time evolution of the pitch angle $\psi(t)$: free system (gray), SDRE control (light blue), and under SDRE control with delay ($\tau = 0.1$ s), after 10% transient removal (dark blue).

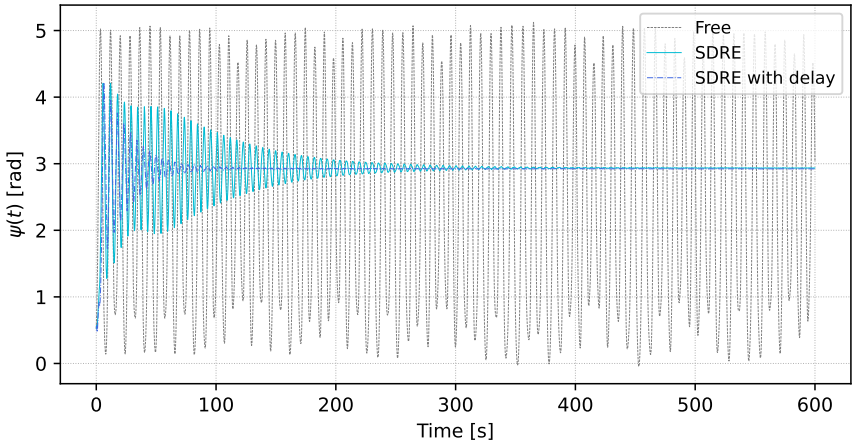

Source: The Author, 2025.

Figure 39 – Time evolution of the sloshing angle $\theta(t)$: free system (light pink), SDRE control (red), and under SDRE control with delay ($\tau = 0.1$ s), after 10% transient removal (magenta).

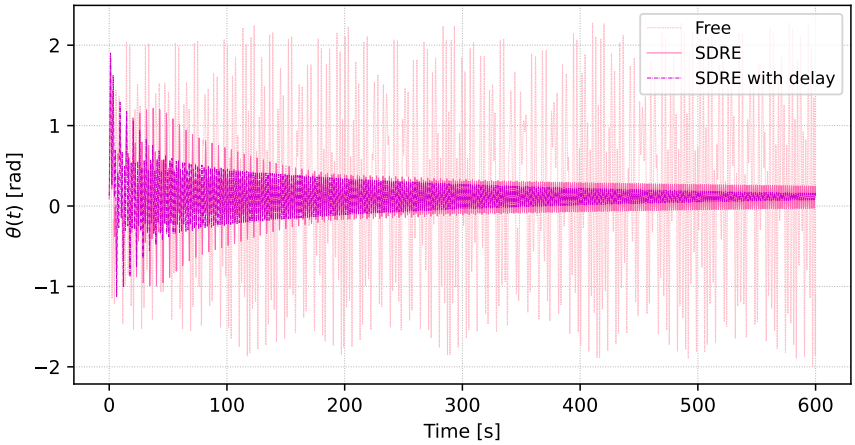

Source: The Author, 2025.

As expected, the presence of delay slightly worsens the transient performance. However, with a moderate delay of $\tau = 0.1$ s, the system remains stable and converges to the same equilibrium as in the delay-free case. The pitch angle $\psi(t)$ settles slightly slower, and the sloshing mode $\theta(t)$ exhibits a mild overshoot increase.

The phase portraits in Figures **??** and **??** provide further insight into the system dynamics with delay. Compared to the delay-free controlled system, the trajectories in the $(\psi,\ \dot{\psi})$ and $(\theta,\ \dot{\theta})$ planes show a larger transient excursion but eventually converge to the origin.

These results suggest that the SDRE control law maintains sufficient robustness against small constant delays, making it suitable for practical implementations in real-world satellite systems. Nonetheless, further investigation is needed to assess performance under time-varying or uncertain delays, and to compare it with alternative robust control strategies.

Figure 40 – Phase portraits of satellite pitch $(\psi,\ \dot{\psi})$: free system (gray), SDRE control (light blue), and under SDRE control with delay ($\tau = 0.1$ s), after 10% transient removal (dark blue).

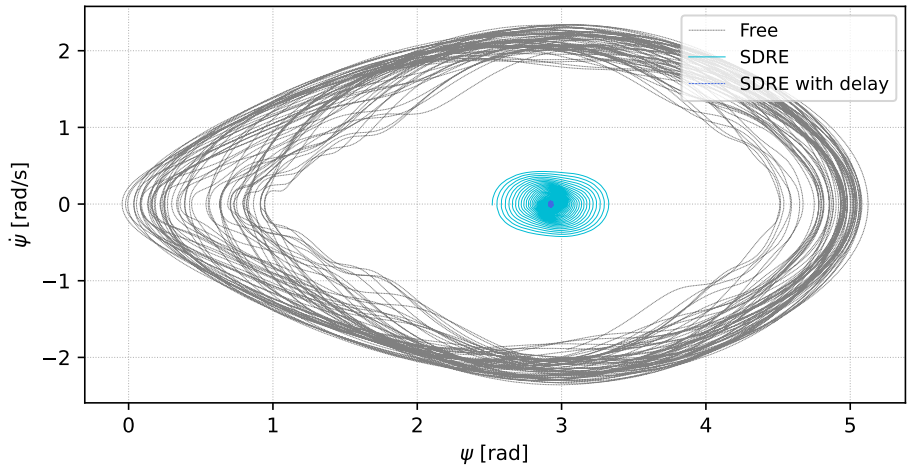

Source: The Author, 2025.

Figure 41 – Phase portraits of sloshing mass $(\theta,\ \dot{\theta})$: free system (light pink), SDRE control (dark pink), and under SDRE control with delay ($\tau = 0.1$ s), after 10% transient removal (magenta).

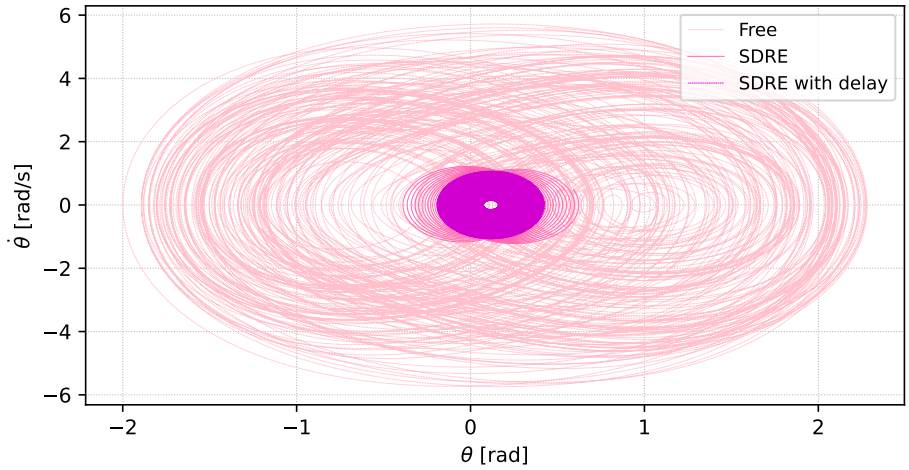

Source: The Author, 2025.

5.1.5 Comparison of Control Effort with and without Time Delay

Figure **??** compares the control torque $u(t)$ generated by the SDRE controller with and without the presence of delay. Interestingly, while both controllers exert high effort during the initial transient, the SDRE with delay exhibits a slightly lower peak torque magnitude and settles to low control levels more quickly.

Specifically, the delay-free SDRE (orange line) reaches a peak torque exceeding $+1000$ N · m, while the delayed case (blue line) remains below this value, with a slightly smaller undershoot. Moreover, the duration of intense oscillatory effort is reduced in the delayed response, indicating a potential benefit in energy efficiency or actuator load management, despite the inherent time lag.

These results suggest that a small constant delay, such as $\tau = 0.05$ s, not only maintains system stability but may also mitigate excessive control effort during early transients.

Figure 42 – Comparison of control torque $u(t)$: SDRE controller with and without time delay ($\tau = 0.05$ s).

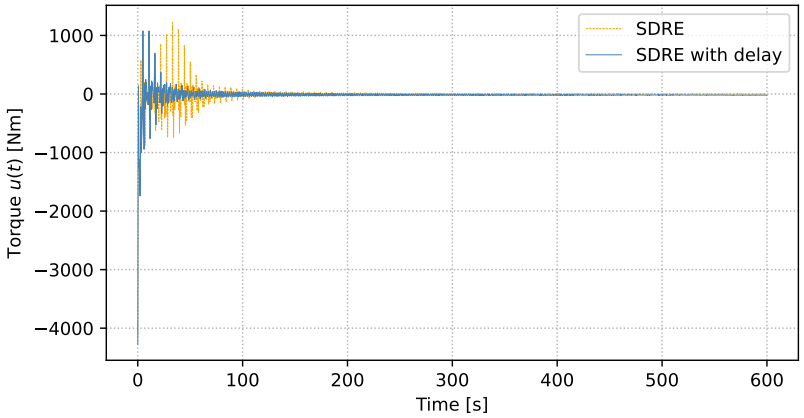

Source: The Author, 2025.

5.1.6 Comparison of Control Effort and Energy Consumption with and without Time Delay

In the context of attitude stabilization for spacecraft with internal fluid sloshing, it is common to assess control effort by analyzing the time history of the applied torque. However, this approach may offer only a partial view of the control strategy's effectiveness, particularly in strongly nonlinear systems where energy exchange mechanisms between the rigid body and the fluid are significant.

To advance toward a more comprehensive evaluation, we propose that control performance should not be assessed solely in terms of torque amplitude or instantaneous power—computed, for instance, as $P(t) = |u(t) \cdot \dot{\psi}(t)|$. Instead, it is crucial to consider the total mechanical energy of the system, including both kinetic and potential components of the satellite and the internal fluid.

Although preliminary simulations suggest that the SDRE controller with delay tends to apply less aggressive torque inputs and settles more rapidly to nominal actuation levels, the broader implications in terms of total system energy remain an open point for future investigation. Factors such as energy dissipation, coupling dynamics, and potential actuator saturation should be analyzed more thoroughly

before definitive conclusions are drawn.

Figure **??** illustrates the control torque $u(t)$ generated by the SDRE controller with and without time delay. While both configurations present high torque magnitudes during the transient regime, the delayed controller yields a lower peak response and a faster convergence to low-amplitude steady-state control inputs. This behavior may be interpreted as a form of natural smoothing introduced by the delay, acting as a low-pass filter that mitigates abrupt control actions.

Therefore, in this work, the comparison of control effort between the SDRE controller with and without delay is presented with caution. While the reduced torque magnitude observed in the delayed case indicates a potential advantage in terms of actuator workload and practical implementation, a full energy-based assessment is necessary to support claims of improved efficiency or performance robustness.

Future studies should incorporate a detailed evaluation of the total energy exchanged within the system, including internal damping, control work, and oscillatory modes, to provide a more accurate and physically grounded comparison of control strategies.

Figure 43 – Comparison of control torque $u(t)$: SDRE controller with and without time delay ($\tau = 0.05$ s).

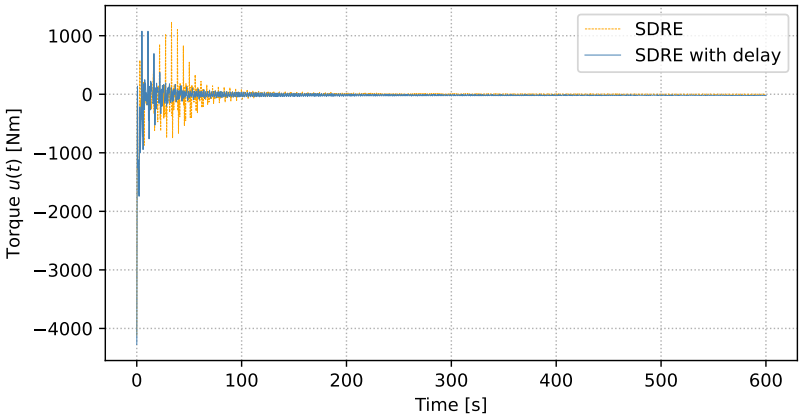

Source: The Author, 2025.

5.1.7 Sliding Mode Control Design

To provide a comparative evaluation of control techniques, a classical Sliding Mode Control (SMC) law was implemented. The control objective remains consistent with the SDRE strategy, aiming at the stabilization of the satellite's pitch dynamics under the influence of internal fluid sloshing disturbances, while rejecting perturbations and ensuring robustness to modeling uncertainties.

The SMC approach adopted in this study is grounded in the classical first-order sliding mode formulation, with a linear sliding surface defined as:

$$s(t) = \dot{\psi}(t) + \lambda\psi(t), \tag{5.14}$$

where $\lambda > 0$ is a positive design parameter that defines the convergence rate to the sliding manifold.

The discontinuous control law is synthesized as:

$$u(t) = -k\,\mathrm{sign}(s(t)), \tag{5.15}$$

in which $k > 0$ is the switching gain, selected to satisfy the sliding condition $s(t)\dot{s}(t) < 0$, thereby ensuring finite-time convergence of the system trajectories to the sliding surface $s(t) = 0$.

Once the system reaches sliding motion, the dynamics reduce to:

$$\dot{\psi}(t) + \lambda\psi(t) = 0, \tag{5.16}$$

which leads to an exponential stabilization of the $\psi(t)$ coordinate.

The parameters utilized in this investigation were empirically adjusted as $\lambda = 1.5$ and $k = 2000$, balancing convergence speed and chattering mitigation.

The present implementation does not incorporate dynamic compensation terms, boundary layer techniques, or smoothing strategies commonly employed to mitigate chattering phenomena. This simplification was deliberate, aiming to enable a direct comparison with the SDRE-based regulator under analogous conditions.

The proposed SMC formulation is consistent with the approaches reported by **??**) and **??**), where sliding mode control has been successfully applied for

spacecraft attitude stabilization in the presence of fuel sloshing effects. Specifically, **??**) employed a fuzzy sliding mode controller augmented with gain scheduling and optimization techniques (PSO) for a coupled spacecraft-fuel model, demonstrating the effectiveness of SMC strategies in suppressing sloshing-induced disturbances. Although the present work does not include fuzzy tuning or gain scheduling, the SMC formulation herein follows the same fundamental principles of robustness to uncertainties and invariance to matched disturbances.

Similarly, **??**) proposed a nonlinear sliding surface tailored for slosh-free motion, highlighting the efficacy of sliding mode approaches in systems with underactuated degrees of freedom and unmatched uncertainties. While their work focuses on slosh suppression in terrestrial containers, the control law structure and robustness properties remain analogous to those employed in this chapter, reaffirming the suitability of SMC for handling the sloshing dynamics in spacecraft applications.

5.1.8 Comparison of Control Strategies

Figures **??** and **??** summarize the time evolution of the pitch angle $\psi(t)$ and the sloshing angle $\theta(t)$ under all evaluated control scenarios: uncontrolled dynamics, SDRE control, SDRE with time delay, and Sliding Mode Control (SMC). The SMC strategy, shown in red for $\psi(t)$ and in royal blue for $\theta(t)$, demonstrates robust stabilization with rapid suppression of transient oscillations. The system reaches equilibrium faster than the delayed SDRE controller and with slightly less overshoot than the delay-free case, particularly for the internal sloshing mode.

The control effort associated with each strategy is presented in Figure **??**. The SMC input (purple curve) exhibits significantly lower amplitude compared to the peak torque observed in the SDRE-based approaches. While the SDRE controller reaches an initial torque of nearly -4000 N $\cdot$ m, the SMC signal remains bounded between approximately -150 and $+150$ N $\cdot$ m, with a notable reduction in overall control energy.

However, the SMC torque profile is highly oscillatory, which is a known characteristic of ideal sliding mode implementations. This chattering behavior is expected in the absence of a boundary layer or smooth approximation of the discontinuous

sign function. Additionally, the current formulation does not include a dynamic compensation term to account for model uncertainties or matched perturbations.

Despite these simplifications, the SMC controller is widely adopted in the literature for spacecraft attitude regulation with sloshing effects due to its structural simplicity and inherent robustness. In this study, the SMC design was intentionally kept minimal to serve as a benchmark against the more complex SDRE strategies. Further refinements, such as the use of saturation functions, higher-order sliding modes, or adaptive gains, can be introduced to mitigate chattering and improve performance.

These results suggest that the SMC approach offers an attractive alternative when control energy and implementation simplicity are prioritized, although it may require additional tuning or filtering mechanisms for practical deployment.

Figure 44 – Time evolution of the pitch angle $\psi(t)$ for all control scenarios. Gray: Free dynamics; Cyan: SDRE; Blue: SDRE with delay; Red: Sliding Mode.

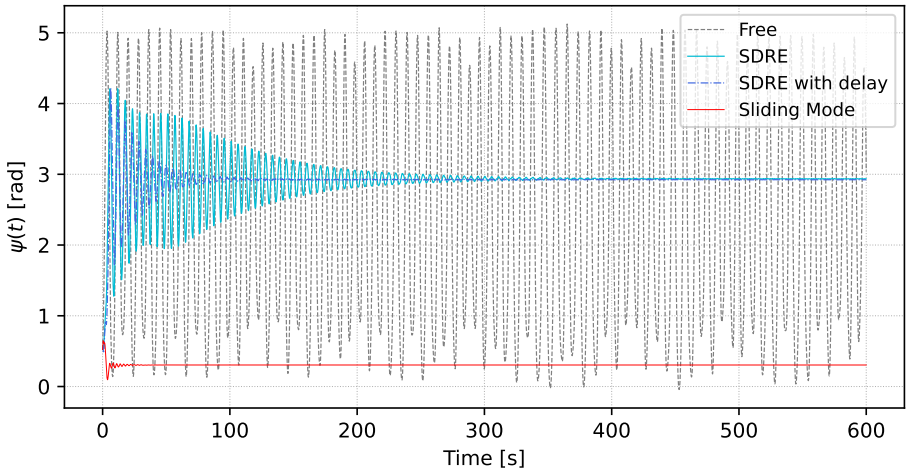

Source: The Author, 2025.

Figure 45 – Time evolution of the sloshing angle $\theta(t)$ for all control scenarios. Pink: Free dynamics; Hotpink: SDRE; Magenta: SDRE with delay; Black: Sliding Mode.

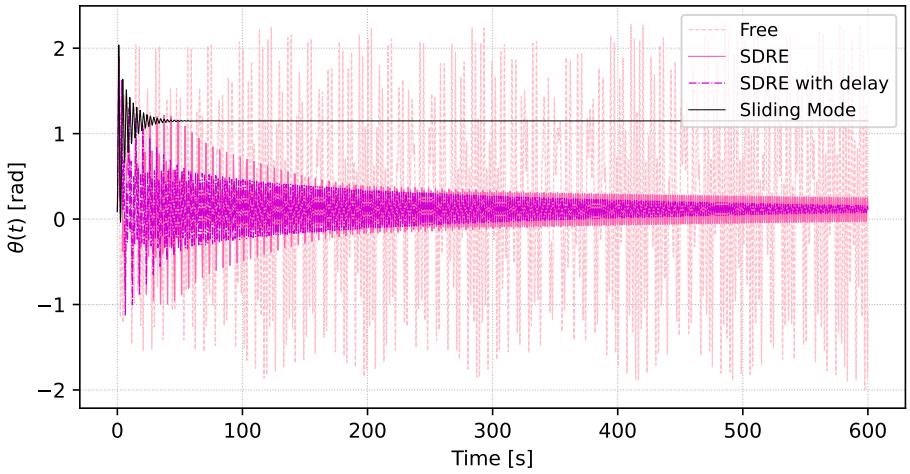

Source: The Author, 2025.

Figure 46 – Control effort $u(t)$ for each strategy. Orange: SDRE; Blue: SDRE with delay; Purple: Sliding Mode.

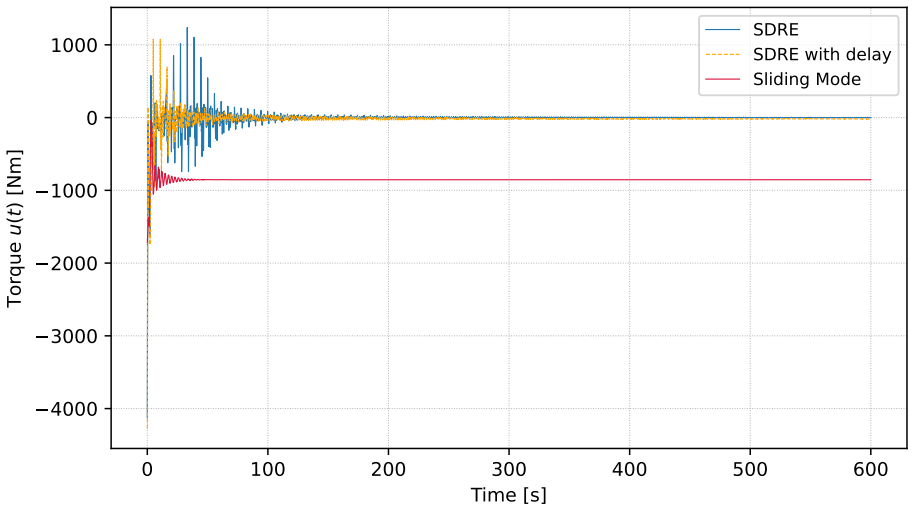

Source: The Author, 2025.

5.1.9 Sliding Mode Control with PID Enhancement (SMC-PID)

To improve the robustness and reduce the steady-state error observed with the conventional Sliding Mode Control (SMC), a composite control law combining SMC with a Proportional-Integral-Derivative (PID) structure was implemented. This approach aims to leverage the fast convergence characteristics of SMC while mitigating the chattering effect and enhancing tracking accuracy, especially in the presence of uncertainties and unmodeled dynamics (**??**).

The sliding surface is defined as a PID-like expression:

$$s(t) = K_p\, e(t) + K_i \int_0^t e(\tau) d\tau + K_d\, \dot{e}(t), \tag{5.17}$$

where $e(t) = \psi(t)$ is the attitude tracking error, K_p, K_i, and K_d are the proportional, integral, and derivative gains, respectively.

The control law is given by:

$$u(t) = u_{\mathrm{PID}} + u_{\mathrm{SMC}}, \tag{5.18}$$

with:

$$u_{\mathrm{PID}} = K_p\, e(t) + K_i \int_0^t e(\tau) d\tau + K_d\, \dot{e}(t), \tag{5.19}$$

$$u_{\mathrm{SMC}} = -k_{\mathrm{SMC}}\, \mathrm{sat}\left(\frac{s(t)}{\eta}\right), \tag{5.20}$$

where k_{SMC} is the sliding gain and η is the boundary layer thickness used to smooth the control action and alleviate chattering.

In this work, the parameters were tuned based on preliminary trials to balance control effort and dynamic performance, adopting the following values:

$$K_p = 500, \quad K_i = 0.1, \quad K_d = 100, \quad k_{\mathrm{SMC}} = 1000, \quad \eta = 0.05.$$

The SMC-PID control action was applied exclusively to the satellite pitch channel ψ, considering the system as underactuated with no direct control on the fluid sloshing angle θ. The resulting control torque $u(t)$ is computed at each integration step and directly injected into the dynamic model.

This strategy aims to provide robust stabilization of the satellite attitude despite the strong nonlinear coupling with the sloshing dynamics, while keeping the control effort within feasible levels.

Figure 47 – SMC-PID control effort over 600 seconds of simulation.

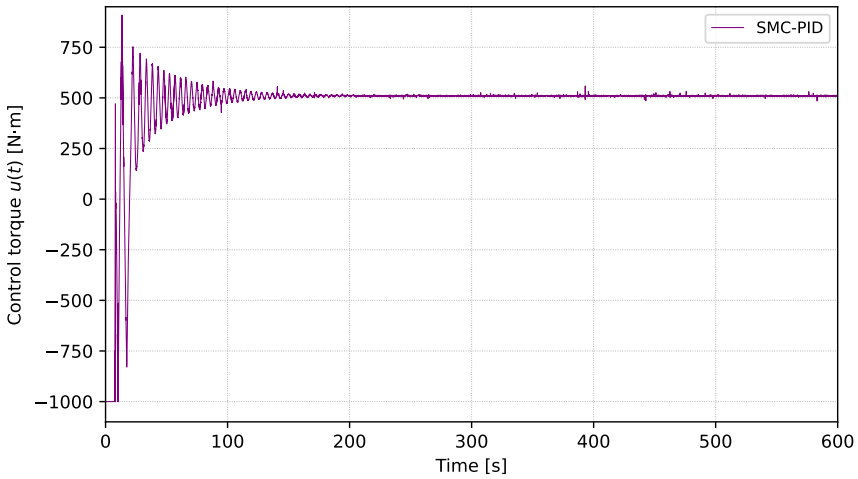

Source: The Author, 2025.

Figure 48 – SMC-PID control effort during the transient period (0–100 s).

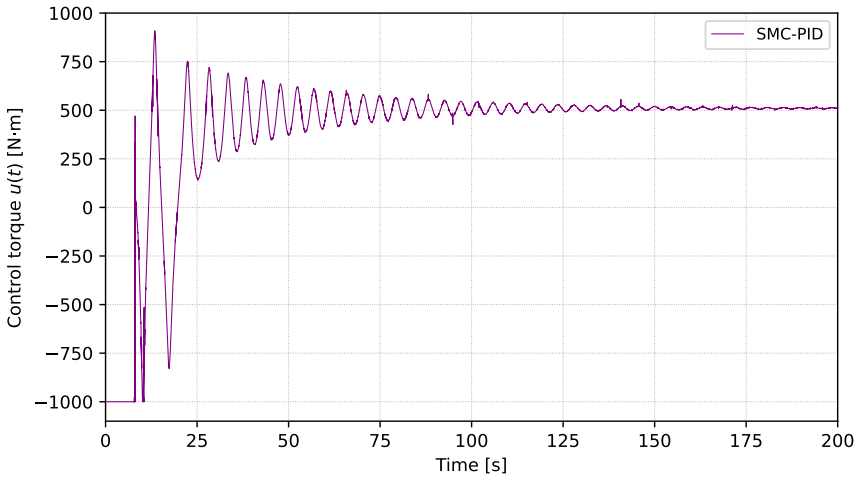

Source: The Author, 2025.

Figure 49 – Comparison of control torque during transients for all controllers.

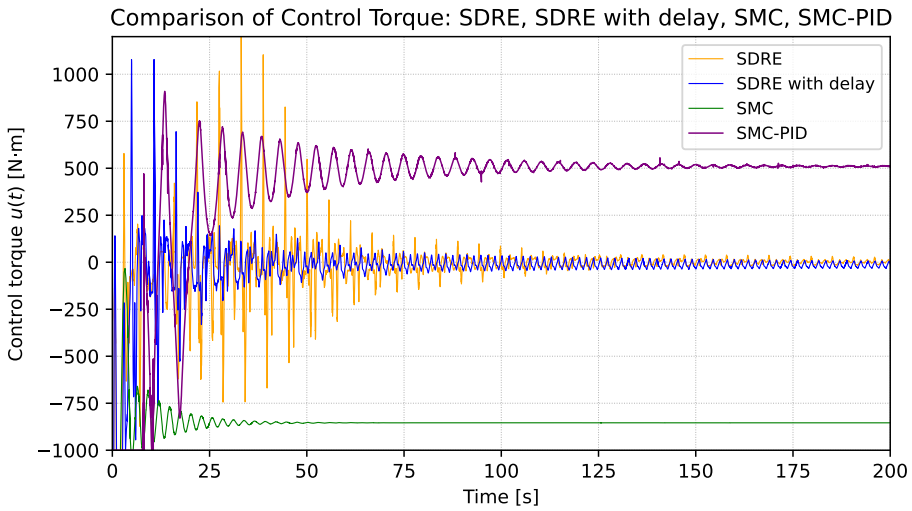

Source: The Author, 2025.

Figure 50 – Time evolution of state variables under SMC-PID control.

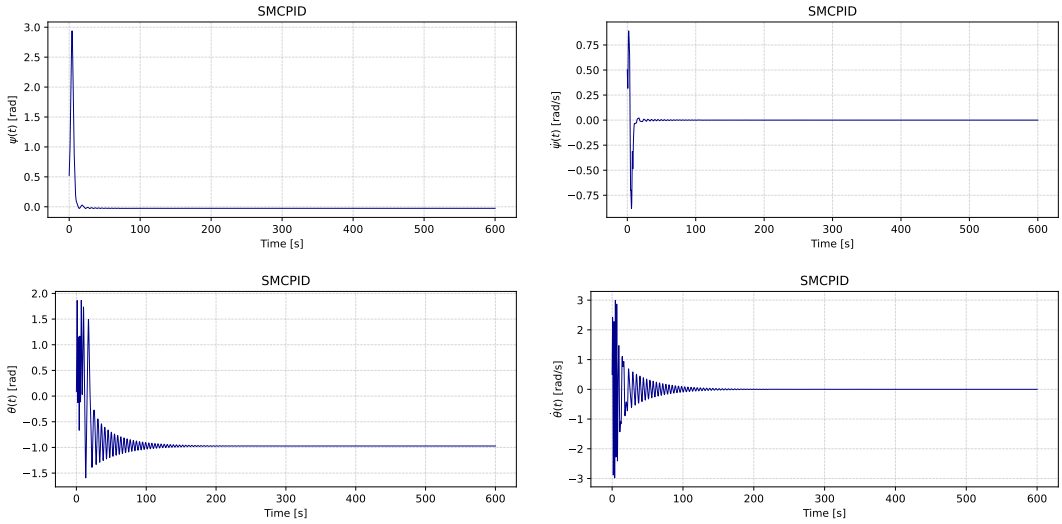

Source: The Author, 2025.

The comparative results summarized in Table **??** reveal the distinct characteristics of each control approach. The SDRE controller, in its ideal configuration,

achieves the fastest stabilization of both the pitch angle $\psi(t)$ and the sloshing mode $\theta(t)$, albeit with the highest control effort, reaching torque peaks of approximately 4000 N·m. The inclusion of a 0.1 s delay in the feedback loop slightly compromises the settling time but leads to a noticeable reduction in control effort, confirming the robustness of the SDRE strategy even under moderate delays.

Table 5 – Quantitative performance comparison of all evaluated controllers.

Controller	**Settling $\psi(t)$ (s)**	**Settling $\theta(t)$ (s)**	**Torque Peak (N·m)**	**Steady-State Torque (N·m)**
SDRE	$\sim$ 90	$\sim$ 70	$\sim$ 4000	$\sim \pm$5
SDRE with delay	$\sim$ 100	$\sim$ 85	$\sim$ 3000	$\sim$ -20
Sliding Mode	$\sim$ 120	$\sim$ 100	$\sim$ 1500	$\sim$ -850
SMC-PID	$\sim$ 80	$\sim$ 65	$\sim$ 600	$\sim$ 500

Source: The Author, 2025.

Sliding Mode Control (SMC), while still effective in stabilizing the system, results in slower convergence compared to SDRE and exhibits a pronounced chattering phenomenon. Nevertheless, the control effort is substantially lower, with torque peaks reduced to about 1500 N·m, illustrating the intrinsic robustness and energy efficiency of SMC even in its basic form.

Remarkably, the proposed SMC-PID hybrid controller outperforms all other approaches in the balance between control performance and effort. It achieves faster stabilization of both $\psi(t)$ and $\theta(t)$ compared to the classical SDRE, while keeping the control torque significantly lower, peaking at around 600 N·m. This result demonstrates that the addition of the PID term to the sliding mode structure effectively improves transient performance and suppresses chattering effects, without sacrificing the inherent robustness of the sliding mode technique.

These findings highlight that the SMC-PID approach is a promising solution for satellite attitude control under sloshing disturbances, particularly in scenarios where actuator saturation and energy constraints are critical concerns.

6 Conclusion

This work presented the nonlinear modeling and dynamic analysis of a satellite containing internal fluid, with the sloshing phenomenon represented by an equivalent pendulum and the presence of disturbance torques from unbalanced reaction wheels. The mathematical model was developed using Lagrangian mechanics, allowing the derivation of a coupled system of nonlinear differential equations that describe the interaction between the satellite's rigid body motion and the internal fluid dynamics. The model incorporated restoring and dissipative forces, as well as external torques, thus reflecting the complexity of the satellite-fluid system operating in orbit.

The results demonstrated the strong influence of the sloshing effect on the satellite's attitude stability. Through time-domain and spectral analysis, it was observed that while the satellite's pitch angle ψ exhibited predominantly periodic or quasi-periodic oscillations, the fluid motion, represented by the variable θ, revealed more complex behavior, with waveform modulations and energy transfer between modes.

The Lyapunov exponent analysis confirmed the presence of local instabilities and sensitivity to initial conditions, particularly in the variable ψ, which reached positive Lyapunov values even under relatively smooth oscillatory regimes. This behavior suggests the existence of strange nonchaotic attractors or transient chaos in the coupled system.

Poincaré maps provided a deeper understanding of the global structure of the system dynamics. The maps confirmed quasi-periodic behavior in nominal conditions, but also revealed signs of drift and trajectory diffusion, especially for the satellite variable ψ, indicating a loss of confinement and the onset of long-term instability.

In the parametric energy analysis, it was verified that geometric parameters such as the pendulum length (a) and pivot position (b) play a critical role in the system's energy distribution. Longer pendulums and off-centered pivot positions were shown to increase kinetic and total system energy, thus intensifying the nonlinear

effects and dynamic complexity. These results reinforce the importance of careful parameter estimation during the modeling phase.

An extreme scenario was investigated, illustrating that small changes in the parameters can significantly affect the system's behavior. In this configuration, the satellite exhibited a clear degradation of dynamic performance, with increased Lyapunov exponents and disrupted Poincaré structures—emphasizing the need for robust control strategies to ensure mission safety.

Three control strategies were evaluated based on this model: the optimal State-Dependent Riccati Equation (SDRE) control, the SDRE with time-delay in the feedback loop, and Sliding Mode Control (SMC). The numerical results indicated that SDRE provides excellent dynamic performance and rapid stabilization, at the cost of high torque peaks during the transient regime; The introduction of a constant delay of 0.1 s in the SDRE control loop slightly compromises the response time but still ensures stability and satisfactory performance; Sliding Mode Control proved effective in stabilization with significantly reduced control effort, although with pronounced oscillatory behavior (chattering) due to the lack of smoothing in the control law.

These results highlight the advantages and limitations of each approach. SDRE is more suitable when dynamic performance is a priority and actuators have a wide operational range. On the other hand, SMC, even in its simplified form, represents a robust and more energy-efficient alternative, being particularly attractive for systems with energy constraints or limited actuators.

6.1 Future Work

Future developments of this research are expected to address several key aspects to enhance the robustness, practicality, and applicability of the proposed control framework. One line of investigation involves the incorporation of more realistic actuator models, including saturation effects and time-varying delays, which are commonly encountered in space systems. In parallel, improvements to the sliding mode control strategy will be pursued through the introduction of smoothing mechanisms—such as boundary layer techniques or higher-order sliding modes—to mitigate chattering and achieve smoother control actions.

Another important direction lies in the global stability analysis of the controlled system. This analysis will be conducted using Lyapunov-based methods, complemented by geometric tools such as Poincaré sections and the numerical estimation of Lyapunov exponents, in order to gain deeper insight into the nonlinear dynamics and the effectiveness of the proposed control schemes.

Practical validation will also be prioritized through the development of test-benches and embedded simulations designed to emulate realistic operating conditions. These efforts aim to bridge the gap between theoretical modeling and real-world implementation, particularly in the context of space systems subject to strict mass, power, and volume constraints.

Building upon the present work, the adaptation of the developed models and control techniques to nanosatellite platforms is also envisioned. Given their compact structure and high sensitivity to internal and external disturbances, these systems demand highly efficient and computationally lightweight control solutions—especially for regulating motion around the pitch axis, which plays a critical role in orbital maneuvers.

To meet these requirements, future studies will focus on embedded implementations of advanced control strategies, such as the State-Dependent Riccati Equation (SDRE) method and sliding mode control, while taking into account the limitations imposed by onboard computational architectures, energy availability, and physical constraints.

Further developments may also include the establishment of technical collaborations with national space research institutions, aiming to validate the proposed methodologies under realistic conditions, including laboratory experiments and hardware-in-the-loop simulations. These initiatives would enhance the practical relevance and national integration of the research, supporting its application to small-spacecraft missions involving internal fluid dynamics.

In addition, future work encompasses the pedagogical application of simplified satellite control models within undergraduate courses in Electrical and Automation Engineering. The goal is to foster student engagement through the use of low-cost educational satellite simulators with reaction wheels, developed under open-source

and open-hardware paradigms. Designed by international teaching and research institutions, these platforms offer accessible experimental setups that facilitate hands-on demonstrations of control principles. Such educational integration promotes the dissemination of advanced aerospace concepts at the undergraduate level and reinforces the connection between academic research and engineering education.

Thus, this work provides a consistent theoretical and numerical foundation for the analysis and design of control strategies applicable to satellite systems affected by internal fluid motion. The results contribute to the understanding of nonlinear coupled dynamics and establish a solid basis for future studies on robust control applications in space systems with similar configurations.

Bibliography

ABRAMSON, H. N. *The Dynamic Behavior of Liquids in Moving Containers: With Applications to Space Vehicle Technology*. Washington, D.C.: NASA, 1966. NASA SP-106. Citado 3 vezes nas páginas 24, 28, and 31.

AHMAD, S.; YUE, B. Z. Bifurcation and stability analysis of the hamiltonian - casimir model of liquid sloshing. *Chinese Physics Letters*, IOP Publishing Ltd, v. 29, 2012. ISSN 17413540. Citado na página 37.

BALTHAZAR, J. M. et al. *Sistemas Dinâmicos e Mecatrônicos - Vol. 1: Teoria e Aplicação de Controle*. 1. ed. São Paulo, Brasil: Blucher, 2021. v. 1. (Sistemas Dinâmicos e Mecatrônicos, v. 1). Citado 2 vezes nas páginas 66 and 67.

BANDYOPADHYAY, B.; KURODE, S.; GANDHI, P. S. Sliding mode control for slosh-free motion-A class of underactuated system. v. 1, n. 3, 2009. Citado na página 39.

BAYARD, D. S. High-precision three-axis pointing and control. In: ____. *Encyclopedia of Aerospace Engineering*. [S.l.]: Wiley, 2010. Citado 7 vezes nas páginas 37, 42, 49, 50, 52, 55, and 56.

BENSON, D. J.; NG, W. Validation of Slosh Modeling Approach Using STAR-CCM +. In: NATIONAL AERONAUTICS AND SPACE ADMINISTRATION (NASA). Maryland, 2018. p. 1–12. Disponível em: <https://ntrs.nasa.gov/archive/nasa/casi.ntrs.nasa.gov/20180003007.pdf>. Citado na página 32.

CHEON, D. I. et al. Disturbance reduction on the small satellite actuator. In: *Proceedings of 2011 2nd International Conference on Instrumentation Control and Automation, ICA 2011*. [S.l.: s.n.], 2011. p. 31–34. ISBN 9781457714603. Citado 2 vezes nas páginas 37 and 52.

CHRISTIDI-LOUMPASEFSKI, O. O. et al. On system identification of space manipulator systems including their fuel sloshing effects. *IEEE Robotics and Automation Letters*, Institute of Electrical and Electronics Engineers Inc., v. 8, p. 2446–2453, 5 2023. ISSN 23773766. Citado na página 36.

ÇIMEN, T. State-Dependent Riccati Equation (SDRE) control: A survey. *IFAC Proceedings Volumes (IFAC-PapersOnline)*, v. 17, n. 1 PART 1, p. 3761–3775, 2008. ISSN 14746670. Disponível em: <http://linkinghub.elsevier.com/retrieve/pii/S1474667016395349>. Citado na página 81.

DENG, M.; YUE, B. Nonlinear model and attitude dynamics of flexible spacecraft with large amplitude slosh. *Acta Astronautica*, Elsevier Ltd, v. 133, p. 111–120, 4 2017. ISSN 00945765. Citado na página 35.

FURUICHI, Y. et al. Evaluation of Sloshing Effect on a Tank during Landing Phases of Spacecrafts in a Micro-Gravity Environment. In: *ASCEND 2022*. Las Vegas, Nevada & Online: American Institute of Aeronautics and Astronautics, 2022. ISBN 978-1-62410-662-0. Disponível em: <https://arc.aiaa.org/doi/10.2514/6.2022-4312>. Citado na página 31.

GASBARRI, P.; SABATINI, M.; PISCULLI, A. Dynamic modelling and stability parametric analysis of a flexible spacecraft with fuel slosh. *Acta Astronautica*, Elsevier Ltd, v. 127, p. 141–159, 2016. ISSN 00945765. Citado 2 vezes nas páginas 34 and 35.

GRAHAM, E. W.; RODRIGUEZ, A. M. The characteristics of fuel motion which affect airplane dynamics. *Journal of Applied Mechanics*, v. 19, n. 3, p. 381–388, 1952. ISSN 1098-6596. Citado na página 31.

HUBERT, C. *Behavior of Spinning Space Vehicles with Onboard Liquids, 2"d Edition, . Technical Report 88030*. Hanover, 2008. 83 p. Citado na página 31.

HUO, J. hai et al. Adaptive prediction backstepping attitude control for liquid-filled micro-satellite with flexible appendages. *Acta Astronautica*, Elsevier Ltd, v. 152, p. 557–566, 11 2018. ISSN 00945765. Citado na página 38.

IBRAHIM, R. A. *Liquid Sloshing Dynamics*. Cambridge: Cambridge University Press, 2005. ISBN 9780511536656. Disponível em: <https://www.cambridge.org/core/product/identifier/9780511536656/type/book>. Citado 5 vezes nas páginas 24, 26, 28, 29, and 30.

KURODE, S. et al. Sliding mode control for slosh-free motion using a nonlinear sliding surface. *IEEE/ASME Transactions on Mechatronics*, IEEE, v. 18, n. 2, p. 714–724, 2009. Citado 3 vezes nas páginas 39, 98, and 99.

LI, D.; CHEN, X.; WU, B. Analysis of reaction-wheels imbalance torque effects on satellite attitude control system. In: *2016 Chinese Control and Decision Conference (CCDC)*. IEEE, 2016. p. 3722–3725. ISBN 978-1-4673-9714-8. Disponível em: <http://ieeexplore.ieee.org/document/7531631/>. Citado 2 vezes nas páginas 37 and 52.

LI, Q.; MA, X.; WANG, T. Equivalent mechanical model for liquid sloshing during draining. *Acta Astronautica*, Elsevier, v. 68, n. 1-2, p. 91–100, 2011. ISSN 00945765.

Disponível em: <http://dx.doi.org/10.1016/j.actaastro.2010.06.052>. Citado 2 vezes nas páginas 55 and 56.

LIU, K.-C.; MAGHAMI, P.; BLAUROCK, C. Reaction wheel disturbance modeling, jitter analysis, and validation tests for solar dynamics observatory. In: *AIAA Guidance, Navigation and Control Conference and Exhibit*. American Institute of Aeronautics and Astronautics, 2008. ISBN 978-1-60086-999-0. Disponível em: <https://arc.aiaa.org/doi/10.2514/6.2008-7232>. Citado 2 vezes nas páginas 55 and 56.

MASON, P. A. C.; STARIN, S. R. Propellant Slosh Analysis for the Solar Dynamics Observatory. In: *595 Flight Mechanics Symposium*. Greenbelt, MD: NASA Goddard Space Flight Center; Greenbelt, MD, United States, 2005. p. 14. Citado na página 32.

MAZMANYAN, L.; AYOUBI, M. A. Fuzzy attitude control of spacecraft with fuel sloshing via linear matrix inequalities. *IEEE Transactions on Aerospace and Electronic Systems*, Institute of Electrical and Electronics Engineers Inc., v. 54, p. 2526–2536, 10 2018. ISSN 15579603. Citado na página 38.

NAVABI, M.; DAVOODI, A.; REYHANOGLU, M. Modeling and control of a nonlinear coupled spacecraft-fuel system. *Acta Astronautica*, Elsevier Ltd, v. 162, p. 436–446, 9 2019. ISSN 00945765. Citado 6 vezes nas páginas 23, 35, 38, 39, 55, and 56.

NAVABI, M.; DAVOODI, A.; REYHANOGLU, M. Optimum fuzzy sliding mode control of fuel sloshing in a spacecraft using pso algorithm. *Acta Astronautica*, Elsevier Ltd, v. 167, p. 331–342, 2 2020. ISSN 00945765. Citado 3 vezes nas páginas 39, 98, and 99.

NICHKAWDE, C.; HARISH, P. M.; ANANTHKRISHNAN, N. Stability analysis of a multibody system model for coupled slosh-vehicle dynamics. *Journal of Sound and Vibration*, v. 275, n. 3-5, p. 1069–1083, 2004. ISSN 0022460X. Citado 2 vezes nas páginas 55 and 56.

OTTANDER, J. A.; HALL, R. A.; POWERS, J. F. Practical methodology for the inclusion of nonlinear slosh damping in the stability analysis of liquid-propelled space vehicles. In: *2018 AIAA Guidance, Navigation, and Control Conference*. American Institute of Aeronautics and Astronautics, 2018. ISBN 978-1-62410-526-5. Disponível em: <https://arc.aiaa.org/doi/10.2514/6.2018-2097>. Citado 2 vezes nas páginas 55 and 56.

PIRAT, C. et al. H and µ-synthesis for nanosatellites rendezvous and docking. *IEEE Transactions on Control Systems Technology*, Institute of Electrical and Electronics Engineers Inc., v. 28, p. 1050–1057, 5 2020. ISSN 15580865. Citado na página 38.

PRIGOGINE, I.; STENGERS, I. *As Leis do Caos*. São Paulo: Unesp, 1997. Tradução de Gilson C. Packer. Citado na página 67.

RAFIKOV, M.; BALTHAZAR, J. M. Optimal linear and nonlinear control design for chaotic systems. In: *ASME 2005 International Design Engineering Technical Conferences and Computers and Information in Engineering Conference*. [S.l.: s.n.], 2005. v. 6, n. 11, p. 867–873. Citado na página 81.

REYHANOGLU, M. Modeling and Control of Space Vehicles with Fuel Slosh Dynamics. In: Jason Hall (Ed.). *Advances in Spacecraft Technologies*. InTech, 2014. cap. 24, p. 449–562. ISBN 978-953-307-551-8. Disponível em: <http://www.intechopen.com/books/advances-in-spacecraft-technologies/modelling-and-control-of-space-vehicles-with-fuel-slosh-dynamics>. Citado 4 vezes nas páginas 23, 28, 32, and 42.

REYHANOGLU, M.; RUBIO, J. R. Nonlinear control of a spacecraft with multiple fuel slosh modes. *Proceedings of the IEEE Conference on Decision and Control*, n. December, p. 6192–6197, 2011. ISSN 01912216. Citado 2 vezes nas páginas 55 and 56.

ROBERTS, R.; CHEN, P.-y. *Slosh design handbook i*. Washington, DC: [s.n.], 1966. 328 p. Citado na página 31.

RODRIGUES, V. d. S.; FENILI, A. ATTITUDE CONTROL OF SATELLITE WITH PROPELLANT SLOSHING DYNAM- ICS. In: *XL Ibero-Latin-American Congress on Computational Methods in Engineering, ABMEC*. Natal: [s.n.], 2019. Citado na página 42.

ROMERO, A. G.; SOUZA, L. C. G. de. Satellite controller system based on reaction wheels using the state-dependent riccati equation (sdre) on java. In: *Proceedings of the 10th International Conference on Rotor Dynamics – IFToMM*. [S.l.]: Springer, Cham, 2018. p. 547–561. Citado na página 39.

SHTESSEL, Y. et al. *Sliding Mode Control and Observation*. [S.l.]: Springer, 2014. Citado na página 102.

SHUAI, J.-W. et al. Positive lyapunov exponents calculated from time series of strange nonchaotic attractors. *Phys. Rev. E*, American Physical Society, v. 64, p. 026220, Jul 2001. Disponível em: <https://link.aps.org/doi/10.1103/PhysRevE.64.026220>. Citado na página 66.

SIDI, M. J. Structural Dynamics and Liquid Sloshing. In: *Spacecraft Dynamics and Control*. Cambridge: Cambridge University Press, 1997. cap. 10, p. 291–317. ISBN 9780511815652. Disponível em: <https://www.cambridge.org/core/product/identifier/

CBO9780511815652A092/type/book_part>. Citado 3 vezes nas páginas 23, 24, and 28.

SLABINSKI, V. J. INTELSAT IV IN-ORBIT LIQUID SLOSH TESTS AND PROBLEMS IN THE THEORETICAL ANALYSIS OF THE DATA Victor. In: *Attitude Control of Space Vehicles: Technological and Dynamical Problems Associated with the Presence of Liquids*. Toulouse: ESA, 1977. Disponível em: <https://ntrs.nasa.gov/archive/nasa/casi.ntrs.nasa.gov/19790017920.pdf>. Citado na página 31.

SOUZA, A. G. de. *Estudo do uso de métodos de controle robusto em sistemas espaciais rígidos-flexíveis*. Tese (Tese de Doutorado) — Instituto Nacional de Pesquisas Espaciais (INPE), São José dos Campos, Brasil, 2017. Programa de Pós-Graduação em Mecânica Espacial e Controle. Citado 2 vezes nas páginas 32 and 42.

SOUZA, L. C. G. de; SOUZA, A. G. de. Satellite attitude control system design considering the fuel slosh dynamics. *Shock and Vibration*, v. 2014, p. 1–8, 2014. Citado na página 40.

STARIN, S. R.; ETERNO, J. Attitude determination and control systems. In: *Spacecraft Dynamics*. [S.l.]: NASA, 2011. Chapter discussing advanced spacecraft attitude control systems. Citado na página 25.

STOREY, J. M. *Experimental, Numerical, and Analytical Slosh Dynamics of Water and Liquid Nitrogen in a Spherical Tank*. 133 p. Tese (Doutorado) — Florida Institute of Technology, 2016. Disponível em: <https://ntrs.nasa.gov/archive/nasa/casi.ntrs.nasa.gov/20160006562.pdf>. Citado na página 32.

TKACHEV, S. et al. Effect of reaction wheel imbalances on attitude and stabilization accuracy. 2021. Disponível em: <https://doi.org/10.3390/aerospace8090252>. Citado 2 vezes nas páginas 42 and 52.

TUSSET, A. M. et al. Statements on chaos control designs, including a fractional order dynamical system, applied to a 'mems' comb-drive actuator. *Nonlinear Dynamics*, 2012. Citado na página 81.

VELDMAN, A. et al. The numerical simulation of liquid sloshing on board spacecraft. *Journal of Computational Physics*, v. 224, n. 1, p. 82–99, may 2007. ISSN 00219991. Disponível em: <https://linkinghub.elsevier.com/retrieve/pii/S0021999106006139>. Citado na página 32.

VREEBURG, J. P. B. Spacecraft Maneuvers and Slosh Control. *IEEE Control Systems Magazine*, n. June, p. 0–4, 2005. Citado na página 31.

WIE, B. *Space Vehicle Dynamics and Control, Second Edition*. Reston ,VA: American Institute of Aeronautics and Astronautics, 2008. ISBN 978-1-56347-953-3. Disponível em: <http://arc.aiaa.org/doi/book/10.2514/4.860119>. Citado 3 vezes nas páginas 26, 28, and 32.

YANG, H. Q.; WEST, J. Validity of Miles Equation in Predicting Propellant Slosh Damping in Baffled Tanks at Variable Slosh Amplitude. In: *AIAA SciTech*. Kissimmee, FL: National Aeronautics and Space Administration (NASA), 2018. p. 1–13. Disponível em: <https://ntrs.nasa.gov/search.jsp?N=0{&}Ntk=Document-ID{&}Ntx=modematchall{&}Ntt=20>. Citado na página 32.

Appendix

APPENDIX A – Bibliometric Analysis of the Literature

This appendix presents the bibliometric process and the methodology applied to select the most relevant literature for this research. The objective is to identify and justify the selection of ten key papers that offer significant theoretical and empirical contributions to the study of nonlinear dynamics, attitude control, and fuel sloshing effects in spacecraft. The bibliometric analysis was carried out using the CAPES Portal of Journals, with search queries targeting publications on “sloshing”, “attitude dynamics”, and “reaction wheel imbalance”.

Figure 51 – Stages of the bibliometric selection process.

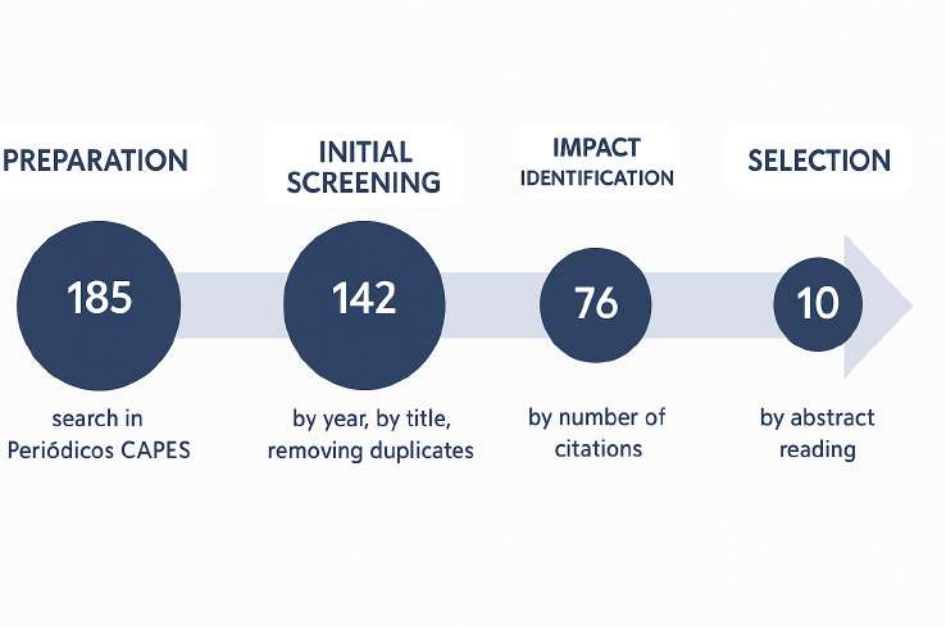

Source: The Author, 2025

Figure **??** summarizes the stages involved in the bibliometric selection process, highlighting the key steps from the initial data retrieval to the final dataset used for detailed analysis.

A.0.1 Search Strategy and Keywords

The search was conducted using the CAPES Journal Portal and complemented with metadata extraction from RIS and BibTeX files exported from selected databases. To capture a comprehensive range of relevant literature, the keyword combinations listed on Table **??** were used.

Table 6 – Keyword groups and codes used in the bibliometric analysis

Code	Keywords
I	"Spacecraft dynamics" OR "Fuel Slosh"
II	"Satellite dynamics" AND "Fuel Sloshing"
III	("spacecraft dynamics" OR "satellite dynamics") AND ("fuel slosh" OR "fuel sloshing")
IV	("nonlinear control" OR control) AND (spacecraft OR satellite) AND ("fuel slosh" OR "fuel sloshing")
V	"reaction wheels" AND ("fuel slosh" OR "fuel sloshing")

Source: The Author, 2025.

Figure 52 – Distribution of result papers by keyword

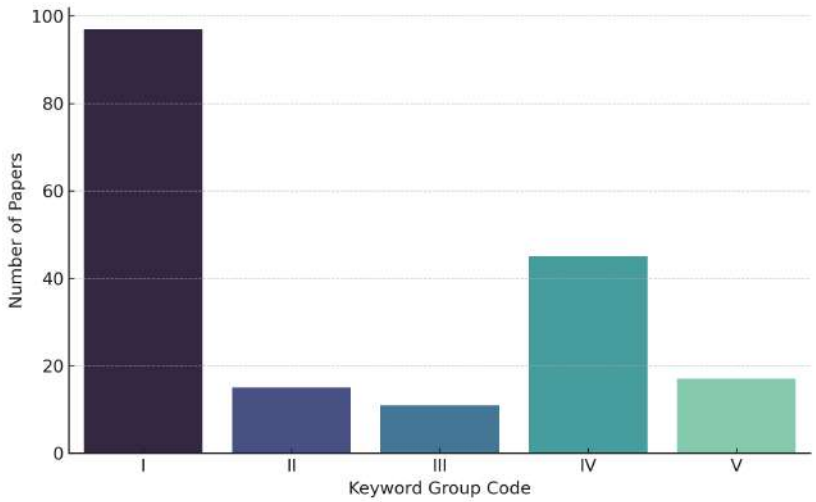

Source: The Author, 2025

The Boolean operators `AND`, `OR` were applied to expand the search scope and combine relevant technical terms. This yielded an initial dataset of over 180

publications distributed within this four keywors combination (Fig. **??**). Figure **??** illustrates the temporal evolution of scientific output related to satellite dynamics with sloshing effects. Based on the selection criteria adopted in this study, a growing interest in the topic can be observed over the past decade. The years 2018, 2019, and 2022 stand out with more than 30 papers each, suggesting a recent resurgence in research efforts focused on this domain.

Figure 53 – Distribution of result papers by publication year

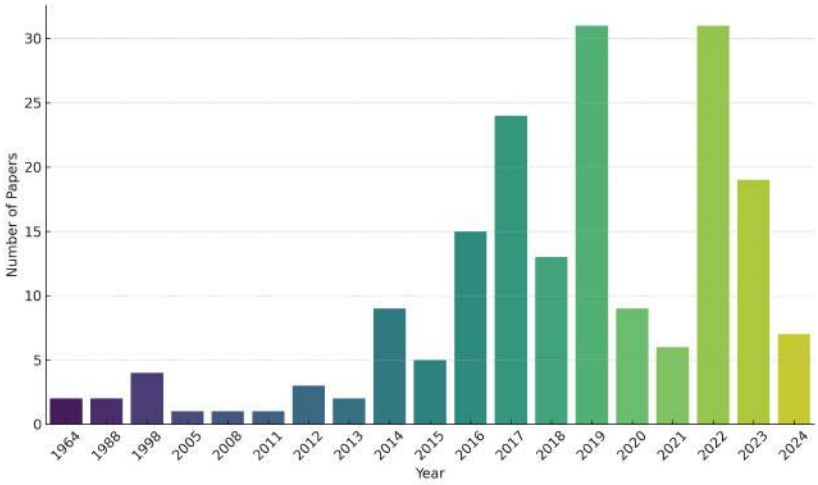

Source: The Author, 2025

A.0.2 Data Cleaning and Preprocessing

The metadata from all retrieved papers were compiled into a unified spreadsheet. The following cleaning steps were applied:

1. Elimination of duplicates: Papers with identical DOIs or titles were removed.
2. Normalization of journal and author names to standardize citations.
3. Verification of thematic adherence: Titles and abstracts were reviewed to confirm relevance to spacecraft dynamics, sloshing effects, or control strategies.
4. Manual corrections were applied where automated parsing tools failed to extract metadata correctly.

The journal Acta Astronautica stands out as both the most prolific and the most cited in the selected dataset. It published 6 of the top 20 most cited papers, accumulating a total of 210 citations, reflecting its central role in disseminating research on spacecraft dynamics and fuel sloshing, as shown in Table **??**. Applied Thermal Engineering follows with 05 citations from only 3 papers, highlighting its high impact per publication. Other journals contributed a single article each but gained recognition through relatively high individual citation counts.

Table 7 – Most productive and impactful journals in the selected dataset

Journal	**# Papers**	**Total Citations**
Acta Astronautica	6	210
Applied Thermal Engineering	3	105
Annals of Nuclear Energy	1	51
Journal of Guidance Control and Dynamics	1	25
Journal of Energy Storage	1	24
Aerospace Science and Technology	1	21
IEEE Trans. on Aerospace and Electronic Systems	1	20
Journal of Mechanics	1	20
AIAA Journal	1	17
IEEE Trans. on Control Systems Technology	1	15
Journal of Marine Science and Technology	1	14
Journal of Spacecraft and Rockets	1	14
Archive of Mechanical Engineering	1	13

Source: Author.

A.0.3 Selection Criteria

The refined dataset was then filtered using the following criteria:

- Time filter: Only papers published within the last 10 years were considered (2014–2024).

- Minimum citation threshold: Preference was given to works with at least 5 citations (with exceptions for recent high-impact works).
- Journal impact: Priority was given to publications in high-impact journals such as *Acta Astronautica*, *AIAA Journal*, and *IEEE Transactions*.
- Thematic coverage: Focused on nonlinear dynamics, fuel sloshing modeling, control strategies (e.g., sliding mode, backstepping, LMI), and practical spacecraft or satellite applications.

Table **??** presents the final list of the ten most relevant papers according to the criteria above. This filtered selection is intended to guide the modeling and control development strategy presented in the subsequent chapters, serving as a consolidated theoretical foundation for nonlinear dynamics in fuel slosh scenarios.

Table 8 – Top 10 selected papers relevant to spacecraft dynamics and fuel sloshing control

Code	Title	Authors	Year	Journal	Citations
II	Dynamic modelling and stability parametric analysis of a flexible spacecraft with fuel slosh	Gasbarri et al.	2016	Acta Astronautica	56
I	Nonlinear model and attitude dynamics of flexible spacecraft with large amplitude slosh	Deng & Yue	2017	Acta Astronautica	38
II	Adaptive prediction backstepping attitude control	Huo et al.	2018	Acta Astronautica	34
I	Optimum fuzzy sliding mode control	Navabi et al.	2019	Acta Astronautica	33
I	Attitude dynamics and control	Liu et al.	2017	Acta Astronautica	27
I	Modeling and control of a nonlinear coupled spacecraft-fuel system	Navabi et al.	2019	Acta Astronautica	22
IV	Fuzzy Attitude Control via LMI	Mazmanyan & Ayoubi	2018	IEEE TAES	20
IV	Modeling and Coupling Dynamics with Multiple Propellant Tanks	Baozeng et al.	2016	AIAA Journal	17
III	$\mathcal{H}_\infty$ and μ-Synthesis for Nanosatellites	Pirat et al.	2019	IEEE TCST	15
II	On System Identification Including Fuel Sloshing Effects	Christidi-Loumpasefski et al.	2023	IEEE RA-L	8

Source: The Author, 2025

APPENDIX B – Mathematical Modeling Code

This appendix presents the code used to implement the equations of motion derived in Chapter **??**. The modeling was carried out using the Julia programming language, based on the Lagrangian formulation and employing an equivalent pendulum model to represent the sloshing effects.

```
# Import required libraries
using DifferentialEquations, DynamicalSystems, ChaosTools
using LinearAlgebra, StaticArrays, Statistics, FFTW
using Plots, CairoMakie, ProgressMeter
using CSV, DataFrames
using Base.Threads
using Symbolics
using SymbolicUtils

# Define variable t and differential operator
@variables t
D = Differential(t)

# Define physical parameters
@variables a b c d g k epsilon real=true  # k = fluid
   stiffness coefficient
@variables m_p m_f real=true              # Masses
@variables I_sat real=true                # Satellite's
   moment of inertia
@variables M_psi real=true                # Control torque

# Parameters for the unbalanced torque from the Reaction
   Wheel
@variables Cs phi_s F_s T_s real=true
```

```
@variables(omega_s(t), real=true)          # Angular speed of
   the motor (reaction wheel)

# ================================================
# Definition of symbolic variables
# ================================================
# Dynamic functions
@variables psi(t) theta(t) beta(t) real=true  # Angles and
   damping coefficient

# ================================================
# Time derivatives
dpsi = D(psi)
dtheta = D(theta)

# ================================================
# Kinetic Energy (T) Calculation
# ================================================

# Relative positions (considering purely rotational motion)
xp = (a * cos(theta) + b) * sin(psi) + a * sin(theta) *
   cos(psi)  # Pendulum x-position
zp = (a * cos(theta) + b) * cos(psi) - a * sin(theta) *
   sin(psi)  # Pendulum z-position
xf = c * sin(psi)
                                                  # Fixed
   mass x-position
zf = c * cos(psi)
                                                  # Fixed
   mass z-position

# Absolute velocities
vx_p = expand_derivatives(D(xp)) + dpsi * zp  # Includes
   transport velocity
vz_p = expand_derivatives(D(zp)) - dpsi * xp
```

```
vx_f = expand_derivatives(D(xf)) + dpsi * zf  # relative + transport velocity
vz_f = expand_derivatives(D(zf)) - dpsi * xf

# Pendulum's Kinetic Energy
T_p = (1/2) * m_p * (vx_p^2 + vz_p^2)

# Fixed Mass's Kinetic Energy
T_f = (1/2) * m_f * (vx_f^2 + vz_f^2)

# Moment of inertia of the fixed mass
I_f = m_f * c^2

# Rotational kinetic energy of the fixed mass
T_fix = (1/2) * I_f * (dtheta + dpsi)^2

# Satellite's Rotational Energy
T_sat = (1/2) * I_sat * dpsi^2

# Total Kinetic Energy
T = T_p + T_f + T_sat + T_fix

# ================================================
# Potential Energy (V) Calculation
# ================================================

# Gravitational Potential Energy
V_gravity = m_p * g * zp + m_f * g * zf

# Elastic Potential Energy (stiffness coefficient)
V_spring = (1/2) * k * psi^2 + (1/2) * k_psi * theta^2  # New term: system stiffness

# Total Potential Energy
V = V_gravity + V_spring
```

```
81
82 # ================================================
83 # Lagrangian and Euler-Lagrange Equations
84 # ================================================
85
86 # Lagrangian
87 L = T - V
88
89 # ================================================
90 # Unbalanced torque T_s(t)
91 # ================================================
92 # Form: T_s(t) = Cs * b * (omega_s^2) * sin(omega_s * t +
      phi_s)
93 # Cs = m*r (mass and radius of RW respectively)
94 # T_s = Cs * c * (omega_s^2) * sin(omega_s*t + phi_s)
95
96 # Equation for psi (satellite)
97 dL_dpsidot = Symbolics.derivative(L, dpsi)
98 dL_dpsi = Symbolics.derivative(L, psi)
99 ddt_dL_dpsidot = expand_derivatives(D(dL_dpsidot))
100 eq_psi = ddt_dL_dpsidot - dL_dpsi - M_psi - T_s - F_s
101
102 # Equation for theta (pendulum)
103 dL_dthetadot = Symbolics.derivative(L, dtheta)
104 dL_dtheta = Symbolics.derivative(L, theta)
105 ddt_dL_dthetadot = expand_derivatives(D(dL_dthetadot))
106 eq_theta = ddt_dL_dthetadot - dL_dtheta + epsilon * dtheta
107
108 # Simplify equations
109 eq_psi_simp = simplify(eq_psi)
110 eq_theta_simp = simplify(eq_theta)
111
112 # ================================================
113 # System Matrices Assembly
114 # ================================================
```

```
115
116 # Add reaction wheel torque definition
117 T_s_func = Cs * (omega_s^2) * sin(omega_s * t + phi_s)
118
119 # Extract matrices from motion equations
120 # Collect state variables
121 q = [psi, theta]
122 q_dot = [dpsi, dtheta]
123 q_ddot = [D(dpsi), D(dtheta)]
124
125 # System can be written as: M * q_ddot + C * q_dot + K * q =
    F
126
127 # Initialize an array to store the equations in standard form
128 eqs = [eq_psi_simp, eq_theta_simp]
129
130 # Inertia matrix M
131 M = zeros(Num, 2, 2)
132
133 # Extract coefficients of q_ddot from each equation
134 for i in 1:2
135 for j in 1:2
136 if i == 1 && j == 1
137 M[i, j] = Symbolics.derivative(dL_dpsidot, dpsi)  # ddpsi in
    eq_psi
138 elseif i == 1 && j == 2
139 M[i, j] = Symbolics.derivative(dL_dpsidot, dtheta)  #
    ddtheta in eq_psi
140 elseif i == 2 && j == 1
141 M[i, j] = Symbolics.derivative(dL_dthetadot, dpsi)  # ddpsi
    in eq_theta
142 elseif i == 2 && j == 2
143 M[i, j] = Symbolics.derivative(dL_dthetadot, dtheta)  #
    ddtheta in eq_theta
144 end
```

```
145 end
146 end
147
148 # Damping matrix C
149 # In nonlinear systems, C may depend on q and q_dot
150 C = zeros(Num, 2, 2)
151 C[2, 2] = epsilon  # Damping in theta
152
153 # Stiffness matrix K (restoring forces)
154 K = zeros(Num, 2, 2)
155 K[1, 1] = k  # Stiffness associated with psi
156 K[1,2] = 0.0
157 K[2,1] = 0.0
158 K[2,2] = k_psi
159
160 # External forces vector F
161 F = zeros(Num, 2)
162 F[1] = M_psi + T_s_func + F_s  # Applied torque in psi
163
164 # Compute accelerations: q_ddot = M^(-1) * (-C * q_dot - K *
    q + F)
165 # For nonlinear systems, all nonlinear terms are included in
    F
166
167 # Symbolic inversion of M
168 M_inv = inv(M)
169
170 # Compute acceleration expressions
171 acceleration_expr = M_inv * (-C * [dpsi, dtheta] - K * [psi,
    theta] + F)
172
173 # ================================================
174 # Display Results (optional)
175 # ================================================#
    println("Euler-Lagrange Equation for \psi (satellite
```

```
    pitch):")
# println(eq_psi_simp)

# println("\nEuler-Lagrange Equation for    (pendulum
    angle):")
# println(eq_theta_simp)

# println("\nInertia Matrix M:")
# println(M)

# println("\nDamping Matrix C:")
# println(C)

# println("\nStiffness Matrix K:")
# println(K)

# println("\nExternal Forces Vector F:")
# println(F)

# println("\nAcceleration Expressions:")
# println("ddpsi = ", acceleration_expr[1])
# println("ddtheta = ", acceleration_expr[2])
```

Listing B.1 – Mathematical Modeling

—

APPENDIX C – Simulation Code for the Satellite-Fluid Model

This appendix presents the source code developed to simulate the dynamic model of a satellite with sloshing, used in the analyses described in Chapter **??**. The code was written in the Julia programming language and implements the equations of motion derived using the Lagrangian formulation.

```
# Required packages
using DifferentialEquations, DynamicalSystems, ChaosTools
using LinearAlgebra, StaticArrays, Statistics, FFTW
using Plots, CairoMakie, ProgressMeter
using CSV, DataFrames
using Base.Threads
using Symbolics
using SymbolicUtils
using Attractors
using StatsBase
using DelimitedFiles

# Parameter structure
struct MyParams
g       ::Float64   # gravitational acceleration
k       ::Float64   # stiffness
k_psi   ::Float64   # stiffness
I_sat   ::Float64   # satellite moment of inertia
M_psi   ::Float64   # control torque (if used)
Cs      ::Float64   # reaction-wheel coefficient
omega_s ::Float64   # reaction-wheel angular speed
phi_s   ::Float64   # reaction-wheel phase offset
beta_s  ::Float64   # not used in this snippet, but
   included
```

```
    F_f      ::Float64   # external force placeholder
    a        ::Float64   # pendulum length
    b        ::Float64   # pivot offset from sat. CG
    c        ::Float64   # offset for fixed mass
    d        ::Float64   # not used, but included
    epsilon  ::Float64   # damping
    m_p      ::Float64   # sloshing mass
    m_f      ::Float64   # fixed mass
    end

    #%%
    # System auxiliary functions
    function inertia_matrix(p::MyParams,   ::Real)
    T = typeof(  )
    M = Matrix{T}(undef, 2, 2)
    M[1,1] = p.I_sat
    + 4.0*p.a^2*p.m_p
    + 4.0*p.b^2*p.m_p
    + 5.0*p.c^2*p.m_f
    + 8.0 * p.a * p.b * p.m_p * cos(  )

    M[1,2] = 2.0*p.a^2*p.m_p
    + 1.0*p.c^2*p.m_f
    + 2.0*p.a*p.b*p.m_p*cos(  )

    M[2,1] = M[1,2]
    M[2,2] = p.a^2*p.m_p + p.c^2*p.m_f
    return M
    end

    function dissipative_matrix(p::MyParams,   ::Real,
        _dot  ::Real)
    T = typeof(  )
    C = Matrix{T}(undef, 2, 2)
    C[1,1] = -8.0 * p.a * p.b * p.m_p * sin(  ) *   _dot
```

```
58      C[1,2] = -2.0 * p.a * p.b * p.m_p * sin(  ) *  _dot
59      C[2,1] = 0.0
60      C[2,2] = -p.epsilon
61      return C
62      end
63
64      function restoration_forces(p::MyParams,  ::Real,
            ::Real)
65      T = typeof(  )
66      K = Matrix{T}(undef, 2, 2)
67      K[1,1] = p.k
68      K[1,2] = 0.0
69      K[2,1] = 0.0
70      K[2,2] = p.k_psi
71      return K
72      end
73
74      function calc_forcing_Ts(p::MyParams, t::Real)
75      return p.Cs * (p.omega_s^2) * sin(p.omega_s * t +
           p.phi_s)
76      end
77
78      function force_matrix(p::MyParams,  ::Real,  ::Real,
            _dot ::Real, M_psi::Real, T_sval::Real, t::Float64)
79      T_s_val = calc_forcing_Ts(p, t)
80      T = typeof(  )
81      F = Vector{T}(undef, 2)
82      F[1] = T_sval + M_psi
83      + p.a * p.g * p.m_p * sin(  +  )
84      + p.b * p.g * p.m_p * sin(  )
85      - p.c * p.g * p.m_f * sin(  )
86      F[2] = + p.a * p.g * p.m_p * sin(  +  )
87      - 4.0 * p.a * p.b * p.m_p * sin(  ) *  _dot ^2
88      return F
89      end
```

```
90
91      #%%
92      # System dynamics
93      function system_dynamics!(du, u, p, t)
94        ,    ,   _dot  ,   _dot   = u
95
96      Mmat = inertia_matrix(p,    )
97      Cmat = dissipative_matrix(p,    ,   _dot  )
98      Kmat = restoration_forces(p,    ,    )
99      T_s_val = calc_forcing_Ts(p, t)
100     M_psi_val = p.M_psi
101     Fvec = force_matrix(p,    ,    ,   _dot  , M_psi_val,
           T_s_val, t)
102
103     qdot = [ _dot  ,   _dot  ]
104     tmp = -Cmat*qdot - Kmat*[   ,    ] + Fvec
105     acc = Mmat \ tmp
106
107     du[1] =   _dot
108     du[2] =   _dot
109     du[3] = acc[1]
110     du[4] = acc[2]
111     end
112
113     # Default parameters
114     const DEFAULT_PARAMS = MyParams(
115     8.7,       # g
116     500.0,     # k_psi
117     90.0,     # k
118     720.0,     # I_sat
119     0.0,       # M_psi
120     1e-7,      # Cs
121     628.0,     # omega_s (6000 rpm)
122     deg2rad(0.0),    # phi_s
123     deg2rad(15.0),   # beta_s
```

```
    0.0,       # F_f
    0.28,      # a
    -0.19,     # b
    -0.38,     # c
    -0.20,     # d
    0.003,    # epsilon 0.0007 to 0.003,
    190.0,    # m_p
    460.0,    #m_f
    )

    # Standard initial conditions
    const STABLE_IC = [deg2rad(2.0), deg2rad(1.0), 0.1, 0.05]
    const QUASIPERIODIC_IC = [deg2rad(10.0), deg2rad(2.0),
       0.3, 0.1]
    const CHAOTIC_IC = [deg2rad(30.0), deg2rad(5.0), 0.5,
       0.5]

    # 5.1 Basic simulation and plotting with transient
       removal

    # Function for basic simulation
    function run_simulation(p::MyParams, u0; tspan=(0.0,
       2500.0), dt=0.01)
    prob = ODEProblem(system_dynamics!, u0, tspan, p)
    sol = solve(prob, saveat=dt)
    return sol
    end

    println("Running basic simulation...")
    sol = run_simulation(DEFAULT_PARAMS, CHAOTIC_IC,
       tspan=(0.0, 2500.0))

    # Function to remove transient
    function remove_transient(sol; t_transient=100.0)
    # Find index corresponding to transient time
```

```
154     idx_transient = findfirst(t -> t >= t_transient, sol.t)
155
156     # Extract data after transient
157     t_vals = sol.t[idx_transient:end]
158     psi_vals = [u[1] for u in sol.u[idx_transient:end]]
159     theta_vals = [u[2] for u in sol.u[idx_transient:end]]
160     dpsi_vals = [u[3] for u in sol.u[idx_transient:end]]
161     dtheta_vals = [u[4] for u in sol.u[idx_transient:end]]
162
163     return t_vals, psi_vals, theta_vals, dpsi_vals,
            dtheta_vals
164     end
165
166     # Extract complete results for comparison
167     t_vals_full = sol.t
168     psi_vals_full = [u[1] for u in sol.u]
169     theta_vals_full = [u[2] for u in sol.u]
170     dpsi_vals_full = [u[3] for u in sol.u]
171     dtheta_vals_full = [u[4] for u in sol.u]
172
173     # File name
174     filename = "dadossimulacao.csv"
175
176     # Data structure: time,    ,    , d  , d
177     dados = hcat(t_vals_full, psi_vals_full,
            theta_vals_full, dpsi_vals_full, dtheta_vals_full)
178
179     # Save with header
180     open(filename, "w") do io
181     writedlm(io, ["time,psi,theta,dpsi,dtheta"])
182     writedlm(io, dados, ',')
183     end
184
185
186     # Remove transient
```

```
187     # Define transient time (adjust as needed)
188     t_transient = 100.0
189     t_vals, psi_vals, theta_vals, dpsi_vals, dtheta_vals =
            remove_transient(sol, t_transient=t_transient)
190
191     println("Transient removed. Data reduced from
            $(length(t_vals_full)) to $(length(t_vals)) points.")
192
193     # Plot time series with transient marking
194
195     # Figure 1: Satellite Pitch Angle
196     p1 = Plots.plot(t_vals_full, psi_vals_full, label="  (t)
            complete", color=:lightgray, alpha=0.5)
197     Plots.plot!(p1, t_vals, psi_vals, label="  (t) without
            transient", color=:mediumslateblue)
198     Plots.vline!(p1, [t_transient], label="transient end",
            linestyle=:dash, color=:red)
199     Plots.xlabel!(p1, "time (s)")
200     Plots.ylabel!(p1, "   (rad) - Satellite Pitch Angle")
201     Plots.title!(p1, "Time Series: Satellite Pitch Angle")
202     # Save p1
203     Plots.savefig(p1,
            "satellite_pitch_angle_time_series.png")
204     Plots.savefig(p1,
            "satellite_pitch_angle_time_series.pdf")
205
206     # Figure 2: Angular Position of the Pendulum Mass
207     p2 = Plots.plot(t_vals_full, theta_vals_full,
            label="  (t) complete", color=:lightgray, alpha=0.5)
208     Plots.plot!(p2, t_vals, theta_vals, label="  (t) without
            transient", color=:orchid)
209     Plots.vline!(p2, [t_transient], label="transient end",
            linestyle=:dash, color=:red)
210     Plots.xlabel!(p2, "time (s)")
211     Plots.ylabel!(p2, "   (rad) - Angular position of the
```

```
        pendulum's mass")
212     Plots.title!(p2, "Time Series: Angular Position of the
        Pendulum's Mass")
213     # Save p2
214     Plots.savefig(p2,
        "pendulum_angular_position_time_series.png")
215     Plots.savefig(p2,
        "pendulum_angular_position_time_series.pdf")
216
217     # Figure 3: Satellite Pitch Angular Velocity
218     p3 = Plots.plot(t_vals_full, dpsi_vals_full,
        label="d  (t) complete", color=:lightgray, alpha=0.5)
219     Plots.plot!(p3, t_vals, dpsi_vals, label="d  (t) without
        transient", color=:mediumslateblue)
220     Plots.vline!(p3, [t_transient], label="transient end",
        linestyle=:dash, color=:red)
221     Plots.xlabel!(p3, "time (s)")
222     Plots.ylabel!(p3, "d  (rad/s) - Satellite Pitch Angular
        Velocity")
223     Plots.title!(p3, "Time Series: Satellite Pitch Angular
        Velocity")
224     # Save p3
225     Plots.savefig(p3,
        "satellite_pitch_angular_velocity_time_series.png")
226     Plots.savefig(p3,
        "satellite_pitch_angular_velocity_time_series.pdf")
227
228     # Figure 4: Angular Velocity of the Pendulum Mass
229     p4 = Plots.plot(t_vals_full, dtheta_vals_full,
        label="d  (t) complete", color=:lightgray, alpha=0.5)
230     Plots.plot!(p4, t_vals, dtheta_vals, label="d  (t)
        without transient", color=:orchid)
231     Plots.vline!(p4, [t_transient], label="transient end",
        linestyle=:dash, color=:red)
232     Plots.xlabel!(p4, "time (s)")
```

```
233     Plots.ylabel!(p4, "d   (rad/s) - Angular velocity of the
           pendulum's mass")
234     Plots.title!(p4, "Time Series: Angular Velocity of the
           Pendulum's Mass")
235     # Save p4
236     Plots.savefig(p4,
           "pendulum_angular_velocity_time_series.png")
237     Plots.savefig(p4,
           "pendulum_angular_velocity_time_series.pdf")
```

Listing C.1 – Main simulation function for the satellite-fluid system

Below, the time histories are extracted as vectors: - $\psi(t)$: Satellite pitch angle - $\theta(t)$: Angular position of the pendulum's mass - $\dot{\psi}(t)$: Angular velocity of the satellite - $\dot{\theta}(t)$: Angular velocity of the pendulum's mass

The transient is removed from the data, and plots are generated: - Figure 1 shows $\psi(t)$ and its filtered version (without transient). - Figure 2 displays $\theta(t)$ before and after transient filtering. - Figures 3 and 4 show the corresponding angular velocities: $\dot{\psi}(t)$ and $\dot{\theta}(t)$.

The data is also exported to the file 'dadossimulacao.csv' for further analysis.

APPENDIX D – Analytical expressions for the matrices A(x), B(x), and the vector G(x,t)

The complete analytical expressions for the matrices $A(x)$, $B(x)$, and the vector $G(x,t)$ are provided in this appendix.

$$\mathbf{A}(\mathbf{x}) = \begin{bmatrix} 0 & 0 & 1 & 0 \\ 0 & 0 & 0 & 1 \\ A_{31} & A_{32} & A_{33} & A_{34} \\ A_{41} & A_{42} & A_{43} & A_{44} \end{bmatrix} \tag{D.1}$$

$$\mathbf{B}(\mathbf{x}) = \begin{bmatrix} 0 \\ 0 \\ B_{31} \\ B_{41} \end{bmatrix} \tag{D.2}$$

$$\mathbf{G}(\mathbf{x}, \mathbf{t}) = \begin{bmatrix} 0 \\ 0 \\ G_{31} \\ G_{41} \end{bmatrix} \tag{D.3}$$

where:

$$A_{31} = -\frac{g\cos(\psi+\theta)a^3m_p^2 + g\cos(\psi)a^2cm_fm_p + bg\cos(\psi+2\theta)a^2m_p^2 + k_\psi a^2m_p + g\cos(\psi)c^3m_f^2 - bg\cos(\psi)c^2m_fm_p + k_\psi c^2m_f}{D}$$

$$A_{32} = \frac{2a^2km_p + c^2km_f - a^3gm_p^2\cos(\psi+\theta) + 8a^2b^2m_p^2\dot{\psi}^2\cos(2\theta) - 2a^2bgm_p^2\cos(\psi+2\theta) + 2abkm_p\cos(\theta)}{D}$$

$$\frac{+8a^3bm_p^2\dot{\psi}^2\cos(\theta) + 2a^3bm_p^2\dot{\theta}^2\cos(\theta) + 8a^3bm_p^2\dot{\psi}\dot{\theta}\cos(\theta)}{D}$$

$$+\frac{2ab\varepsilon m_p\dot{\theta}\sin(\theta) - 2abkm_p\theta\sin(\theta) + 4abc^2m_fm_p\dot{\psi}^2\cos(\theta) + 2abc^2m_fm_p\dot{\theta}^2\cos(\theta) + 8abc^2m_fm_p\dot{\psi}\dot{\theta}\cos(\theta)}{D}$$

$$-\frac{\left(8\cos(\theta)\sin(\theta)a^2b^2m_p^2 - 4m_f\sin(\theta)abc^2m_p\right)\cdot N_1}{D^2}$$

$$A_{33} = \frac{8a^2b^2m_p^2\dot{\psi}\sin(2\theta) + 16a^3bm_p^2\dot{\psi}\sin(\theta) + 8a^3bm_p^2\dot{\theta}\sin(\theta) + 8abc^2m_fm_p\dot{\psi}\sin(\theta) + 8abc^2m_fm_p\dot{\theta}\sin(\theta)}{D}$$

$$A_{34} = \frac{8a^3bm_p^2\dot{\psi}\sin(\theta) - c^2\varepsilon m_f - 2a^2\varepsilon m_p + 4a^3bm_p^2\dot{\theta}\sin(\theta) - 2ab\varepsilon m_p\cos(\theta) + 8abc^2m_fm_p\dot{\psi}\sin(\theta) + 4abc^2m_fm_p\dot{\theta}\sin(\theta)}{D}$$

$$B_{31} = \frac{m_pa^2 + m_fc^2}{D}$$

$$B_{41} = -\frac{2m_pa^2 + 2bm_pa\cos(\theta) + m_fc^2}{D}$$

$$
\begin{aligned}
G_{31} = & \frac{M_\psi a^2 m_p + M_\psi c^2 m_f + T_s a^2 m_p + T_s c^2 m_f - a^3 g m_p^2 \sin(\psi+\theta) - c^3 g m_f^2 \sin(\psi) - 2a^2 \varepsilon m_p \dot{\theta} - a^2 k_\psi m_p \psi - c^2 \varepsilon m_f \dot{\theta} - c^2 k_\psi m_f \psi + 2a^2 k m_p \theta + c^2 k m_f \theta}{D} \\
& + \frac{8a^3 b m_p^2 \dot{\psi}^2 \sin(\theta) + 2a^3 b m_p^2 \dot{\theta}^2 \sin(\theta) + 4a^2 b^2 m_p^2 \dot{\psi}^2 \sin(2\theta) - a^2 b g m_p^2 \sin(\psi+2\theta)}{D} \\
& + \frac{8a^3 b m_p^2 \dot{\psi}\dot{\theta} \sin(\theta) - 2ab\varepsilon m_p \dot{\theta} \cos(\theta) + 2abk m_p \theta \cos(\theta) - a^2 c g m_f m_p \sin(\psi) + bc^2 g m_f m_p \sin(\psi)}{D} \\
& + \frac{4abc^2 m_f m_p \dot{\psi}^2 \sin(\theta) + 2abc^2 m_f m_p \dot{\theta}^2 \sin(\theta) + 8abc^2 m_f m_p \dot{\psi}\dot{\theta} \sin(\theta)}{D} \\
& - \frac{\theta(2a^2 k m_p + c^2 k m_f - a^3 g m_p^2 \cos(\psi+\theta) + 8a^2 b^2 m_p^2 \dot{\psi}^2 \cos(2\theta) - 2a^2 b g m_p^2 \cos(\psi+2\theta))}{D} \\
& + \frac{\theta(2abk m_p \cos(\theta) + 8a^3 b m_p^2 \dot{\psi}^2 \cos(\theta) + 2a^3 b m_p^2 \dot{\theta}^2 \cos(\theta) + 8a^3 b m_p^2 \dot{\psi}\dot{\theta} \cos(\theta))}{D} \\
& + \frac{\theta(2ab\varepsilon m_p \dot{\theta} \sin(\theta) - 2abk m_p \theta \sin(\theta) + 4abc^2 m_f m_p \dot{\psi}^2 \cos(\theta) + 2abc^2 m_f m_p \dot{\theta}^2 \cos(\theta) + 8abc^2 m_f m_p \dot{\psi}\dot{\theta} \cos(\theta))}{D^2} \\
& + \frac{4abm_p(m_f \sin(\theta) c^2 - abm_p \sin(2\theta))(M_\psi a^2 m_p + M_\psi c^2 m_f + T_s a^2 m_p + T_s c^2 m_f - a^3 g m_p^2 \sin(\psi+\theta) - c^3 g m_f^2 \sin(\psi)}{D^2} \\
& + \frac{-2a^2 \varepsilon m_p \dot{\theta} - a^2 k_\psi m_p \psi - c^2 \varepsilon m_f \dot{\theta} - c^2 k_\psi m_f \psi + 2a^2 k m_p \theta + c^2 k m_f \theta + 8a^3 b m_p^2 \dot{\psi}^2 \sin(\theta)}{D^2} \\
& + \frac{2a^3 b m_p^2 \dot{\theta}^2 \sin(\theta) + 4a^2 b^2 m_p^2 \dot{\psi}^2 \sin(2\theta) - a^2 b g m_p^2 \sin(\psi+2\theta) + 8a^3 b m_p^2 \dot{\psi}\dot{\theta} \sin(\theta) - 2ab\varepsilon m_p \dot{\theta} \cos(\theta) + 2abk m_p \theta \cos(\theta) - a^2 c g m_f m_p \sin(\psi)}{D^2} \\
& + \frac{bc^2 g m_f m_p \sin(\psi) + 4abc^2 m_f m_p \dot{\psi}^2 \sin(\theta) + 2abc^2 m_f m_p \dot{\theta}^2 \sin(\theta) + 8abc^2 m_f m_p \dot{\psi}\dot{\theta} \sin(\theta))}{D^2} \\
& + \frac{\psi(g \cos(\psi+\theta) a^3 m_p^2 + g \cos(\psi) a^2 c m_f m_p + bg \cos(\psi+2\theta) a^2 m_p^2 + k_\psi a^2 m_p + g \cos(\psi) c^3 m_f^2 - bg \cos(\psi) c^2 m_f m_p + k_\psi c^2 m_f)}{D} \\
& - \frac{\dot{\theta}(8a^3 b m_p^2 \dot{\psi} \sin(\theta) - c^2 \varepsilon m_f - 2a^2 \varepsilon m_p + 4a^3 b m_p^2 \dot{\theta} \sin(\theta) - 2ab\varepsilon m_p \cos(\theta) + 8abc^2 m_f m_p \dot{\psi} \sin(\theta) + 4abc^2 m_f m_p \dot{\theta} \sin(\theta))}{D} \\
& - \frac{8abm_p \dot{\psi}(2a^2 m_p \dot{\psi} \sin(\theta) + c^2 m_f \dot{\psi} \sin(\theta) + a^2 m_p \dot{\theta} \sin(\theta) + c^2 m_f \dot{\theta} \sin(\theta) + 2abm_p \dot{\psi} \cos(\theta) \sin(\theta))}{D}
\end{aligned}
$$

$$
\begin{aligned}
G_{41} = & \frac{I_{\text{sat}}k + 4a^2km_p + 4b^2km_p + 5c^2km_f - 2a^3gm_p^2\cos(\psi+\theta)}{D} \\
& - \frac{3ab^2gm_p^2\cos(\psi+\theta) - I_{\text{sat}}agm_p\cos(\psi+\theta) + 32a^2b^2m_p^2\psi_{\text{dot}}^2\cos(2\theta)}{D} \\
& + \frac{4a^2b^2m_p^2\theta_{\text{dot}}^2\cos(2\theta) - ab^2gm_p^2\cos(\psi-\theta) - 6a^2bgm_p^2\cos(\psi+2\theta)}{D} \\
& - \frac{2M_\psi abm_p\sin(\theta) - 2T_s abm_p\sin(\theta) + 8abkm_p\cos(\theta)}{D} \\
& + \frac{16ab^3m_p^2\psi_{\text{dot}}^2\cos(\theta) + 16a^3bm_p^2\psi_{\text{dot}}^2\cos(\theta) + 4a^3bm_p^2\theta_{\text{dot}}^2\cos(\theta)}{D} \\
& + \frac{16a^3bm_p^2\psi_{\text{dot}}\theta_{\text{dot}}\cos(\theta) + 8ab\epsilon m_p\theta_{\text{dot}}\sin(\theta)}{D} \\
& + \frac{2abk_\psi m_p\psi\sin(\theta) - 8abkm_p\theta\sin(\theta) - 4ac^2gm_fm_p\cos(\psi+\theta)}{D} \\
& + \frac{4I_{\text{sat}}abm_p\psi_{\text{dot}}^2\cos(\theta) + 16a^2b^2m_p^2\psi_{\text{dot}}\theta_{\text{dot}}\cos(2\theta)}{D} \\
& + \frac{20abc^2m_fm_p\psi_{\text{dot}}^2\cos(\theta) + 2abc^2m_fm_p\theta_{\text{dot}}^2\cos(\theta)}{D} \\
& - \frac{abcgm_fm_p\cos(\psi+\theta) + abcgm_fm_p\cos(\psi-\theta)}{D} \\
& + \frac{8abc^2m_fm_p\psi_{\text{dot}}\theta_{\text{dot}}\cos(\theta)}{D}
\end{aligned}
$$

where:

$$
\begin{aligned}
D = & \, 4c^4m_f^2 + 4a^2b^2m_p^2 + I_{\text{sat}}a^2m_p + I_{\text{sat}}c^2m_f + 5a^2c^2m_fm_p \\
& + 4b^2c^2m_fm_p - 4a^2b^2m_p^2\cos^2(\theta) + 4abc^2m_fm_p\cos(\theta) \\
N_1 = & \, 2a^2km_p\theta - c^3gm_f^2\sin(\psi) - 2a^2\varepsilon m_p\dot{\theta} - a^2k_\psi m_p\psi - c^2\varepsilon m_f\dot{\theta} - c^2k_\psi m_f\psi \\
& - a^3gm_p^2\sin(\psi+\theta) + c^2km_f\theta + 8a^3bm_p^2\dot{\psi}^2\sin(\theta) + 2a^3bm_p^2\dot{\theta}^2\sin(\theta) \\
& + 4a^2b^2m_p^2\dot{\psi}^2\sin(2\theta) - a^2bgm_p^2\sin(\psi+2\theta) + 8a^3bm_p^2\dot{\psi}\dot{\theta}\sin(\theta) \\
& - 2ab\varepsilon m_p\dot{\theta}\cos(\theta) + 2abkm_p\theta\cos(\theta) - a^2cgm_fm_p\sin(\psi) + bc^2gm_fm_p\sin(\psi) \\
& + 4abc^2m_fm_p\dot{\psi}^2\sin(\theta) + 2abc^2m_fm_p\dot{\theta}^2\sin(\theta) + 8abc^2m_fm_p\dot{\psi}\dot{\theta}\sin(\theta)
\end{aligned}
$$